# Development, Functionalisation, and Characterisation of Triply Periodic Minimum Surface Hydrogels for Solid-Tolerant Chromatography

A thesis submitted in partial fulfilment of the requirements for the degree of

**Doctor of Philosophy in Chemical and Process Engineering**

**University of Canterbury**


Written by

Anne Mary Gordon


November 2019


Department of Chemical and Process Engineering
Te Whare Wānanga o Waitaha, University of Canterbury
Ōtautahi, Christchurch
Aotearoa, New Zealand

# A. Abstract

The work presented in this thesis demonstrates the development of the first chromatography columns for solid-tolerant chromatography produced using 3D-printing methods. This work developed from the rapidly evolving 3D-printing industry, with the hypothesis that 3D-printing methods could be used to produce chromatography columns in a controlled geometry structure. In this application, columns were specifically designed for solid-tolerant chromatography, thus addressing one of the bottlenecks in downstream processing of biological feedstocks, because columns combined primary protein recovery with cell removal from a cell culture or fermentation broth.

Columns were made in triply periodic minimum surface structures such as Schwarz diamond and Schoen gyroid from agarose and cellulose hydrogels. These columns had large monolith-type channels (300 μm – 500 μm) allowing cell passage but had the benefit of high surface area for adsorption from the inherent porosity of the hydrogels. Columns were functionalised for three common types of chromatography, demonstrated competitive static adsorption performance compared with commercial resins, and were able to capture protein from a cell/protein mixture, demonstrating solid-tolerant chromatography capabilities. The cellulose CM column was measured to have a binding capacity of 132.8 mg/mL cytochrome c, the agarose DEAE column had a static binding capacity of 229.7 mg/mL BSA, and the agarose HIC column had a static binding capacity of 36.4 mg/mL α-lactalbumin.

This work goes through several steps to prove the concept of using 3D-printing methods to produce columns for solid-tolerant chromatography. In the first part of this work, the successful prototyping of TPMS hydrogel structures using a 3D-printed template was demonstrated, with column features on the same order of magnitude as beads used in some protein chromatography applications. TPMS features were shown to be prototyped with good fidelity to their initial design. Next, successful functionalisation was demonstrated through ion exchange and protein binding capacity experiments. The performance of the columns under dynamic conditions was then characterised, showing mass transfer effects reliant on TPMS channel diameter and on-sample velocity. An investigation into limiting parameters of the functionalisation procedure was then presented. Lastly, the effect of yeast cells on protein adsorption was analysed, and cell recovery over a range of velocities on the different columns was characterised.

# B. Contents

# C. List of Figures

# D. List of Tables

# E. Nomenclature

## List of Symbols

### *Roman Alphabet*

| Symbol | Definition | Unit |
|---|---|---|
| $A$ | Cross-sectional area | $m^2$ |
| $a$ | Freundlich isotherm constant | - |
| $a$ | Hydrodynamic dispersion term (van Deemter) | - |
| $A_s$ | Porosity dependent parameter | - |
| $b$ | Freundlich isotherm constant | - |
| $b$ | Axial diffusion term (van Deemter) | - |
| $C$ | Liquid or mobile phase concentration | mg/ml or $mol/m^3$ |
| $c$ | Mass transport term (van Deemter) | - |
| $C_0$ | Initial liquid or mobile phase concentration | mg/ml or $mol/m^3$ |
| $C_s$ | Liquid or mobile phase salt concentration | mg/ml or $mol/m^3$ |
| $d$ | Diameter, generic | m |
| $\boldsymbol{D_{ax}}$ | Axial dispersion coefficient | $m^2/s$ |
| $DBC$ | Dynamic binding capacity | mg/ml or $mol/m^3$ |
| $\boldsymbol{D_m}$ | Molecular diffusivity | $m^2/s$ |
| $d_m$ | Molecular diameter | Å |
| $\boldsymbol{D_{m,AB}}$ | Molecular diffusivity of A in B | $m^2/s$ |
| $d_p$ | Particle diameter | m |
| $d_s$ | Solid particle diameter | m |
| $F_0$ | Volumetric flowrate | $m^3/s$ or ml/min |
| $g$ | Gravitational acceleration | $m/s^2$ |
| $H$ | Hamaker constant $3x10^{-21} - 4x10^{-20}$ J | J |
| $h'$ | Reduced plate height | - |
| $HETP$ | Height equivalent to a theoretical plate | m |
| $IEX$ | Ion exchange capacity | eQ/ml |
| $K$ | Adsorption equilibrium constant | ml/mg or $m^3/mol$ |
| $k$ | Boltzmann constant, $1.3805x10^{-23}$ J/K | J/K |
| $k_{ads}$ | Rate of adsorption | $mol/m^2s$ |
| $K_D$ | Distribution coefficient | - |
| $k_{des}$ | Rate of desorption | $mol/m^2s$ |
| $K_e$ | Affinity constant | ml/mg or $m^3/mol$ |

| | | |
|---|---|---|
| $L$ | Length | L |
| $M_w$ | Molecular weight | g/mol or Da |
| $N$ | Plate number | - |
| $n$ | Number of moles | mol |
| $N_A$ | Attraction number | - |
| $N_D$ | Dispersion number | - |
| $N_G$ | Gravity number | - |
| $N_R$ | Aspect ratio | - |
| $N_{vdW}$ | van der Waals number | - |
| $Pe$ | Peclet number | - |
| $q$ | Adsorbed or stationary phase concentration | mg/ml or mol/m$^3$ |
| $q_e$ | Equilibrium binding capacity | mg/ml or mol/m$^3$ |
| $q_{max}$ | Maximum ion exchange capacity | mg/ml or mol/m$^3$ |
| $Re$ | Reynolds number | - |
| $Re_l$ | Modified Reynolds number | - |
| $SBC$ | Saturation binding capacity | mg/ml or mol/m$^3$ |
| $St$ | Stokes number | - |
| $S_v$ | Specific surface area per unit volume | m$^{-1}$ |
| $t$ | Time | s |
| $T$ | Temperature | K |
| $u$ | Linear velocity | m/s or cm/h |
| $v$ | Interstitial velocity | m/s |
| $V$ | Volume | ml or m$^3$ |
| $v'$ | Reduced velocity | - |
| $V_A$ | Molar volume species A | m$^3$/mol |
| $V_{column}$ | Column volume | ml or m$^3$ |
| $V_e$ | Mean elution volume | ml or m$^3$ |
| $V_{e,i}$ | Mean elution volume, species i | ml or m$^3$ |
| $V_i$ | Interstitial volume | ml or m$^3$ |
| $V_p$ | Pore volume | ml or m$^3$ |
| $\varkappa$ | Effective charge | - |
| $\Delta P$ | Pressure drop | Pa |

### *Greek Alphabet*

| Greek Symbol | Definition | Unit |
|---|---|---|
| $\alpha$ | Interaction coefficient | - |
| $\varepsilon$ | Total void fraction | - |
| $\varepsilon_i$ | Interstitial fraction | - |
| $\varepsilon_p$ | Pore fraction | - |
| $\eta_0$ | Overall filter capture efficiency | - |
| $\eta_D$ | Diffusion mechanism capture efficiency | - |
| $\eta_G$ | Sedimentation mechanism capture efficiency | - |
| $\eta_I$ | Interception mechanism capture efficiency | - |
| $\kappa$ | Permeability | $1/m^2$ |
| $\mu$ | Dynamic viscosity | Pa.s |
| $\mu_i$ | Mean residence time | s |
| $\rho$ | Density | $kg/m^3$ |
| $\sigma$ | Steric hindrance | - |
| $\sigma$ | Variance | s or ml |

## List of Abbreviations

| Abbreviation | Definition |
|---|---|
| ABS | Acrylonitrile butadiene styrene |
| AM | Additive manufacturing |
| BET | Brunauer-Emmett-Teller |
| BSA | Bovine serum albumin |
| CAD | Computer-aided design |
| CDI | 1,1'-carbonyl diimidazole |
| CFD | Computational fluid dynamics |
| CHO | Chinese hamster ovary |
| CIP | Clean-in-place |
| CM | Carboxy methyl |
| DBC | Dynamic binding capacity |
| DEAE | Diethylaminoethyl |
| DSP | Downstream processing |
| DVB | Divinyl benzene |
| EBA | Expanded bed adsorption |
| EBC | Equilibrium binding capacity |

| | |
|---|---|
| ECH | Epichlorohydrin |
| FDM | Fused deposition modelling |
| G | Gyroid |
| GMAC | Glycidyl trimethylammonium chloride |
| HETP | Height equivalent to a theoretical plate |
| HIC | Hydrophobic interaction chromatography |
| HPLC | High-performance liquid chromatography, high-pressure liquid chromatography |
| IEX | Ion exchange capacity |
| IgG | Immunoglobulin G |
| ISEC | Inverse size exclusion chromatography |
| MAbs | Monoclonal antibodies |
| PBC | Packed-bed chromatography |
| PEEK | Polyetheretherketone |
| PEGDA | polyethylene glycol diacrylate |
| pI | Isoelectric point |
| PLA | Poly-lactic acid |
| PP | Polypropylene |
| PS | Polystyrene |
| Q | Quaternary ammonium |
| RTD | Residence time distribution |
| SBC | Saturation binding capacity |
| SD | Schwarz diamond |
| SEC | Size exclusion chromatography |
| SEM | Scanning electron microscope |
| SLM | Selective laser melting |
| SLS | Selective laser sintering |
| SMA | Steric mass action |
| SP | Sulfopropyl |
| TPMS | Triply periodic minimum surface |
| UV | Ultraviolet |

# Chapter 1. Introduction

## 1.1 Background

The purification of biological products such as proteins, enzymes and other therapeutics from cell cultures and fermentation broths is of key importance in recovering a product of high purity. The desired product is often at very low concentration in the feedstock, which is also contaminated with other chemicals, particulates and biological products, meaning that a rigorous series of steps is required to purify the product to the extent required for therapeutic use. The series of unit operations required to capture and purify the biological feedstock after the growth of cells in the cell culture or fermentation broth is often called "downstream processing". These operations can include cell disruption, removal of solids, primary capture of the product, further purification and concentration and, finally, polishing. The number of steps involved in overall purification affects the processing costs and potential yield of target products. With more unit operations, capital and processing costs increase, and the yield decreases because in each process some of the target product is usually entrained out of the waste stream (Figure 1-1). Hence, it is desirable to reduce the number of processing steps to optimise the processing costs and overall recovery.

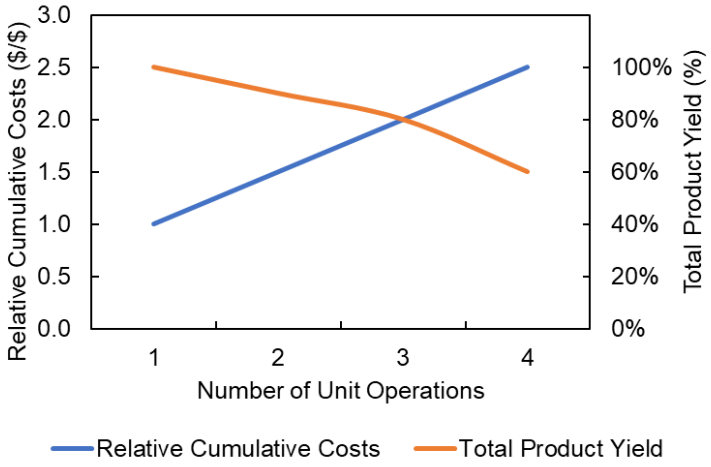


*Figure 1-1: Effect of additional unit operations on cumulative costs and product yield. Relative cumulative cost is the cumulative cost of the number of operations in the process divided by the cost of a single unit operation process.*

Perhaps the most prominent unit operation involved in downstream processing of therapeutic products is packed-bed chromatography (PBC). It appears in primary capture of the target molecule, as well as further processing steps to get the product to the desired purity. For

example, in monoclonal antibody (MAb) production, immunoglobulin G (IgG) is captured from cultured Chinese hamster ovary (CHO) cells by affinity chromatography, achieving the primary capture of the monoclonal antibody, then cation exchange and anion exchange steps are used in the subsequent purification and polishing phases (Figure 1-2). Because of its common usage, it is important that chromatographic steps are finely tuned and optimised for highest yield and lowest processing costs.

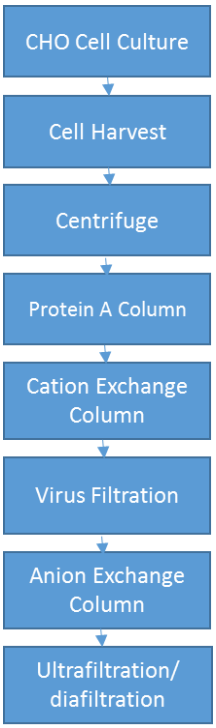


*Figure 1-2: Downstream processing schematic for IgG from CHO cell culture, adapted from Gottschalk [1]*

Downstream processing in general and, more specifically, PBC, have been identified as both practical and economic bottlenecks in the production of biopharmaceutical products. In PBC, a beaded resin of spheres (stationary phase) is randomly packed into a column. A mixture of solutes (mobile phase) is applied to the column, and the mixture separates based on each components' interaction with the stationary phase. The beads have a specified median diameter and a size range. For example, CM-Sepharose Fast Flow has a mean bead diameter of 90 µm, and a particle diameter range of 45 µm – 165 µm [2]. Because of the size distribution and random packing no two packed columns are ever identical. The different bead size distribution and random packing means that the flow profile of the mobile around the stationary phase is different in every different column, meaning that the separation of components will be different, and the capture and separation of high value products is unpredictable. Packed beds can be susceptible to blockages, dead-zone formation and

channelling, which reduces the overall separation efficiency of the columns. The feedstocks to packed beds must be completely free of solid material because they block the voids between the beads. For example, the 90 µm bead would have a pore diameter range of 45 nm – 100 nm and void sizes around 1 µm to 30 µm. Typical yeast cells and debris range in diameter from 4 µm – 40 µm, meaning these cells not only block the pores but the voids too. A paper by Datar et al. [3] supported by Thömmes [4] highlighted the problems with the typical solid removal steps required before PBC such as centrifugation because fast acceleration can damage sensitive cells, and filtration where the target biological may bind non-specifically to the filter medium, lowering the yield. An industry survey conducted by BioPharma Associates [5] identified column chromatography as the most serious contributor to the bottleneck because it is time-consuming as a result of the slow diffusion process, hardware and consumables are expensive, columns are run in batch operation, and the amount of mobile phase that can be processed at once (titre) is generally small. Both the academic and industrial view is that this bottleneck may be overcome by finding a substitute for column chromatography and/or combining solids removal with primary capture.

Expanded bed adsorption was developed as a unit operation which combined solids removal with primary protein capture. In expanded bed adsorption, the mobile phase is applied to a fluidised bed of beaded resin. The voids between the resin while fluidised provide sufficient space for the unwanted suspended particles in the feed-stream to pass through without causing blockages, while the target protein binds to the resin. The columns can be designed to immobilise the cells to the surface, with unwanted proteins and other biologicals flowing through the column. Similar and even superior purification was achieved with EBA compared with PBC in some instances [6-8]. However, the initial potential of integrating EBA into downstream processing was never fully realised because there were a number of disadvantages with EBA, including:

- Difficulty in predicting fluidisation behaviour;
- Non-specific binding of cells to resin that led to fluidisation instabilities;
- High fouling rates;
- Intensive clean in place (CIP) required resulting in disintegration of resin;
- High cost of retrofitting EBA hardware into existing processes;
- Cell-adsorbent aggregates forming and becoming entrained in the outlet flow from the column.

The high number of disadvantages above typically outweighs the advantages of EBA. Therefore, while research and development on this process is still being conducted, it is not likely to be implemented widely in downstream processing.

3D-printing technologies are seen as one of the disruptive technologies of the 21st Century. Also known as "additive manufacturing", 3D-printing is the ability of a 3D structure to be directly made from a model by a printer, where the model is built layer-by-layer. Typical types of printers may include extrusion, sintering, or photo-curing. From basic trinkets and jewellery to cell scaffolds and human organs, 3D-printing methods are being introduced in all industries. Downstream processing and chromatography were not immune to this development: in 2014 Fee et al. at the University of Canterbury highlighted the potential of 3D-printing as a way to overcome the downfalls associated with randomly packed beds of adsorptive media, because it would be possible to design and print a column with a geometry optimised for separation [9]. In the research presented in this thesis, 3D-printing was used to produce chromatography columns with a tightly controlled geometry designed to combine solids removal and primary protein capture from biological feedstocks.

Triply periodic minimum surfaces (TPMS) were used as the base geometry for the chromatography columns developed in this thesis (Figure 1-3). These columns have large channels that enable cell passage but are made from hydrogels with a highly microporous internal structure which offers a large surface area where protein adsorption can occur (Figure 1-4). Because the columns were made from agarose and cellulose, they were able to be chemically modified with cation exchange, anion exchange, and hydrophobic ligands, with the primary focus herein being on cation exchange columns. This thesis focuses on the agarose and cellulose columns prototyped, demonstrating the controlled geometries achieved using 3D-printing techniques and the successful chromatographic separations achieved. The chromatographic performance of the columns is analysed under static and dynamic conditions, and cell recovery is quantified for the different channel diameters. Conclusions are drawn regarding the suitability of the columns to be integrated into downstream processing as a combined solid removal/primary capture step. The potential of this project to form a marketable column for the bioprocessing industry is large. However, the development and optimisation of channel geometries using computational fluid dynamics, development of printing techniques, and full mechanical testing of the columns has not been included in this study.

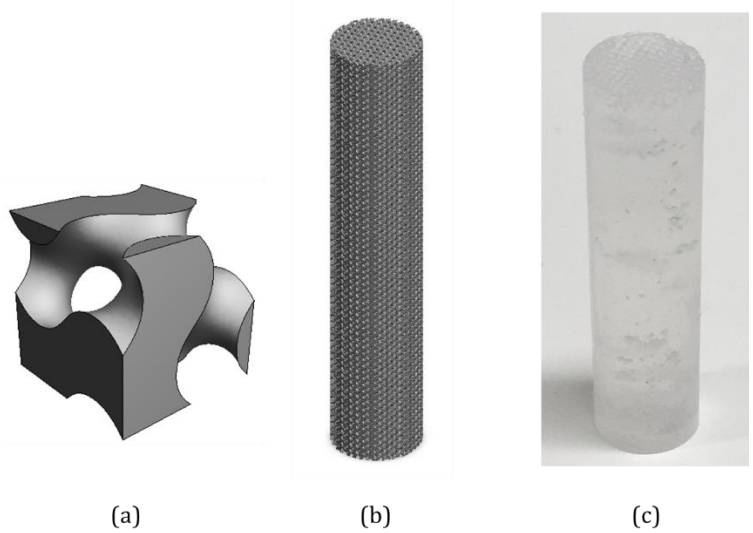


*Figure 1-3: (a) TPMS unit cell (gyroid), (b) 3D model of TPMS column template consisting of repeating unit cells, (c) final TPMS agarose column*

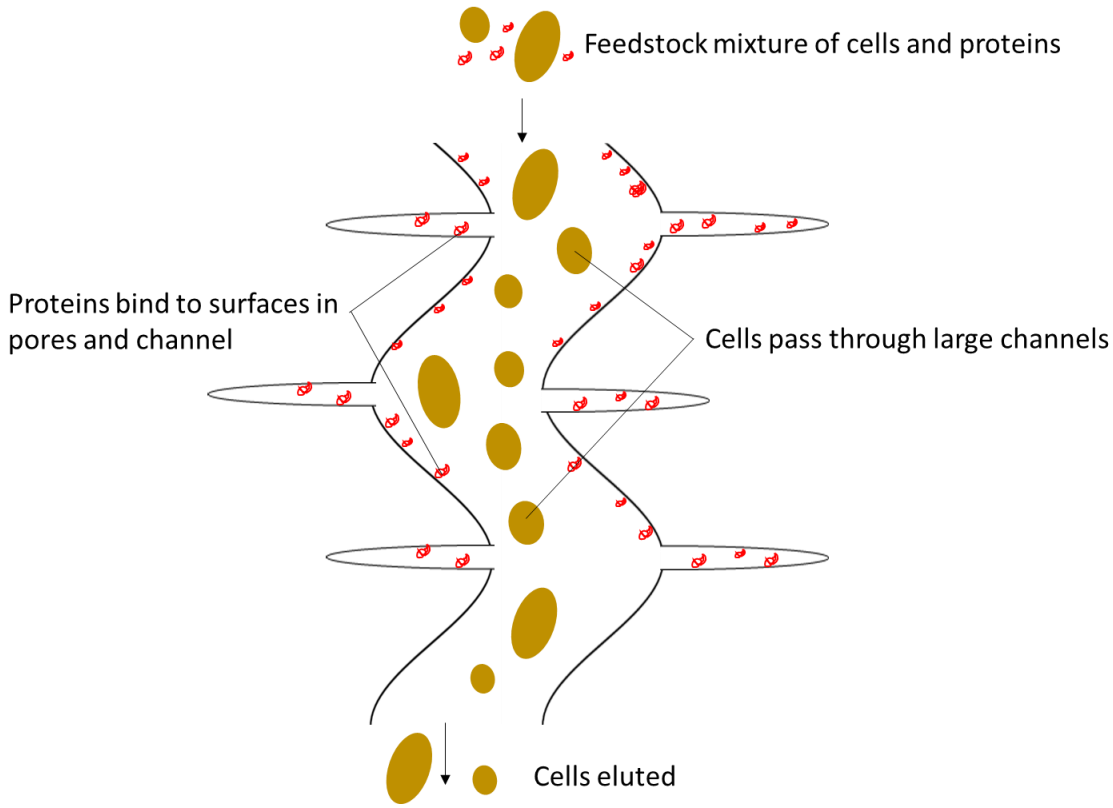


*Figure 1-4: Simplified gyroid channel with pores demonstrating protein binding and simultaneous cell passage (not to scale)*

## 1.2 Objectives

The overall aim of this thesis was to develop a chromatographic matrix with a controlled geometry which can be used as a combined suspended solids removal/primary protein capture step in the downstream processing of biologicals. More specifically, the aims are as follows:

- To prototype novel chromatographic matrices using a 3D-printing method to create various TPMS geometries from cellulose and agarose materials with varying channel diameters. TPMS geometries include Schoen gyroid and Schwarz diamond, and channel diameters range between 300 μm – 500 μm.
- To functionalise the columns for cation exchange, anion exchange, and hydrophobic interaction chromatography.
- To determine the maximum ion exchange capacities and protein equilibrium binding capacities for proteins of the columns.
- To quantify the effects of channel size and operating flowrate on column binding capacity by determining the dynamic binding capacity of proteins to the columns, and determining the optimum operating flowrate (ranging from 19.1 cm $h^{-1}$ to 763.9 cm $h^{-1}$) for protein adsorption.
- To understand the mechanisms that may limit protein adsorption in the columns such as mass transfer, adsorption rate, degree of functionalisation.
- To demonstrate the use of these prototype columns for solids removal with simultaneous protein capture.
- To quantify the effects of channel size and operating flowrate on cell passage in the columns and determining the optimum operating flowrate (ranging from 19.1 cm $h^{-1}$ to 763.9 cm $h^{-1}$) for 100% cell passage.
- To understand the mechanisms and limitations of cell passage through the columns such as cell sedimentation, interception, and impaction.
- To recommend an operating procedure for the columns based on experimental results which accounts for protein adsorbed, cell passage, and process operating time.

## 1.3 Organisation of Thesis

Chapter 2 of this thesis presents the literature surrounding those factors which influence the design, manufacture and testing of 3D printed chromatography columns. The history of chromatography is examined, and current state of the art explained. Then, alternative unit operations to the commonly used PBC are discussed, and how these alternatives offer

solutions to problems associated with PBC (although these alternatives are not without their faults). The techniques for functionalising agarose and cellulose for chromatography are explained, and 3D-printing techniques and development are discussed. TPMS are introduced, and their potential application to 3D-printed chromatography structures developed.

In chapter 3, experimental apparatus, materials and methods used to produce, functionalise, characterise and test the columns' adsorption performance and ability to act as solid-tolerant chromatography columns are explained. First, the column prototyping is analysed, showing how a 3D-printed template can be used to create complex TPMS columns from hydrogels. The column functionalisation procedure for cation exchange, anion exchange, and hydrophobic chromatography is described, along with the methods to measure ion exchange capacity and protein equilibrium binding capacity. Protein breakthrough experiments used to determine dynamic binding capacity of the columns is outlined, with a description of how fractions collected from runs are analysed using UV spectrophotometry. Methods for investigation into the limits of the functionalisation procedure are explained. Lastly, cell recovery experimental procedure is presented to determine the proportion of solids entrapped in the columns.

The next three chapters present the results and discussion for initial prototyping results, showing the successful manufacture of TPMS hydrogels, and characterisation of the adsorption under static conditions (Chapter 4). Chromatographic and adsorption efficiency of the columns are analysed under dynamic conditions to determine reduced plate height and dynamic binding capacity values, leading to an analysis of the mass transfer limitations on the columns (Chapter 5). The columns' abilities to act as solid-tolerant chromatography matrices is shown, and investigation into the controlling mechanisms for successful cell passage are analysed. These three chapters are followed by concluding remarks, with recommendations for future work in the development of TPMS hydrogels for solid-tolerant chromatography.

# Chapter 2. Literature Review

## 2.1 Chromatography

PBC is a separation process widely used across many industries. In a general chromatography process, a solution of different components (mobile phase) is passed over an insoluble material (stationary phase) to which each component has a different interaction. In PBC, the stationary phase is a spherical bead mixture ranging from 5 μm to 150 μm in diameter, packed randomly into a cylindrical column. The type of interaction between mobile and stationary phase depends on the chromatographic mode used, for example bio-specific affinity such as immunoglobulin G (IgG) to Protein A in affinity chromatography, or opposing electric charge between mobile phase component and stationary phase in ion exchange chromatography. Components that have a higher interaction with the stationary phase take longer to move through the column or are adsorbed to the column; hence a separation is achieved. Eventually, the components are eluted separately from the column and collected in fractions. For the context of this thesis, chromatography is mainly discussed as a downstream process in biotechnology where proteins are the desired components of the mobile phase (analyte).

### *2.1.1 Downstream Processing*

The production and manufacture of biological products is generally separated into upstream and downstream processing. At the centre of the process is usually a bioreactor, or other unit operation where a certain type of biological is grown to a high yield. Prior to the bioreactor are the upstream processes, which involve preparing a cell for growth (such as cell isolation, cell cultivation, inoculum preparation, media preparation), and after the bioreactor are the processes that separate the target molecule (for example a protein) from the culture medium to the highest purity possible. The basic downstream processing steps may include insoluble (for example cell and cell debris) removal, primary protein capture, further purification and polishing. Each step in upstream and downstream processing should be optimised to the produce the highest yield of product while minimising processing costs.

A schematic of a typical downstream process (Figure 2-1) shows adsorption and chromatography appear in the primary, intermediate, and final purification steps for extracellular products from fermentation [10]. This is often the case in the production and

purification of biological products: the different modes of chromatography such as ion exchange, affinity and size exclusion mean that chromatographic steps may be implemented to remove different contaminants from the initial cell culture or fermentation broth. The high usage of packed chromatography across the board in downstream processing makes it a key target for research and optimisation to reduce processing costs and increase yields.

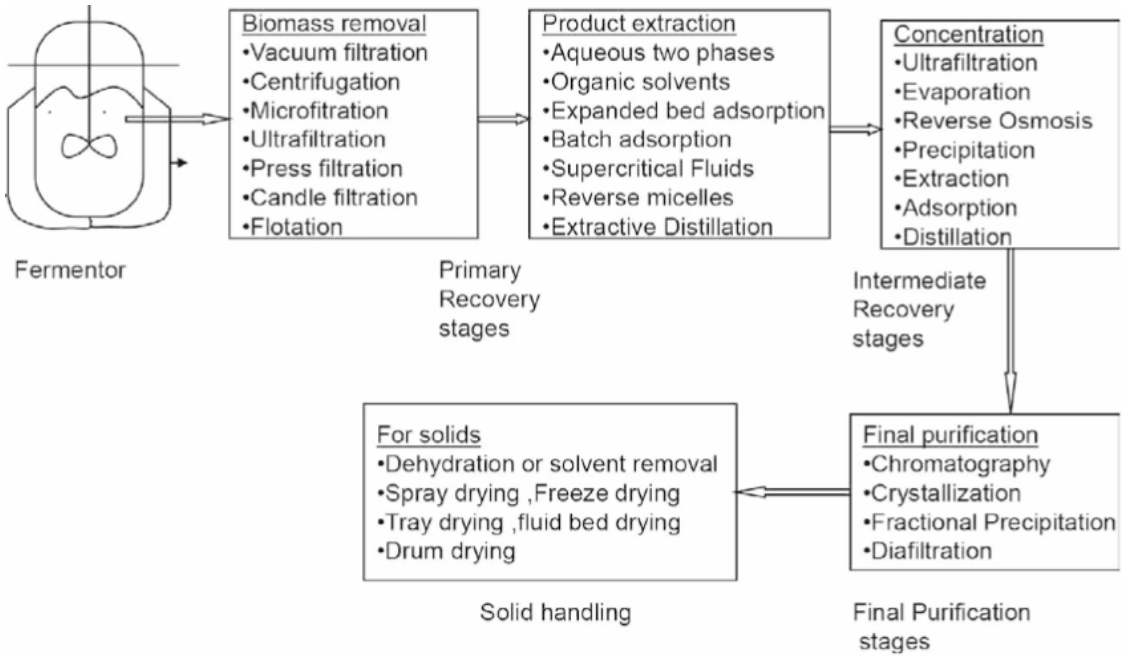


*Figure 2-1: Possible unit operations for downstream processing of extracellular products from fermentation [10]*

Despite its attractiveness and widespread usage, a bottleneck in the manufacture of biological products has been identified in downstream processing, because it is a slow and costly series of steps to purify biological products. 80% of cost of the processing costs arise during purification of high value biological products [3]. It is widely known that the cost of production increases and yield decreases with increasing number of unit operations [10]. Furthermore, there is no limit to the size of a bioreactor or fermenter, meaning as much of the target molecule could be grown or cultured, although there are size limitations on the unit operations used to purify these products [11]. Column chromatography was identified as the most serious contributor to that bottleneck based on a survey of 446 biopharmaceutical manufacturers from 35 countries conducted by BioPharma Associates [5]. Because of this, alternatives to such conventional processing steps as PBC are a highly sought-after area of research.

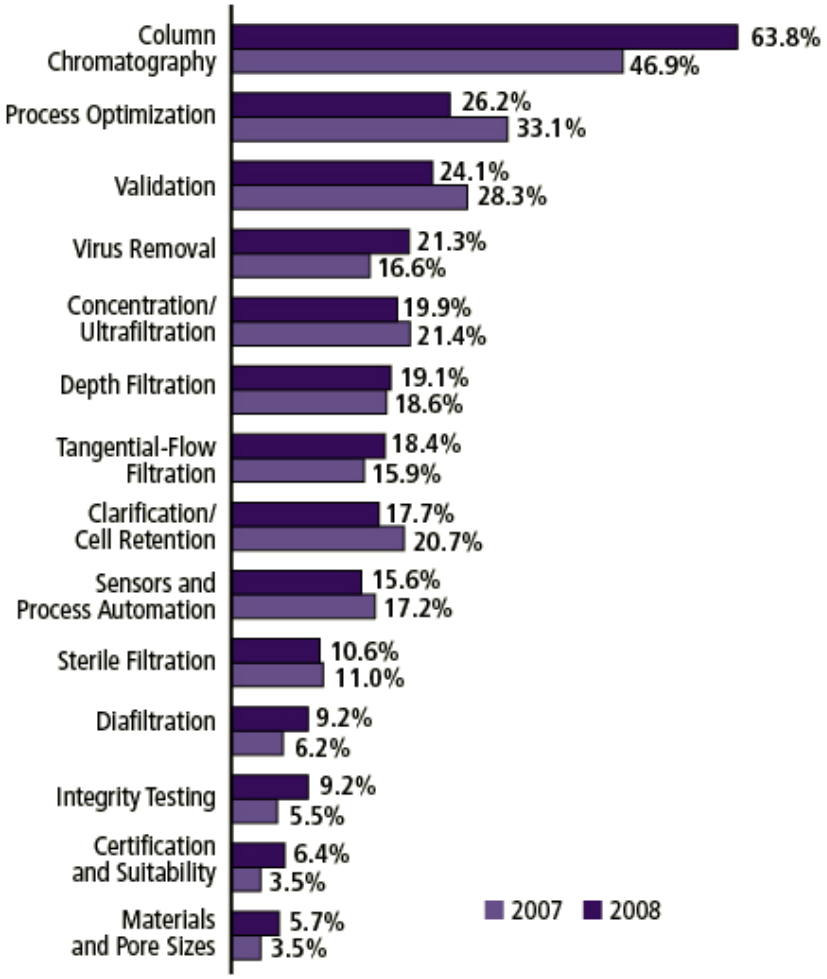


*Figure 2-2: Areas where downstream proccessing bottlenecks occur, according to respondents of BioPharma survery [5]*

In summary, PBC found a core application in protein capture, purification, and polishing phases for cell cultures and fermentation broths. The processes prior to the chromatography steps are important as they remove the cell debris from the mobile phase; if solids are present in the feedstock for PBC, they will cause blockages and reduce product yield. However as already stated, the removal of unit operations from the overall process is known to reduce product lost and reduce processing costs [12]. Despite its attractiveness and widespread usage, a bottleneck in the manufacture of biological products has appeared in downstream processing, and chromatography was identified as the main cause of this because it is a slow and costly series of steps to purify biological products. Because of this, alternatives to conventional processing steps such as PBC are an attractive area of research with great potential to improve downstream processing and the manufacture of biological products.

As it stands, PBC is the culmination of approximately a century's research into separation mechanisms, stationary phase types, and chromatographic hardware. It is an attractive processing option because of its success and range of applications, and the potential of replacing packed bed columns is seen as a risk by many in industry because of apparently unknown technologies and the high cost of retrofit. However, it is not without its disadvantages: PBC can be slow because the rate of adsorption is controlled by diffusion of analyte to the bead surface and the diffusion of analyte within the pore structure. Better mass transfer may be achieved by reducing the diffusion length through the particle, but if this were put into practice it would mean creating beads with shorter pores, essentially reducing the surface area to volume ratio inside the bed and decreasing the number of adsorption sites. In randomly packed beds there may be potential for dead zones to form in the bed, channelling can occur, and overall separation efficiency vastly reduced. Furthermore, the randomly packed nature of the resin bed means that 100% reproducibility in separation results cannot be achieved. This proves there is a lot of scope for research and development into alternative chromatography techniques, which is outlined later in this chapter.

### *2.1.2 Modes of Chromatography*

There are a vast number of methods that achieve chromatographic separation. These alternative methods are based on a variety factors: nature of the target molecule, polarity of buffer, composition of mobile phase, size of molecule, and many more. The main modes are outlined in Table 2-1 below, with the general mechanism and examples of immobilised ligands and sub-groups shown. The modes are then discussed in more detail in the following sections.

#### 2.1.2.1 Ion exchange chromatography

Ion exchange chromatography is perhaps the most widely used mode of chromatography. In typical downstream processing schemes, there are normally two ion exchange steps. The stationary phase is immobilised with a charged ligand, which targets solutes in the mobile phase with the opposite charge. There are two types of ion exchange: cation exchange and anion exchange; named such by the charge of the molecule attracted to the ligand. For example, a carboxy methyl (CM) ligand (negatively charged) attracts positively charged molecules, making it a cation exchanger. Cation and anion exchange are both divided into sub groups that describe the power of their interactions similar to how weak and strong acids and bases are described: weak and strong cation and anion exchangers. Common ligands for ion exchange include the carboxy methyl (CM), sulfopropyl (SP), diethylaminoethyl (DEAE), and quaternary ammonium (Q) (shown in Table 2-1).

*Table 2-1: Summary of modes of chromatography*

| Chromatographic Mode | Mechanism | Sub-class | Functional Group | Ligand |
|---|---|---|---|---|
| Ion Exchange | Opposite charges between adsorbent and adsorbate | Weak Cation | Carboxymethyl (CM) | 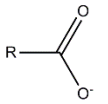 |
| | | Strong Cation | Sulfopropyl (SP) | 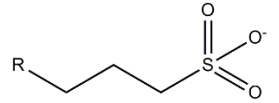 |
| | | Weak Anion | Diethylaminoethyl (DEAE) | 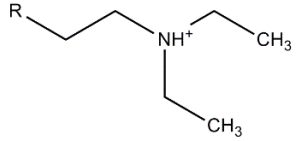 |
| | | Strong Anion | Quaternary ammonium (Q) | 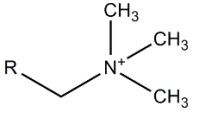 |
| Hydrophobic Interaction | Attraction between hydrophobic adsorbent and hydrophobic amino acid groups of adsorbate | Aliphatic | Octyl | 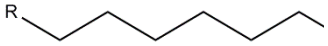 |
| | | Aromatic | Phenyl | 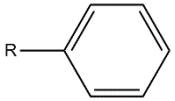 |
| Reverse Phase | Stronger interactions than HIC which require non-polar organic solvents for elution | Aliphatic | Octa-decyl (C-18) | 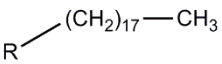 |
| | | Aromatic | Diphenyl | 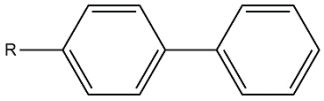 |

| | | | | |
|---|---|---|---|---|
| | | | DVB | 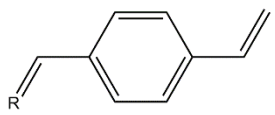 |
| | | Biologicals | Antigens, antibodies, protein A, enzymes, nucleic acids, proteins, lectins | |
| Affinity | Interaction between stationary phase and target molecule specific to adsorbate | Dyes | Cibracon Blue | 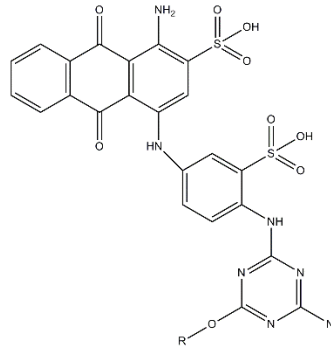 |
| Size Exclusion | Different size components of the mobile phase spend different amounts of time in column | Gel filtration | N/A - requires inert adsorbate with high porosity | |

General equations can show the procedure for ion exchange, whereby counterions associated to the oppositely charged functional groups are exchanged for the analyte in solution. An example is given in Equation 2-1 for a cation exchanger, where the counterion is $Na^+$, immobilised ligand is R and analyte is $X^+$:

$$\overline{Na^+R^-} + X^+ \rightleftharpoons \overline{X^+R^-} + Na^+ \quad (2\text{-}1)$$

The opposite equation applies to anion exchange chromatography, where the stationary phase is positively charged, an anion such as $Cl^-$ is the counterion, and analyte is negatively charged.

At the beginning of an ion exchange process, the stationary phase has counterions loaded on to the ligand binding sites, after which the column is equilibrated in binding buffer. The binding buffer should consist of low concentration salts (such as 20 mM), in order to reduce the ionic strength of the solution yet enable appropriate buffering capacity. The mobile phase sample is loaded onto the column; the target molecules bind to the ion exchange ligand, displacing the counterions. The column is then washed in binding buffer to remove any unbound sample. To recover the bound molecule, a high salt concentration elution buffer is applied to the column, which increases the ionic strength in the bulk phase, drawing the adsorbed molecule from the ligand back into solution, replacing the molecule with counterions at the same time.

#### 2.1.2.2 Hydrophobic Interaction Chromatography

Hydrophobic interaction chromatography (HIC) is primarily seen in protein purification for molecules with a high number of hydrophobic amino acid groups. In this mode of chromatography, target proteins are captured in order of hydrophobicity (ie number of hydrophobic amino groups such as alanine, valine, leucine, isoleucine, proline, phenylalanine, methionine, and tryptophan). Hydrophobic amino acids contain hydrophobic side chains, which are usually buried inside the folded protein structure. In the hydrophobic interaction chromatography process, the protein is dissolved in a high-salt buffer in order to change the folded structure where the hydrophobic groups become closer to the surface. Ligands that have long carbon chains (commonly butyl or octyl) or aromatic rings (phenyl) are immobilised to the stationary phase, to which the hydrophobic proteins bind.

The hydrophobic strength of the buffer can be manipulated by controlled salt type and salt concentration. Salts such as ammonium sulfate promote hydrophobicity compared with salts such as sodium chloride and sodium sulfate. In order to elute the proteins, the salt

concentration of the mobile phase is gradually reduced (hence hydrophobicity of mobile phase is gradually reduced), and proteins elute in order of reverse hydrophobicity.

#### 2.1.2.3 Reversed Phrase Chromatography

Reversed phased chromatography is named such because most other chromatographic techniques (ion exchange, affinity, etc.) are considered "normal phase". This is because a polar mobile phase is used as the equilibration and binding buffer, while the elution buffer consists of an organic solvent such as acetonitrile, tetrahydrofuran or methanol, which is miscible in water.

The stationary phase in reversed phase chromatography is immobilised with a highly hydrophobic ligand such as a C-18 chain, or multiple aromatic rings (e.g. divinyl benzene). Although reversed phased chromatography is not often seen in protein chromatography, it is a useful tool in HPLC because it can purify and analyse solutions of fats, lipids, cobalamins, and other complex biomolecules. It is not generally used in preparative protein chromatography because the solvents used denature the proteins.

#### 2.1.2.4 Affinity Chromatography

The development of affinity chromatography resulted in a large change in downstream processing. Because of advances in ligand immobilisation, almost any molecule could be immobilised to a stationary phase, particularly ligands with a specific affinity to one or a small group of biomolecules.

Perhaps the most important development in affinity chromatography was the immobilisation of Protein A from *Staphylococcus aureus*, because when bound to a stationary phase it can capture immunoglobulins from mammalian species, particularly IgGs which have several therapeutic uses. Other types of ligands seen in affinity chromatography include dyes such as Cibracon blue which captures BSA and Procion red, enzymes such as pepsin and proteases, and nucleic acids.

The downside of affinity chromatography is the ligands typically used are very expensive to source. This makes it less attractive as an option for the chromatography columns made in this research; however, it is a very useful tool, and development of 3D-printed affinity columns should be considered in the future.

#### 2.1.2.5 Size Exclusion Chromatography

The only mode of chromatography that requires an inert matrix is size exclusion chromatography, where components of the mobile phase are separated based on their size. The resin is a porous packed bed, which when a mobile phase is applied to the column, larger molecules flow through the column because they cannot penetrate the pores of the resin, while smaller molecules spend more time in the column because they interact with the smaller sized pores. A common application of size exclusion is desalting protein solutions: the protein is eluted from the column earlier than the salts because the protein size is significantly larger than the salt.

### *2.1.3 Stationary Phases*

The stationary phase is the solid phase packed into a column casing, typically made up of small, spherical beads. It is often referred to as the "matrix" and is the base material to which a ligand may be covalently attached or immobilised. There is an extremely large range of materials used as stationary phases in chromatography, from natural materials such as agarose and cellulose, ceramic based materials like silica and alumina, and synthetic polymers such as polyamides and polystyrene. As with the mode of chromatography, the application often determines the choice of stationary phase material. However in this research, the ability of the stationary phase material to be used in a 3D-printing technique to produce a controlled geometry is of equal importance. This section looks at the properties important in a stationary phase material and discusses specific properties of hydrogel materials cellulose and agarose in the context of their uses as chromatography stationary phases and their ability to be constructed into a controlled geometry using a 3D-printing method.

The properties important to the performance of the stationary phase include:

- Ease of functionalisation/ligand immobilisation;
- Good mechanical stability;
- Good chemical resistance;
- Even pore size distribution and bead size;
- High surface area;

The ease of functionalisation is key in chromatographic processes that require ligands for adsorption of analytes in the mobile phase to the stationary phase. A ligand is covalently attached to a functional group in the matrix polymer chain, and commonly cited groups easily

functionalised include primary alcohols, carboxylic acids, and primary amine groups. Alcohols are abundant in many polysaccharide chains (for example agarose and cellulose), carboxylic acid groups appear in polymethacrylates, and amine groups are present in chitosan and polyacrylamide. Methods for the functionalisation of the different stationary phase materials are discussed in Section 2.3.

Mechanical stability determines how well the stationary phase can withstand high pressures and flowrates without compacting or breaking. Hydrogel structures do not generally have high mechanical stability; however, this may be improved by crosslinking the polymer structure.

Stationary phase materials require good chemical stability because of the types of chemicals used in the functionalisation procedure as well as the chromatography process. Some functionalisation procedures require immersion in pure acetone, extreme pH ranges (often pH 1-14) and exposure to oxidising conditions. During a chromatography run, buffers containing acetonitrile are common, and cleaning processes expose the column to strong alkaline conditions which can break down some polymeric chains and hydrolyse immobilised ligand groups. As well as having good chemical resistance, the matrix must be insoluble in functionalisation solvents and chromatography buffers.

Uniformity in pore size and bead size is not crucial to all types of chromatography, but it can impact the separation efficiency in size exclusion chromatography because the pore size determines which molecules can be separated by molecular weight (ie size). If the pore size is not uniform or within specification, the molecules cannot be effectively separated. Uniformity in bead size is important in maintaining uniform flow characteristics by keeping a constant voidage between the beads. As voidage varies, so does interstitial velocity, meaning mass transfer properties change which can have a detrimental effect on adsorption processes that are mass-transfer limited.

High surface areas are required for stationary phases to provide enough binding sites for adsorption. High surface area can be achieved by using materials with a high porosity; some materials such as agarose and cellulose hydrogels have a natural porosity, while other materials require the addition of a porogen. The porogen is added to the monomer mixture before polymerisation, then dissolved away after polymerisation, leaving a porous structure. Examples include parrafin beads as a porogen for poly-lactic acid (PLA) [13] and cyclohexane or toluene as a porogen for polystyrene divinylbenzene [14]. Pore size can easily be controlled using a porogen, by selecting a porogen with an appropriate diameter. In

hydrogels, pore size is controlled by the amount of the material dissolved in water (for example 6% w/w agarose in water) and the degree of crosslinking, and gelation temperature.

Non-specific binding refers to the ability of an undesirable protein or analyte to bind to a binding site competitively with the desired analyte. This is often a function of the inherent charge or hydrophobicity of the matrix and can be unpredictable if the composition of the mobile phase is unknown. Polystyrene is commonly taken advantage of because of its non-specific binding abilities to antibodies. Non-specific binding can also be caused because of the ligand type or immobilisation procedure which will be discussed in Section 2.3.1.

These properties are all important in selecting a stationary phase material appropriate for chromatography, however the challenge presented to this work is selecting a material suitable for chromatography that may also be 3D-printed with relative ease. Properties of a material suitable for 3D-printing are determined by the type of printing method (for example extrusion, selective laser sintering, and photo-curing). The potential for the stationary phase materials discussed hereafter to be crafted into a controlled geometry is discussed below.

Typical stationary phase materials with their properties are shown below (Table 2-2), where the pH stability range, inherent properties of the matrix, typical synthesis route of the matrix, and surface functional groups are stated. The table gives a range of stationary phase classes (natural, ceramic, and synthetic), functional groups (such as alcohol, amine, carboxylic acid), and inherent properties (hydrophilic, hydrophobic, and amphoteric).

*Table 2-2: Properties of typical stationary phase materials for chromatography (adapted from Fanali et al [15])*

| Class | Resin Material | Stability range | Inherent Properties | Synthesis or Manufacture | Functional Groups |
|---|---|---|---|---|---|
| Natural | Agarose | pH 0-14 | Hydrophillic | Sol-gel | Alcohol |
| | Cellulose | pH 3-10 | Hydrophillic | Sol-gel | Alcohol |
| | Dextran | pH 0-14 | Hydrophillic | Sol-gel | Alcohol |
| Ceramic | Silica | pH 1-9 | Hydrophillic, cation exchange | Sol-gel or template assisted synthesis | Silanol |
| | Alumina | pH 2-12 | Amphoteric, cation and anion exchange | Thermal decomposition of gibbsite or boehmite | Acidic and basic sites |
| Synthetic | Polystyrenes | pH 0-14 | Hydrophobic | Polymer emulsion and crosslinking | Styrene, often crosslinked with divinyl benzene |
| | Polyacrylamides | pH 0-14 | Hydrophilic | Polymer emulsion and crosslinking with sol-gel process | Amine |
| | Polymethacrylates | pH 2-12 | Hydrophilic | Polymer emulsion and crosslinking | Carboxylic acid |

Agarose and cellulose hydrogels were decided as the material for controlled geometry structures to be made from, given their pH stability range, the relative ease of the sol-gel process to be transferred to a 3D-printing method, and the range of functionalisation methods available for the alcohol groups in the polysaccharide chains. Furthermore, both agarose and cellulose are widely used and commercially acceptable chromatography bead materials.

#### 2.1.3.1 Natural Hydrogels

##### *2.1.3.1.1 Agarose*

The polysaccharide agarose is a naturally occurring polysaccharide derived from seaweed. It is a very commonly used material in chromatography because of its high porosity and ability to be chemically modified while maintaining high chemical stability. Agarose is a polysaccharide sourced from seaweed, made from repeating D-galactose and 3-anhydrogalactose units (Figure 2-3). As a hydrogel, it forms a stable, highly porous

structure. The primary and secondary alcohols (hydroxyl groups) on each ring can be modified using appropriate functionalisation techniques, meaning a range of chromatographic functionalities can be employed with agarose stationary phases. It is common to see agarose modified for all modes of chromatography; Sepharose beads by GE Healthcare are immobilised with CM, DEAE, SP, Q, Protein A, butyl, or octyl ligands to make ion exchange, affinity, and hydrophobic interaction resins [16]. Agarose is a widely used, robust stationary phase, with a proven track record in chromatographic separations.

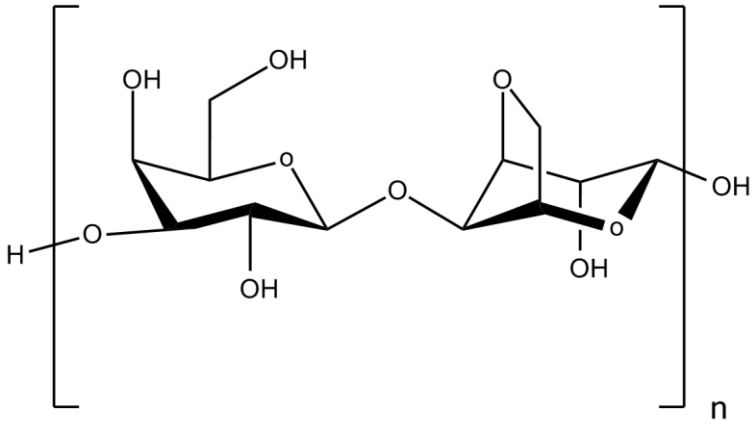


*Figure 2-3: One unit of agarose, showing a D-galactose molecule and a 3-anhydrogalactose molecule*

In general, commercially available agarose beads such as Sepharose are made from 6% w/w agarose, crosslinked with epichlorohydrin in order to increase mechanical stability. The downside of using chemical crosslinkers is that the number hydroxyl groups free for ligand immobilisation is reduced, as the cross-link is achieved between the hydroxyl units of each chain. It is reported that up to 30-50% of hydroxyl groups are consumed during crosslinking. This means that there are fewer sites available for ligand immobilisation.

Agarose is a robust stationary phase material. Its pH stability range covers pH 0-14, has an average pore size of 300 Å, and can be made in to a large range of bead sizes. Small agarose beads on the order of 25 μm to 45 μm are used for high performance liquid chromatography (HPLC), while larger beads ranging between 45 μm and 300 μm can be used for process chromatography.

The synthesis of beaded agarose is simple: agarose power is water soluble at approximately 60 ˚C, because the hydrogen bonds break upon heating, allowing solution of agarose in powdered form to be dissolved in water. Upon cooling, hydrogen bonds reform in the sol-gel

transition and the solution may be cast into different shapes. This property may be taken advantage of in 3D-printing using a fused deposition modelling technique.

#### *2.1.3.1.2 Cellulose*

Cellulose is a polysaccharide made up of repeating D-glucose units (Figure 2-4). It is a naturally occurring polymer, being the main component of the cell wall in plants. The primary and secondary alcohol functional groups provide many options for ion exchange functionalisation [17]. Cellulose is generally used in a "regenerated" form, whereby cellulose is dissolved in a solvent where it can be chemically modified, and then regenerated to a desired form (this process is also used to make cellulose hydrogels). Because of its similarity to agarose, the functionalisation opportunities for cellulose are vast. However it is not as widely used as a chromatographic support due to its lower pH stability, and being more difficult to handle without breakages [18]. Cellufine is a major manufacturer of regenerated beaded cellulose resins, with their range covering all types of ion exchange, phenyl and butyl hydrophobic interaction, and affinity resins for virus and nucleic acid capture [19]. Cellufine states that cellulose has superiority over other polymeric resins because ligand leaching is less likely [19].

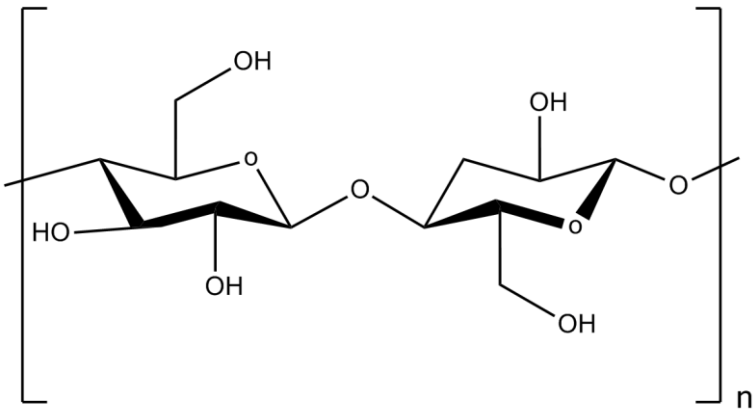


*Figure 2-4: Two D-glucose units demonstrating the chemical structure of cellulose*

Cellulose hydrogels are produced by dissolving cellulose powder in a solution of 8% NaOH and 12% urea at -12 °C. The solution is mixed thoroughly and then cast into a desired shape and left to gel at up to 70˚C. The gelling rate may be increased by exposing the gel to higher temperatures. The gel is then regenerated in water to make a hydrogel: water is absorbed, causing the gel to swell, increasing the pore size. The gel may also be crosslinked using either a chemical or physical crosslinker. Epichlorohydrin (ECH) is used as a chemical crosslinker, and extra cellulose powder acts as a physical crosslinker. Work conducted at the University

of Canterbury has shown that the type of crosslinking, amount of crosslinker, gelling temperature and gelling time are all important in determining the microstructure of the hydrogel, which would have a major effect on the chromatographic performance [20].

The physical nature of the material makes it attractive for a 3D printing option as well as chromatography: as a hydrogel it is highly porous and may be made into a mechanically strong polymer. The gelling process means that either fused deposition modelling or stereolithography may be used: these processes take advantage of a change in temperature to change the structure of the liquid to a solid gel, held together by the hydrogen bonds in the cellulose matrix; these bonds can be further strengthened by chemical or physical crosslinking. Recent success has been reported taking advantage of this process by using a LASER beam to thermally gel cellulose into controlled geometry structures up to 100 μm feature size [21].

### 2.1.4 Alternatives to Packed-bed chromatography

The alternatives to PBC discussed in this section are monolithic chromatography and expanded bed adsorption. Other alternatives do exist, such as membrane chromatography, fibre chromatography, and cryogel chromatography; however, these are not discussed. In theory, these processes can be superior to PBC because they reduce mass transfer limitations often associated with PBC. Expanded bed adsorption (EBA) is furthermore attractive because it combines primary protein recovery with solids removal. This was outlined by Spalding as a way to achieve economic success in downstream processing because it reduces the number of unit operations [22]. This manifests as a process that tolerates suspensions containing solid particles and provides an initial protein capture step with clarified protein concentrate that can be transferred to subsequent processes [4]. Although centrifugation is good for solids removal of large cells (such as yeast), as the cells get smaller, centrifugal separation performance is decreased significantly, meaning there are more likely to be cell impurities in the product supernatant, or target protein lost in the cell debris waste [3]. Furthermore, there is an advantage in not subjecting the cells and proteins to centripetal forces that can disrupt their functionality. In filtration processes, non-specific binding of protein and cells to the filter medium can occur, meaning product is lost. Therefore, processes such as expanded bed adsorption is attractive because less product is lost.

#### 2.1.4.1 Monolith Chromatography

Monolithic structures are widely used in other chemical engineering practices, such as other separation devices and flow-through reactors [23-25]. Monolithic chromatography uses a stationary phase made of a single plug of permeable channels, rather than a randomly packed bed of spherical beads. The channel diameters in typical monolith columns are of a similar order to that of the pores in beaded resins, as demonstrated in the figure below (Figure 2-5).

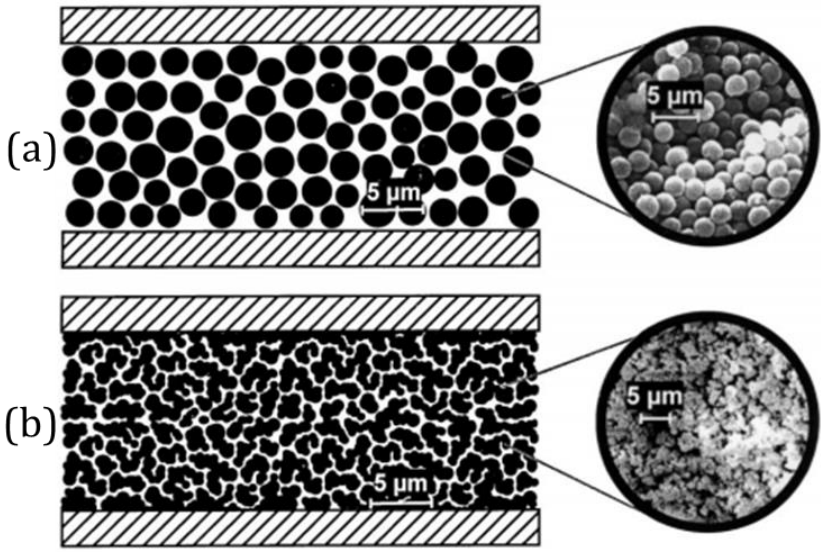


*Figure 2-5: Structural differences in (a) packed bed columns and (b) monolithic columns [26]*

In PBC, approximately 30% of the stationary phase is interstitial voids (i.e. area between the beads), which is an inefficient use of space within the column because there is no adsorption occurring in these volumes [27]. Furthermore, beads are often limited by diffusion rates to the bead surface and within the pores of the beads because convective mass transfer dominates in the void space, while diffusion through the pores is comparatively slow. The principles behind monolithic columns overcome both limitations: interstitial voidage is greatly reduced because of using a single plug of material, and the use of permeable channels means that the mobile phase is pumped through all the channels in the material and mass transfer is achieved by convection, rather than being limited by slow diffusion. Therefore, mass transfer and adsorption rates are faster because of the lowered interstitial voidage and increased rate of penetration through the entire column, hence overall chromatographic efficiency is improved.

Initial testing of monolithic structures showed that fast chromatographic separations could be achieved at moderate back pressures [25, 27-29]. A monolith column was prepared with

the permeability equal to that of a packed bed of 5 μm particles, with the separation power of a packed bed of resin particles half the size [30].

However, the main challenge to overcome in monolithic chromatography is to reduce the column back pressure which is generally quite high, demonstrated in Darcy's Law (Equation 2-2), where, long columns, high flowrates, and low permeability all yield large pressure drops.

$$\Delta P = \frac{F_0 \mu L}{\kappa A} \tag{2-2}$$

In Equation 2-5, $\Delta P$ is the pressure drop across the monolith column, $F_0$ is the volumetric flowrate, L is the length of the monolith column, $\kappa$ is the permeability of the monoliths, and $A$ is the cross-sectional area of the monolith column. From a practical point of view, large pressure drops are undesirable because they lead to bed compression, deformation, and breakage. This issue has still not been overcome in monolithic chromatography, because the low permeability yields high pressure drops.

The current manufacturing method for monolithic columns does not ensure every column is identical: usually a synthetic polymer is used with a porogen to add the pores. This means column-to-column reproducibility for protein capture and chromatographic performance is not ensured. This gives it the same limitation as PBC. 3D-printing methods would be beneficial in monolithic chromatography to ensure each column is identically produced.

#### 2.1.4.2 Expanded Bed Adsorption

Expanded bed adsorption was introduced as a unit operation to achieve primary capture of products from unclarified feedstocks in downstream processing. The first reported use was in 1987 where Wells et al. developed agar particles suitable for fluidisation and adsorption of yeast cell proteins [31]. The stationary phase is fluidised to a constant expanded state, increasing the interstitial volume between stationary phase particles. As the unclarified mobile phase is applied to the column, the cells and cell debris pass through the voids caused by fluidisation, and proteins bind to the porous stationary phase. Following protein capture, the flow adapter reduces the column volume, compressing the adsorbent back to a packed state where the bound molecules are eluted, and adsorbent is regenerated. This process is demonstrated in the figure below (Figure 2-6).

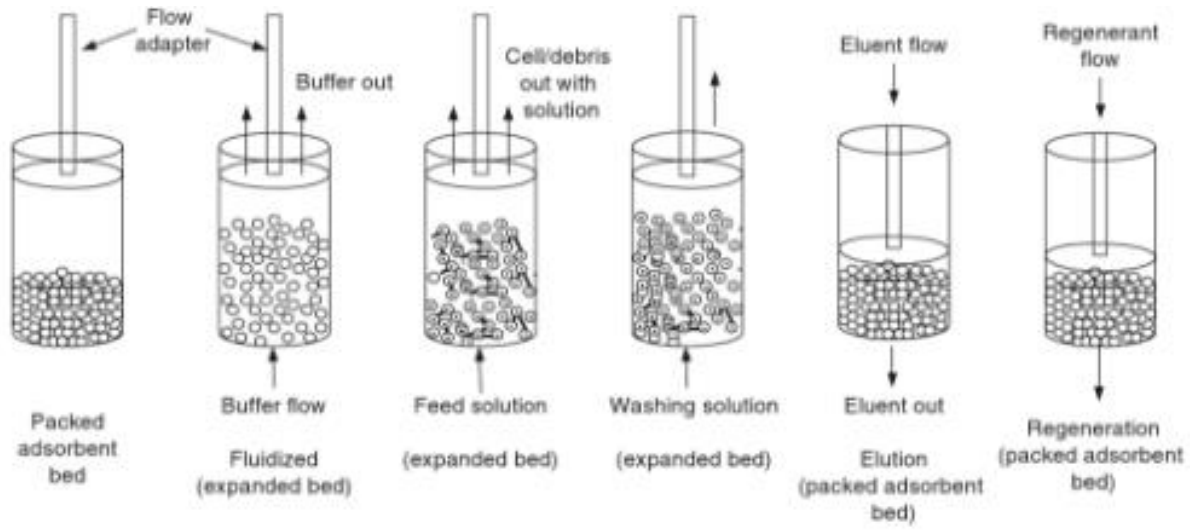


*Figure 2-6: Process progression for expanded bed adsorption. Packed adsorbent is fluidised in buffer flow; feed solution is applied to the expanded bed which is washed in buffer. Bed is then packed and target protein eluted and bed regenerated [32].*

In the initial development of expanded bed adsorption, several successes were reported by a series of research groups. Performance parameters indicating EBA would be successful include:

- Protein adsorption efficiency unhindered or improved compared with PBC
- Fluidisation behaviour stable, follows Richardson and Zaki theory
- Stationary phase resilient to fluidisation cycles and CIP cycles
- Stationary phase not fouled
- Stationary phase not entrained with fluidised cells
- Cells undamaged

Key findings proved that protein adsorption efficiency is not hindered; perhaps because the cells are too large to penetrate the pores of the stationary phase, so do not reduce ion exchange capacity. Initial success in the development of EBA as an attractive unit operation for integration into DSP are summarised in the Table 2-3 below.

Summarising these studies shows clear successes in expanded bed adsorption. Target protein capture was increased in several studies, productivity was improved by reducing cycle times (which in some cases even meant quality of the product was improved, such as protease activity), cells were recorded to be undamaged, and methods to maintain bed stability were recorded. Affinity, cation and anion exchange chromatography with different stationary phase materials (agarose and silica) were widely proved to be successful. These weren't

*Table 2-3: Summary of expanded bed adsorption success*

| Product | Protein Source | Stationary Phase | Performance | Comments | Authors |
|---|---|---|---|---|---|
| Streptomycin | *Streptomyces* | Cation exchange | 12% increase in streptomycin yield | Added distributor at column outlet to break up aggregates | [6] |
| Novobiocin | *Streptomyces* | Anion exchange | 57% increase in yield | Large insolubles initially removed on a vibrating screen | [7] |
| Fusion protein | *Escherichia coli* | Streamline DEAE | 90% product yield | Feedstock diltued to reduce ion strength for successful ion exchange EBA | [33] |
| Annexin V | *Escherichia coli* | Streamline DEAE | >95% product yield | Investigated biomass loading into fluidised bed stability investigated - 5% biomass OK, and fluids with low viscosities (less than 0.01 kgm-1s-1) | [34] |
| Recombinant human interleukin 2, anti-Tac(Fv), *Pseudomonas* exotoxin fusion protein | *Escherichia coli* | Interleukin 2 receptor immobilised on Prosep-CHO activated controlled pore glass | Competitive recovery compared with PBA with clarified extracts | Protein were refolded and the crude extract purified using EBA | [35] |
| Phosphofructokinase | *Saccharomyces cerevisiae* | Cibracon Blue Sepharose FastFlow | 10 fold purification of enzyme observed | 5% yeast feed, 1.8 fold reduction in process volume | [36] |
| Protease | *Yarrowia lipolytica* | DEAE Spherodex | Similar protease recovery compared with fixed bed | 2.5 fold faster processing, and higher specific activity of the enzyme because of less autolysis due to shorter processing time | [37] |
| glucose-6-phosphate-dehydrogenase | *Saccharomyces cerevisiae* homogenate | Procion red agarose | 103 fold purified enzyme, 98.8% yield | Pseudoaffinity interaction | [38] |
| Aprotinin | *Hansenula polymorphia* | Streamline SP | 68% yield | 4 fold increase in purity, 7 fold increase in concentration | [39] |

| | | | | | |
|---|---|---|---|---|---|
| Antibodies | CHO cells | Protein A covered Prosep glass | Equal to PBC recovery | Take advantage of MAb-protein interaction at pH 7, and cells not damaged | [8] |
| HSA | Human blood plasma | DEAE sepharose | 95% recovery at 85% purity | Blood had to be diluted 10 fold to be able to be used at a reasonable capacity | [40] |
| α-lactalbumin and β-lactoglobulin | Bovine whey | Spherosil QMA (anion exchange) | Higher productivity yielded | Bed stability increased by static mixers and successful scale up was demonstrated | [41] |
| Human IgG | CHO cells | ProteinA Sepharose | Equal to PBC recovery | Fluidisation stability was ensured, and flow characterised as ideal plug flow confirming the Richardson and Zaki theory. [42] | [43] |

without changes in processing techniques, for example in Bartels work aggregates formed in fluidised bed with untreated broth on the cation exchange resin, meaning an agitator was used at the entrance to the column to prevent settling and blockages. This change in operation gained a 12% increase in Streptomycin yield compared with the fixed bed case [6]. In practical terms, EBA appeared to be a highly successful alternative to PBC.

A study into the economic benefits of EBA showed that integrating the process into systems with existing filtration and PBC is superior when the EBA column operates anywhere from above 30% of its design capacity in the capture of BSA in a solution with *Pichia pastoris* [12]. Because the implementation of EBA was likely to be retrofitted into existing processes means that economic analyses should also consider the cost of refitting a plant with EBA hardware (despite claims made that EBA could easily fit into existing chromatographic hardware), and loss of productivity while new equipment is installed. Mustafa concluded that the net present value of EBA technology relative to PBC would be larger provided a facility was out of production for less than seven months. This took into account the increased process yield achieved in EBA [44]. From these studies the economic viability of EBA is verified.

One of the key challenges in EBA development was minimising cell-adsorbent interactions, and Chase and Feuser showed that the adsorbent selection is important in minimising these interactions [45, 46]. Chase and Draeger show that protein adsorption efficiency on expanded bed Protein A Sepharose Fast Flow is similar to that of packed bed when purified as an unclarified broth [47]. Likewise, a cation exchanger had little interaction with *S. cerevisiae* and *E. coli* when in concentrations less than 5 mg/ml. On the other hand, numerous reports of cell binding were recorded by Chase and Draeger while analysing BSA adsorption onto Q-Sepharose (anion exchanger). In the presence of *S. cerevisiae*, *E. coli* and *Alcaligenes* protein breakthrough was recorded earlier for high concentrations of cells, and the static binding capacity was greatly reduced (49% reduction in BSA absorbance to Q-Sepharose was observed). This is due to the net charge of cells in anion exchange buffering conditions, often causing them to become negatively charged and bind to the anion exchange resin [36, 43, 48]. In Feuser's work, cell binding to Q-Sepharose was reduced by increasing the salt concentration in the binding buffer; however, makes no comment on the effect of protein binding in higher salt conditions which is likely to be reduced in ion exchange chromatography [46]. Tari et al. explored this in more detail and found an optimum salt concentration of 150 mM NaCl in binding buffer to enable capture of BSA with *S. cerevisiae* cells remaining unbound [49].

Unfortunately, EBA was never seen as an attractive process to be fully integrated to mainstream downstream processing due to several factors outlined below:

- EBA does not get around the problems of viruses and endotoxins in the final product, therefore processing surrounding this still required.
- Ligand selection may be difficult.
- There are specific situations where EBA is not applicable because of specific properties of the biomass in the feedstock [45].
- Intensive clean-in-place (CIP) causing chemical deterioration of stationary phase.
- Blockages occurring, destabilising the fluidised bed, causing channelling and collapse of fluidised bed [4].
- Cells becoming damaged because of high shear forces.
- Cation exchange capacity of certain cells hindering performance.

Although EBA did not successfully solve the problem achieving primary capture of target proteins from unclarified feedstocks, this principle remains interesting and is the basis behind the chromatographic structures designed in this research.

#### 2.1.4.3 3D-Printed Adsorptive Media

The idea of creating adsorptive media using 3D-printing techniques was hypothesised to overcome the bottleneck in chromatography processes by printing a controlled geometry structure, where flow paths and chromatographic efficiency could be optimised using computational fluid dynamics (CFD) [9]. Porous bed structures could be printed to easily fit into existing chromatographic hardware, meaning widespread implementation would not require large disruption in analytical and preparative processes. The work presented later in this thesis is patented [50], and there is continued investment and development in this area, and it is leading to the use of 3D-printing techniques to be used to produce microstructures in other chemical and process engineering operations [51].

### *2.1.5 Measuring Chromatographic Performance*

#### 2.1.5.1 Static Performance

Chromatographic performance of ion exchangers is cited under both static and dynamic conditions. In the static case, the ion exchange capacity and equilibrium binding capacity are used. The ion exchange capacity is the maximum number of ions that can bind to the ion exchanger, or the maximum ligand density, assuming a 1:1 exchange ratio between ion and

resin which is valid for small ions. The ion exchange capacity is the number of ions that may be exchanged per unit mass or volume of the stationary phase, referred to as "equivalent" units of ion. The equilibrium binding capacity refers to the maximum amount of solute that may adsorb to the resin.

All modes of chromatography except for size exclusion chromatography use adsorption theory to model the binding behaviour of target molecules to the stationary phase. If monolayer adsorption is assumed, then Langmuir behaviour is observed. This is given in Equation 2-3 for a single analyte.

$$q = \frac{q_e K C}{1 + KC} \tag{2-3}$$

Where $q$ is the concentration of the analyte on the stationary phase, $q_e$ is the maximum concentration of adsorbate bound to the stationary phase (at equilibrium), $C$ is the concentration of the adsorbate in the mobile phase, and $K$ is the equilibrium constant relating at adsorption and desorption rates (Equation 2-4):

$$K = \frac{k_{ads}}{k_{des}} \tag{2-4}$$

The Langmuir isotherm indicates that there is a maximum amount of adsorbate that can bind to a stationary phase. Fitting data to this isotherm is used to report maximum binding capacities of commercially available chromatographic resins.

However, in the case of protein ion exchange the protein size, shape, and charge distribution means that 1:1 ion exchange does not occur. Two factors influence the number of binding sites a single protein adsorbs to: the effective charge of the protein ($\nu$), and its steric hindrance ($\sigma$). The effective charge arises because complex amino acid sequence in protein yields multiple charged sites at a given pH [52]. Steric hindrance occurs because proteins are large molecules which can shield binding sites and repel like-charged proteins. These effects are modelled by the steric mass action (SMA) model, where the maximum binding capacity of a molecule, $q_{e,i}$, is found by dividing the maximum ion exchange capacity of the resin, $q_{max}$, by the sum of the steric hindrance and protein effective charge (Equation 2-5). The maximum ion exchange capacity may be determined by acid-base titration, and steric mass action model parameters determined by adsorption experiments at different salt concentrations.

$$q_{e,i} = \frac{q_{max}}{z_i + \sigma_i} \tag{2-5}$$

Because of the steric mass action law, a modified Langmuir model can be applied, given in Equation 2-6:

$$q = \frac{K_e[q_0 - (z+\sigma)q]^z C}{C_s^z} \tag{2-6}$$

Where $K_e$ is the affinity constant, determined by the analyte's affinity to the mobile phase which can be a function of salt concentration, pH, and ligand dissociation. $C_s$ is the salt concentration in the mobile phase.

In some cases, adsorption behaviour does not fit Langmuir behaviour. In these instances, Freundlich (Equation 2-7) or BET (Equation 2-8) adsorption theories may be used to model the behaviour. Freundlich does not have a mechanistic basis; rather it is purely derived on an empirical basis.

$$q = aC^{\frac{1}{b}} \tag{2-7}$$

Where $q$ and $C$ are defined as before, and $a$ and $b$ are empirical constants. Note that the nature of this isotherm means there is no theoretical maximum binding capacity.

$$q = \frac{q_e K C}{\left(1 + KC - \frac{C}{C_s}\right)\left(1 - \frac{C}{C_s}\right)} \tag{2-8}$$

In Equation 2-8, $q_e$ is the monolayer adsorption capacity, $K$ is the equilibrium constant, $C_s$ is the mobile phase concentration at the stationary phase surface. This is the BET isotherm and can be used for multilayer adsorption. For the stationary phases made in this research, adsorption behaviour will be modelled based on one of the above isotherms.

#### 2.1.5.2 Dynamic Performance

##### *2.1.5.2.1 Mass Transport in Chromatography*

Quantification of chromatographic matrices under dynamic conditions requires a brief understanding of the mass transfer systems that occur between the mobile phase and stationary phase. In a porous medium, there are a series of mass transfer steps between the analyte in the mobile phase and the analyte adsorbed to the stationary phase ligand, demonstrated schematically below (Figure 2-7). Typical mass transfer mechanisms for chromatography are:

- Advective transport due to bulk fluid motion in interstitial voids.

- Diffusive mass transport from bulk fluid to adsorptive surface (film diffusion).
- Diffusive mass transport from bulk fluid through pores.
- Adsorption from fluid to binding site.

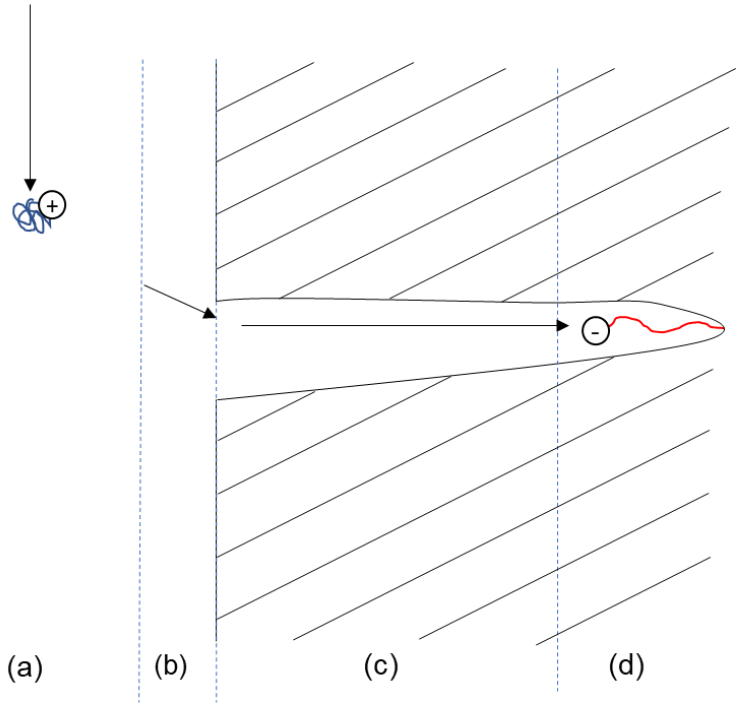


*Figure 2-7: Schematic of analyte movement through porous adsorptive media movement from bulk fluid to binding site: (a) advection through bulk fluid (void space); (b) diffusion from bulk flow to surface (film diffusion); (c) pore diffusion; (d) adsorption*

In most chromatography processes, adsorption is fast compared with other mass transfer rates and may thereby be neglected in time-dependent analyses. PBC is usually diffusion limited, because the rate of diffusion of analyte from the bulk fluid through to the solid, and diffusion through the pore structure, are much slower than mass transfer via advection in the bulk flow. In membrane and monolithic chromatography, the structures are designed to remove the diffusion limitation seen in PBC. These structures do not have blind pores as with beads; rather networks of small channels that the mobile phase flows through via advection. The Peclet number, Pe gives the advection mass transfer rate over the molecular diffusion rate (Equation 2-9).

$$Pe = \frac{vL}{\boldsymbol{D_m}} \tag{2-9}$$

Where $v$ is the interstitial velocity, $L$ is the column length, and $\boldsymbol{D_m}$ is the molecular diffusivity of the analyte. When Pe<1, diffusion effects are greater than advection effects.

Although not a type of mass transport, axial dispersion is an important mechanism to consider in the performance of chromatographic media. Axial dispersion refers to the amount of mixing in the longitudinal direction as a deviation from plug flow. Axial dispersion may be influenced by the diffusivity, turbulence, and stationary phase geometry. In most protein chromatography in porous media, axial dispersion is negligible compared with diffusion. To avoid confusion with the Peclet number which has been defined on a diffusion basis, the dispersion number of a column, $N_D$, is used to quantify the degree of dispersion compared with advection (Equation 2-10):

$$N_D = \frac{\boldsymbol{D_{ax}}}{uL} \tag{2-10}$$

Where $\boldsymbol{D_{ax}}$ is the dispersion coefficient. When $N_D < 0.01$ there is a small deviation from plug flow and dispersion may be neglected [53]. Dividing the Peclet number by the dispersion number gives the ratio of molecular diffusion to axial dispersion.

The accumulation of the mass transfer and dispersion effects affect the degree of band broadening in an elution profile, and it is important to be able to infer which mechanism is responsible for the band broadening. Residence time distribution and height equivalent of a theoretical plate (HETP) are ways of quantifying these effects.

#### *2.1.5.2.2 Residence Time Distribution*

In order to measure the effects of mass transfer and dispersion, the residence time distribution (RTD) of a column can be experimentally determined. A short pulse of a tracer molecule, generally inert, is loaded onto a column with the outlet concentration continuously detected. The shape of the effluent curve detected demonstrates the magnitude of band broadening and can be used to find the mean residence time ($\mu_1$) and variance ($\sigma$). A symmetrical, gaussian curve indicates near plug flow with minimal diffusion effects (Figure 2-8, blue), and a curve with a long tail indicates a pore diffusion limitation, because the tracer spends more time in the pores and takes longer to elute, or axial dispersion is influencing the flow (Figure 2-8, orange curve). Situations where multiple peaks are detected indicate channelling in a column, because mass transfer by advection causes the tracer to be entrained out of the channels with the bulk flow.

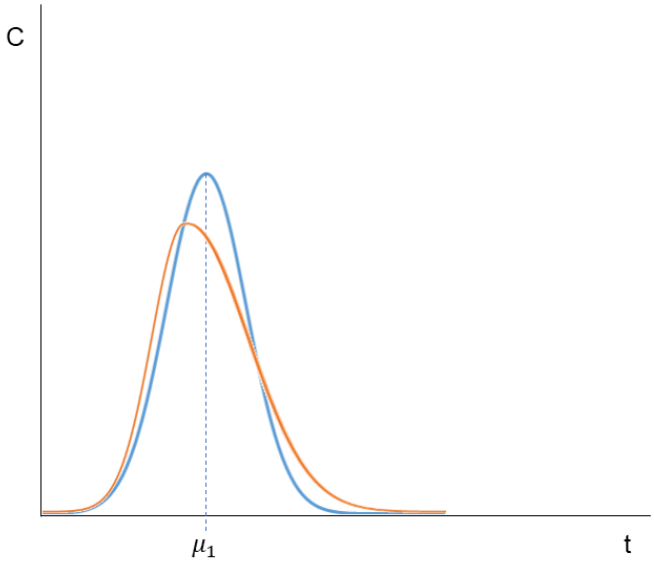


*Figure 2-8: Residence time distribution (RTD) curves for tracers with same mean elution time $\mu_1$. Blue curve is normal (Gaussian), orange is skewed to the right*

The mean residence time and variance can be determined numerically from the RTD curves, shown in Equations 2-11 to 2-13 below.

$$\mu_0 = \int_0^\infty C dt = \sum C_i \Delta t \tag{2-11}$$

$$\mu_1 = \frac{1}{\mu_0}\int_0^\infty C t dt = \frac{1}{\mu_0}\sum C_i t_i \Delta t \tag{2-12}$$

$$\sigma^2 = \frac{1}{\mu_0}\int_0^\infty C(t-\mu_1)^2 dt = \frac{\sum t_i^2 C_i}{\sum C_i} - \mu_1^2 \tag{2-13}$$

Using these parameters, the dispersion number can be calculated using Equations 2-14 and 2-15.

$$\sigma_\theta = \frac{\sigma^2}{\mu_1^2} \tag{2-14}$$

$$\sigma_\theta = \frac{2\boldsymbol{D_{ax}}}{uL} - 2\left(\frac{\boldsymbol{D_{ax}}}{uL}\right)^2\left(1 - e^{-\frac{uL}{\boldsymbol{D_{ax}}}}\right) \tag{2-15}$$

For a guessed initial value of $\frac{D_L}{uL}$, the equation above may be iterated through until $\sigma_\theta$ is satisfied.

#### 2.1.5.2.3 Inverse Size Exclusion Chromatography

Taking advantage of different size tracer molecules, RTD data can be used to determine porosity of stationary phases in inverse size exclusion chromatography. Inverse size exclusion chromatography (ISEC) is a good way of determining porosity without destroying the stationary phase matrix. Tracer molecules with different sizes are selected such that a large molecule is excluded from the matrix's pores, so its elution volume gives the interstitial volume. A small tracer molecule interacts with all the pores; therefore, its elution volume corresponds to the pore volume and interstitial volume. Typically, high molecular weight blue dextran is used as the large molecule, and acetone is used as the small molecule [54, 55].

From RTD curves, the mean residence time, $\mu_1$, is converted to mean elution volume, $V_e$, by dividing by the flowrate ($F_0$) (Equation 2-16):

$$V_e = \frac{\mu_1}{F_0} \tag{2-16}$$

From the mean elution volume, Equation 2-17 can be used to find the pore volume, $V_p$, and interstitial volume, $V_i$.

$$V_e = V_i + K_D V_p \tag{2-17}$$

These volumes are related by a distribution coefficient, $K_D$, which is the ratio of tracer concentration in the pores to the concentration in the interstitial space. For complete penetration of the pores, $K_D = 1$, and for complete exclusion $K_D = 0$ [56]. Blue dextran is assumed to be completely excluded from the pores, therefore $V_e = V_i$, and $K_D = 1$ for acetone, therefore $V_e = V_i + V_p$. This may be rearranged for $V_p$ by substituting in $V_i$ from the blue dextran data.

For a known column volume, $V_{column}$, this data is used to calculate porosities, sometimes referred to as pore fraction. Interstitial void fraction, $\varepsilon_i$, pore void fraction, $\varepsilon_p$, and total void fraction, $\varepsilon$, are calculated using Equations 2-18, 2-19 and 2-20.

$$\varepsilon_i = \frac{V_i}{V_{column}} \tag{2-18}$$

$$\varepsilon_p = \frac{\left(V_{e,acetone} - V_i\right)}{V_{column}} = \frac{V_p}{V_{column}} \tag{2-19}$$

$$\varepsilon = \frac{V_{e,acetone}}{V_{column}} = \frac{V_i + V_p}{V_{column}} \tag{2-20}$$

The diameter of the blue dextran tracer molecule is calculated from its molecular weight [57] (Equation 2-21):

$$d_m = 0.53 M_W^{0.5} \tag{2-21}$$

Where $M_w$ is the molecular weight and $d_m$ is the diameter of the molecule. This diameter gives the maximum size pore from which the molecule may be excluded.

#### 2.1.5.2.4 Plate Height

A commonly cited way to quantify the effects of advection and diffusion is to calculate the height equivalent to a theoretical plate (HETP) for an analyte on a chromatographic media, or the plate number, *N*. From either an RTD curve or elution peak in a chromatogram, HETP gives a measure of column efficiency. As band broadening is minimised, this increases column efficiency and decreases the HETP and increases the plate number. Ideal behaviour occurs when the plate numbers approaches infinity and HETP approaches zero. Using variance, mean residence time, and column length, HETP is calculated in metres from Equation 2-22:

$$HETP = \frac{\sigma^2 L}{\mu_1^2} \tag{2-22}$$

And plate number is calculated from Equation 2-23:

$$N = \frac{L}{H} \tag{2-23}$$

The plate height is often divided by the characteristic length of the column packing, $d_p$, to be presented as a dimensionless quantity, the reduced plate height, $h'$ (Equation 2-24):

$$h' = \frac{H}{d_p} \tag{2-24}$$

The Van Deemter curve [58] gives a method of quantifying the mass transfer effects on column efficiency, where the reduced plate height is plotted against the Peclet number. Interstitial velocity, $v$, used in the Peclet number is calculated using Equation 2-25:

$$v = \frac{u}{\varepsilon} \tag{2-25}$$

Where $u$ is the linear velocity, which is found from the flowrate, $F_0$, and cross-sectional area, $A$ (Equation 2-26).

$$u = \frac{F_0}{A} \tag{2-26}$$

For the Peclet number, the diffusivity of the analyte was required, which is calculated from the Hayduk-Laudie correlation for aqueous solutions (Equation 2-27) [59]:

$$\boldsymbol{D_{m,AB}} = \frac{13.16 \times 10^{-5}}{\mu_B^{1.14} V_A^{0.589}} \tag{2-27}$$

A generalised van Deemter curve is plotted in Figure 2-9 below. The hyperbolic curve (yellow) is a function of three parameters: hydrodynamic dispersion (blue), axial diffusion (orange) and mass transport (grey). These three parameters interact to yield an optimum Peclet number, where reduced plate height is minimised.

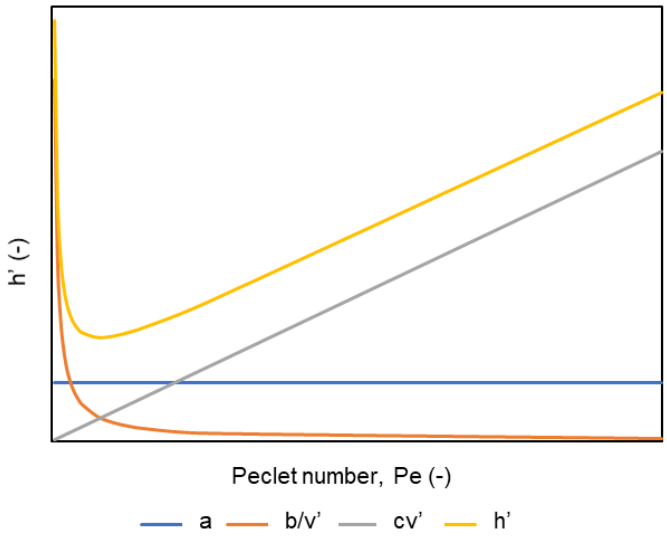


*Figure 2-9: Generalised van Deemter curve (h') with contributing effects of eddy dispersion (a), axial diffusion (b/v'), and mass transport (cv')*

The effects of each of these parameters is different depending on the Peclet number, which in turn is predominantly affected by the interstitial velocity. Hydrodynamic dispersion is constant for all Pe, because this is generally a function of the distribution of the stationary phase packing. Poor packing distribution yields channelling in a column, resulting in early elution and multiple peaks in an RTD or chromatogram. At low Pe, axial diffusion has the most pronounced effect on reduced plate height, because the low velocities or large diffusivity mean that analyte diffuses faster than the fluid front, causing band broadening. At large Pe,

the effects of mass transfer are the most prominent. At high velocities, diffusive mass transfer is much slower than advective mass transfer, meaning RTDs and chromatograms have a long tail, reducing the column efficiency. At this point, the rate of adsorption and desorption is also taken into account.

The van Deemter curve is given by Equation 2-28, where the constants correspond to those in Figure 2-9.

$$h' = \frac{b}{v'} + a + cv' \tag{2-28}$$

Where $v'$ is the reduced velocity, calculated using Equation 2-29.

$$v' = \frac{vd_p}{\boldsymbol{D_{m,AB}}} \tag{2-29}$$

Carta and Jungbauer used this analysis to determine the dominant dispersive factor for different types of chromatography [52] which is summarised in Table 2-4. Of interest was the difference in dominant dispersive factors between macromolecules in monoliths and in porous particles. In monoliths, hydrodynamic dispersion was dominant for macromolecules, while mass transfer was the dominant dispersive factor in porous particles. This is because for large molecules such as proteins, the diffusivities are small compared with smaller molecules, meaning diffusion times are longer when the molecule must diffuse into an internal pore structure. This is not observed in monoliths, where macromolecules do not need to diffuse passively through a porous structure; rather are carried through via advective transport. For future developments of adsorptive media, reduced plate height should be minimised, and remain outside the range where mass transfer is the dominant dispersive factor because this greatly reduces the column efficiency.

*Table 2-4: Dominant dispersive factors for different types of chromatography [52]*

| Type | Range of $v'$ | Dominant dispersive factor |
|---|---|---|
| Gas chromatography | 0.1-1 | Axial diffusion |
| Small molecules and analytical HPLC | 1-100 | Hydrodynamic dispersion |
| Macromolecules in monoliths | 1-10 | Hydrodynamic dispersion |
| Macromolecules in porous particles | 100-10000 | Mass transfer |

#### 2.1.5.2.5 Breakthrough Curves

Breakthrough curves are used to quantify the performance of adsorptive media. Breakthrough curves are generated the continuous application of adsorbate to the adsorptive media, with continuous monitoring of the effluent concentration. The ratio of effluent concentration to feed concentration $\left(\frac{C}{C_0}\right)$ is plotted against time or volume added to generate the curve, shown below (Figure 2-10).

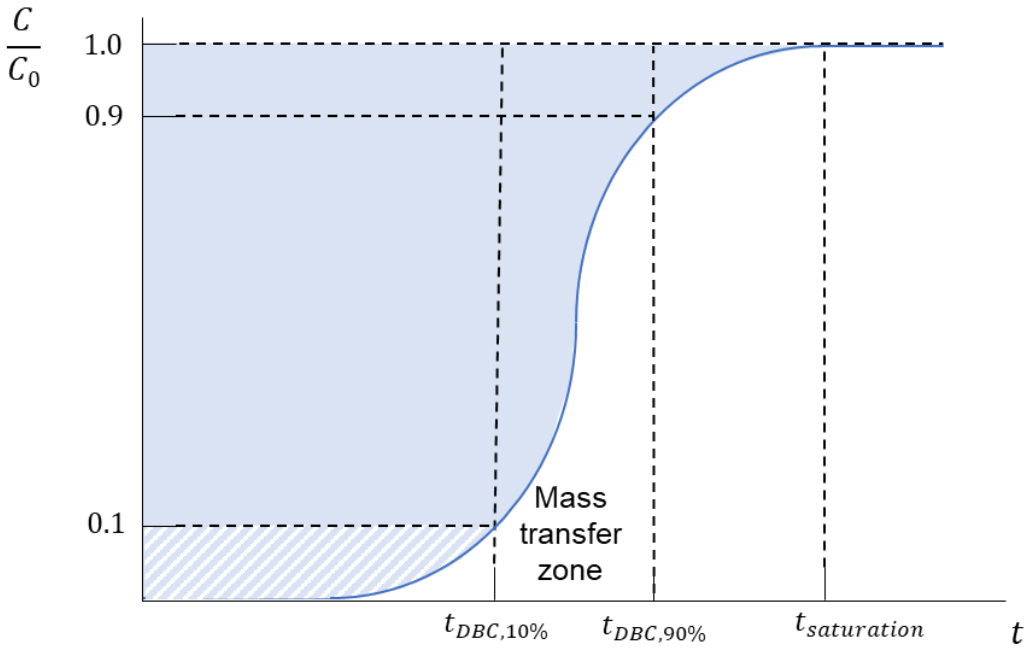


*Figure 2-10: Example breakthrough curve*

A number of important characteristics of adsorptive media can be quantified from the breakthrough curve. The total amount of analyte which can be adsorbed to the column, called the saturation binding capacity (SBC), is determined by integrating the area above the breakthrough curve (all blue areas in Figure 2-10). The trapezium rule may be used to numerically determine this integral, where the area is divided into strips, with strip width $t_{i+1} - t_i$, and strip average height $1 - \frac{\frac{C}{C_{0_i}} + \frac{C}{C_{0_{i+1}}}}{2}$, the product of these values gives the area, which is then summed to give the total area above the curve. This is shown in Equation 2-30, where in order to given SBC in unit mg/ml, the area is multiplied by the feed concentration $C_0$ in mg/ml, flowrate $F_0$ in ml/s, and column volume, $V_{column}$ in ml.

$$SBC = \frac{\sum\left(\left(1 - \frac{\frac{C}{C_{0_i}} + \frac{C}{C_{0_{i+1}}}}{2}\right)(t_{i+1} - t_i)\right) C_0 F_0}{V_{column}} \quad (2\text{-}30)$$

While the SBC gives the maximum capacity at a given linear velocity, the dynamic binding capacity (DBC) is often a more meaningful way of presenting the capacity of an adsorbent under dynamic conditions. The dynamic binding capacity at 10% breakthrough ($DBC_{10\%}$) is determined by integrating the area above the breakthrough curve between $\frac{C}{C_0}$= 0.1 and $t_{DBC_{10\%}}$ (blue striped area in Figure 2-10), and may be done numerically using the trapezium rule as before. At the point where $DBC_{10\%}$ is evaluated, the effluent concentration only contains 10% of the analyte compared with the feed concentration, so minimal product is lost. Operating beyond this point results in more product loss. The point where $DBC_{10\%}$ is evaluated is also referred to as the breakthrough point.

Between the breakthrough point and 90% breakthrough is known as the mass transfer zone. The gradient of the mass transfer zone gives the effectiveness of mass transfer: a steep curve has fast mass transfer, while a more gradual curve indicates poor mass transfer, where the analyte flows out of the adsorptive media faster via advection faster than it may be transferred to the solid surface, diffuse through pores, or adsorb. The effect of different mass transfer on breakthrough profile is shown in Figure 2-11 below. The yellow curve has the lowest mass transfer coefficient and demonstrates a situation whereby advective mass transport is faster than diffusion and adsorption, therefore initially most of the analyte flows out of the column immediately with the bulk fluid. The orange curve has the best mass transfer, where most of the analyte adsorbs immediately, rather than being entrained from the column. Blue and green curves demonstrate intermediate effects of mass transfer, where the mass transfer zone gradient becomes shallower and mass transfer from the mobile phase to the stationary phase is least efficient.

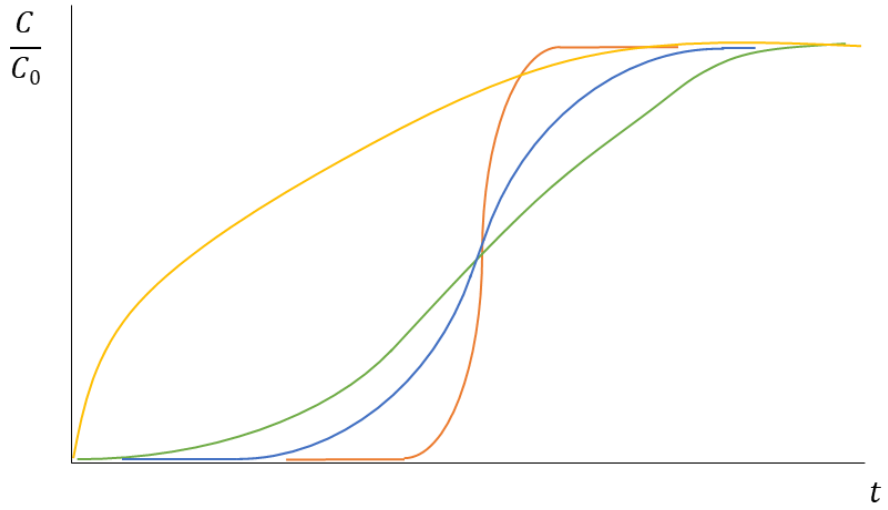


*Figure 2-11: Breakthrough curves dependent on mass transfer coefficient. Lowest coefficient on yellow curve, increasing coefficient with increasing gradient (yellow<green<blue<orange)*

Other observations that are made from breakthrough curves are the effects of axial dispersion. The effects of axial dispersion are shown in Figure 2-12, where low axial dispersion is present on the green curve, and is larger on the orange curve, and the largest on the blue curve. For ideal adsorption, dispersion should be minimised in order to reduce processing times.

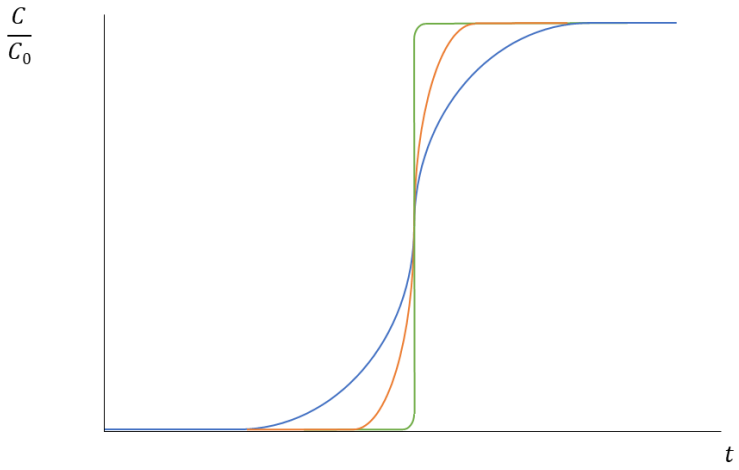


*Figure 2-12: Effect of axial dispersion on breakthrough curve*

## 2.2 Solids Removal

The ability of chromatographic media to combine primary protein capture and solids removal depends on the ability of the column to allow particulates such as cells and cell debris to pass unobstructed through the column. This is dependent on a number of mechanisms usually

used to design filtration units, however in this research, poor filtration behaviour is desired. The main mechanisms include:

- Straining.
- Sedimentation.
- Interception.
- Inertial impaction.
- Diffusion.
- Hydrodynamic interaction.
- Electrostatic interaction.

Straining occurs when the particulate matter is prevented from passing through the flow channels because the diameter of the solid particle is greater than the characteristic length of the interstitial void space. To prevent entrapment in this case, the column stationary phase structure must have an interstitial voidage with a characteristic length larger than that of the particle. This may be difficult to predict given cell diameter depends on growth age of the cell; therefore, selection of a column media and geometry must consider the maximum cell diameter.

Sedimentation refers to particulate capture via gravitational settling, whereby solid particles fall vertically and settle on the column. The likelihood of this occurring is dependent on the particle's terminal velocity and the velocity of the bulk flow. These are combined in the Gravity number, $N_G$ (Equation 2-31).

$$N_G = \frac{d_s^2(\rho_s - \rho_f)g}{18\mu_f u} \tag{2-31}$$

Where $d_s$ is the solid's diameter, $\rho_s$ is the cell density, $\rho_f$ is the fluid density, $g$ is acceleration from gravity, $\mu_f$ is the fluid viscosity and $u$ is the bulk fluid velocity. When $N_G$ is less than 1, the bulk velocity dominates the settling velocity, and sedimentation is less likely to occur [60]. Therefore, increasing bulk fluid velocity will reduce the effect of sedimentation which is desirable in solids removal.

Interception occurs when the cell radius is greater than the distance between the flow streamline and the filter's surface; the cell will contact and settle on the column surface provided no repulsive mechanisms are present. Thus, larger interstitial space and smaller particles are required for a successful solid's removal step. Interception efficiency is

dependent on the aspect ratio, $N_R$ (Equation 2-32), the van der Waals number which characterises attraction between the solid and the filter surface, $N_{vdW}$ (Equation 2-33), and the Peclet number. $d_p$ is the characteristic dimension of the stationary phase, $H$ is the Hamaker constant, $k$ is the Botlzmann constant, and $T$ is the absolute temperature.

$$N_R = \frac{d_s}{d_p} \tag{2-32}$$

$$N_{vdW} = \frac{H}{kT} \tag{2-33}$$

Inertial impaction is prominent when flow direction changes, but the particle's direction does not change because of its greater inertia. When this occurs close to the column surface, the particle can come into contact with and be entrapped in the column stationary phase. The Stokes number, $St$ (Equation 2-34), is used to quantify the magnitude of inertial impaction: an appropriate range of Stokes numbers for a filter is $1\text{x}10^{-9} - 2\text{x}10^{-3}$ [61]. The larger the Stokes number, the greater chance of inertial impaction occurring.

$$St = \frac{\rho_s d_s^2 u}{18\mu_f d_p} \tag{2-34}$$

As opposed to sedimentation, a large bulk flow velocity results in particle entrapment within the column. However, this can be counteracted by increasing the characteristic dimension of the stationary phase material, whether this be a particle diameter or monolith diameter.

Random diffusion, or Brownian motion of a suspended solid may cause it to come into contact with the column's surface. This is generally only significant when the particle diameter is less than 1 μm, and it is characterised by the Peclet number. As eukaryotic cells usually range between 10 μm – 100 μm in diameter [62], this effect can be neglected.

Hydrodynamic interaction is defined by the Reynolds number, $Re$ (Equation 2-35). In cases with multiple channels or interstitial spaces, a modified Reynolds number, $Re_l$ (Equation-2-36), is used.

$$Re = \frac{d_p u \rho_f}{\mu_f} \tag{2-35}$$

$$Re_l = \frac{v\rho_f}{(1-\varepsilon)S_v\mu_f} \tag{2-36}$$

Where $v$ is the interstitial velocity, and $S_v$ is the specific surface area per unit volume of the stationary phase. If the modified Reynolds number is less than 2, then the fluid follows a streamline throughout the column, but the particles "wander" between flow streamlines and can become entrapped on the stationary phase [61]. At higher values of the modified Reynolds number hydrodynamic interaction can be reduced. This is caused by applying a fluid greater velocity or using a stationary phase with a smaller surface area.

Electrostatic interaction refers to attraction caused between relative charges of the particle and the column surface. When the charges are opposite, the particle is attracted to the surface of the column. This presents a large issue when using a chromatography media for solids removal, because the presence of ion exchange ligands will likely result in the mechanism being prominent under certain conditions. Cell walls generally have a net negative charge, therefore would bind to an anion exchange column. The interaction between the particle and the surface is characterised by the attraction coefficient, $\alpha$, determined experimentally by Tari et al. [49].

Tufenkji and Elimelech [63] derived an empirical equation describing the collection efficiency of porous filtration media, $\eta_0$ (Equation 2-37), which was the sum of the capture efficiency from diffusion, $\eta_D$ (Equation 2-38), the capture efficiency from interception, $\eta_I$ (Equation 2-39), and the capture efficiency from sedimentation, $\eta_G$ (Equation 2-40). The capture efficiency of a porous collector is given in Equation 2-41

$$\eta_0 = \eta_D + \eta_I + \eta_G \tag{2-37}$$

$$\eta_D = \frac{2.4A_s^{\frac{1}{3}}N_{vdW}^{0.052}}{N_R^{0.081}Pe^{0.715}} \tag{2-38}$$

$$\eta_I = 0.55A_sN_R^{1.675}N_A^{0.125} \tag{2-39}$$

$$\eta_G = \frac{0.22N_G^{1.11}N_{vdW}^{0.053}}{N_R^{0.24}} \tag{2-40}$$

$$\eta_0 = \frac{2.4A_s^{\frac{1}{3}}N_{vdW}^{0.052}}{N_R^{0.081}Pe^{0.715}} + 0.55A_sN_R^{1.675}N_A^{0.125} + \frac{0.22N_G^{1.11}N_{vdW}^{0.053}}{N_R^{0.24}} \tag{2-41}$$

Where $Pe$ and $N_G$ were previously defined. $A_s$ is a porosity dependent parameter defined by Happel, and $N_A$ is the attraction number (Equation 2-42), which gives the ratio of van der Waals attraction forces to the inertial forces of the settling particle.

$$N_A = \frac{H}{3\pi\mu_f d_s^2 u} \tag{2-42}$$

For a solid suspension with a starting concentration $C_0$, the solids recovery, $C/C_0$, may be found using Equation 2-43. For a solid-tolerant chromatography matrix, $C/C_0 = 1$ indicates complete recovery of the solids in the column effluent, which is desirable for the operation of these columns as a process combining primary protein capture and solids removal.

$$\frac{C}{C_0} = exp\left(-\frac{(1-\varepsilon)L\eta_0\alpha}{d_p}\right) \tag{2-43}$$

When considering optimising the solids removal from a process that combines primary protein capture and solids removal in a single step, the main parameters affecting solids recovery are the sample velocity and interstitial diameter. Higher velocities reduce effects of sedimentation and hydrodynamic interaction, and large interstitial diameters reduce the effects of interception and inertial impaction. In comparison with good protein adsorption efficiency, these parameters have the opposite effect. Higher velocities and larger interstitial spaces increase the advective mass transfer of the analyte, which requires time to diffuse into porous structures. Combining primary protein capture and solids removal requires careful optimisation, whereby minimal target protein is lost, and as many of the solids are removed from the initial broth as possible.

## 2.3 Functionalisation

For stationary phases that require chemical modification in order to immobilise ligands, there are a wide range of functionalisation methods available. These may involve grafting polymers to the material or coupling a ligand to the appropriate groups. For both agarose and cellulose structures, hydroxyl groups provide a clear path for functionalisation, although in their base form they are very resistant to chemical modification, so an activation step is required before the ligand coupling step. The activation method, ligand coupling procedure and final chromatographic application are all important in selecting the appropriate functionalisation process.

### 2.3.1 Matrix Activation

Activation is the means to chemically modify an inert matrix to increase its affinity to the target ligand in order to obtain the product matrix that has a covalent bond with the ligand attached. Several activation options are available for agarose and cellulose that involve modifying one of the hydroxyl groups in each glucose ring of the polysaccharides. Harsh chemical activations include cyanogen bromide, 1,1'-carbonyl diimidazole (CDI), 1,1′-carbonyl-di-(1,2,4-triazole) (CDT), 1,1'-carbonyl-di-(1,2,3-benzotriazole) CDB, phosgene, epoxide activation, and many more [18]. The activation method is generally determined by the ligand to be immobilised to the matrix. For example, if the ligand contains an amine, hydroxyl, or sulfhydryl group such as 6-aminohexanoic acid and benzylamine ligand both contain amine groups are highly reactive with the imidazole intermediate formed by CDI activation of hydroxyl groups. Epoxy activation is suitable for immobilising ligands with hydroxyl or sulfhydryl groups. Activation methods for hydroxyl groups on agarose and cellulose are considered in this section.

Cyanogen bromide (CNBr) was among the first hydroxyl activation methods to be developed. Under alkaline conditions (approximately pH 11.0), the hydroxyl containing matrix is reacted with CNBr, forming a reactive cyanate ester (Figure 2-13) [64] [65] [66].

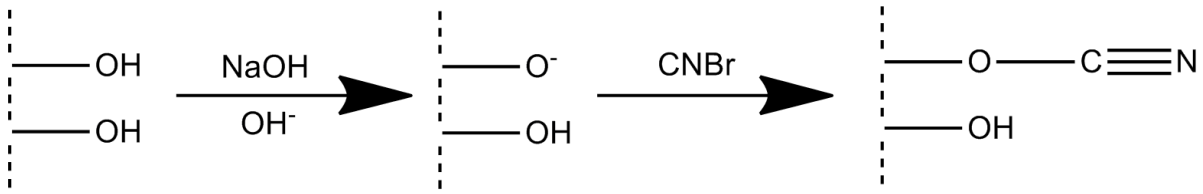


*Figure 2-13: CNBr activation reaction scheme yielding active cyanate ester active group*

The cyanate ester is highly reactive to amine-containing ligands, and each molecule of CNBr ultimately uses two hydroxyl groups on the stationary phase to create the amine bond which immobilises the amine-containing ligand (Figure 2-14 (b)). However under some reaction conditions once the activated matrix was exposed to the ligand, the triple cyanate ester bond may split into a single amine bond, immobilising the ligand to the stationary phase, and a double bonded amide (Figure 2-14 (a)). The latter is undesirable, because although the ligand is immobilised to the surface, an extra cation exchange group is introduced to the surface which can be a source of non-specific binding.

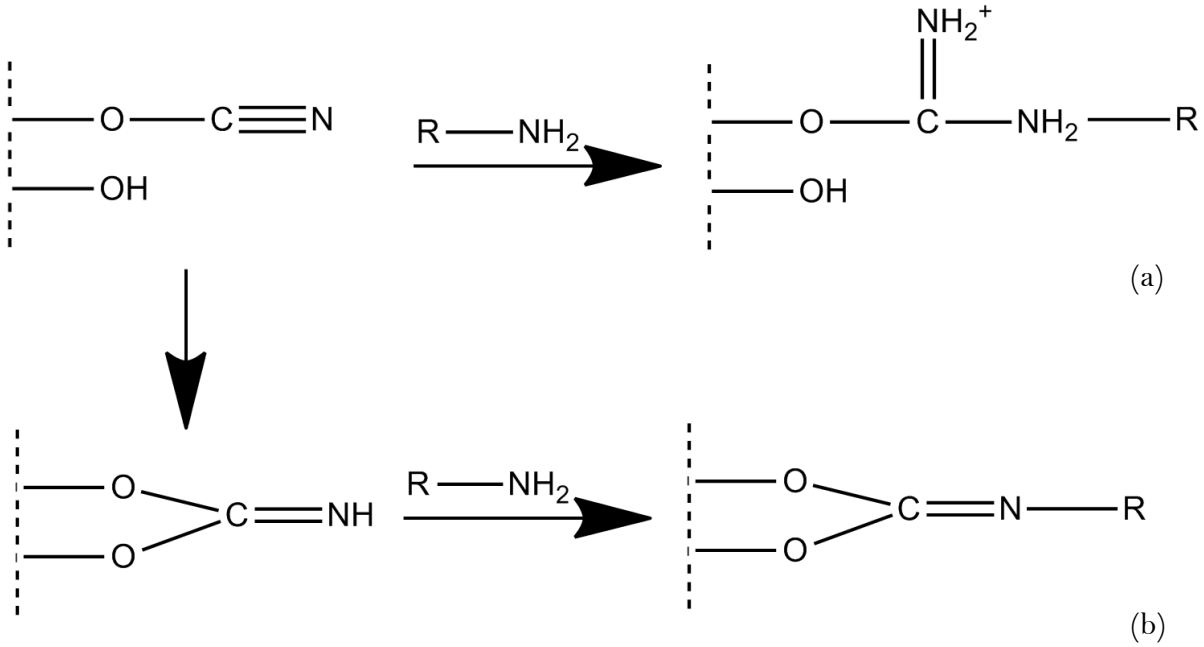


*Figure 2-14: Reactions of cyanide ester with amine containing ligand forming (a) immobilised ligand with cation exchange group and (b) immobilised ligand*

1, 1'-Carbonyl diimidazole (CDI) was discovered as an alternative hydroxyl activation agent to CNBr because of its higher activation yield compared with CNBr and doesn't result in extra cation exchange groups forming as a result of activation [67]. Because of this, CDI is widely used an a hydroxyl activator for a large range of ion exchange and affinity ligands [68]. The reaction scheme below shows the formation of the reactive imidazole intermediate formed on a hydroxyl containing matrix (Figure 2-15).

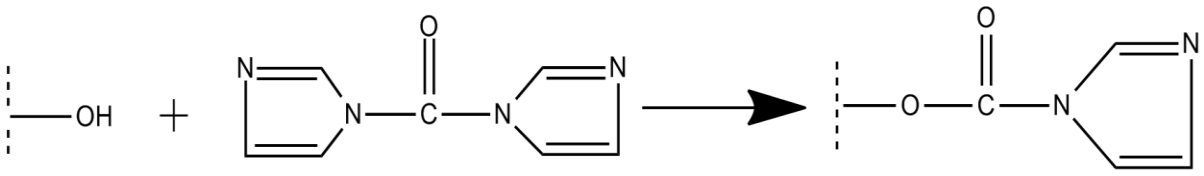


*Figure 2-15: CDI activation of hydroxyl containing matrix resulting in reactive imidazole intermediate on matrix surface*

The reactive imidazole carbamate intermediate is susceptible to reaction with nucleophilic amino groups in basic conditions [18]. This makes it an attractive option for immobilisation of ligands that contain primary amines, amino acids, proteins, and other complex amine-containing molecules. The covalent carbamate linkage has good chemical stability in mildly basic and acidic conditions. This CDI activation provides an excellent pathway to create biospecific or affinity chromatography supports. CDI activated matrices do not have any charged groups following ligand coupling, making it a good activation method for affinity

chromatography where charged groups are unnecessary. However, the reactive imidazole carbamate intermediate hydrolyses very quickly under aqueous conditions. Hydroxyl groups in aqueous solutions substitute with the reactive intermediate, therefore activation is generally conducted in an acetone solution and then washed quickly in a non-aqueous solution to remove unreacted CDI to prevent this. The hydrolysis reaction rate increases with increasing pH; Bethell et al. found that it took 10 hours for a matrix to completely hydrolyse at pH 10 and 1.5 hours to completely hydrolyse at pH 11 [69].

### 2.3.2 Ligand Coupling

Materials activated with CDI are highly reactive to amine-containing ligands. The ligand 6-aminohexanoic acid is a suitable ligand to consider in creating an ion exchange matrix via immobilisation to a CDI activated matrix. 6-aminohexanoic acid acts as a nucleophile once deprotonated at a high pH, therefore will be immobilised to the activated matrix via a carbamate linkage from the reactive intermediate. The other end of the ligand is a carboxylic acid group, otherwise known as a weak cation exchange (CM) group. The scheme below demonstrates the immobilisation reaction.

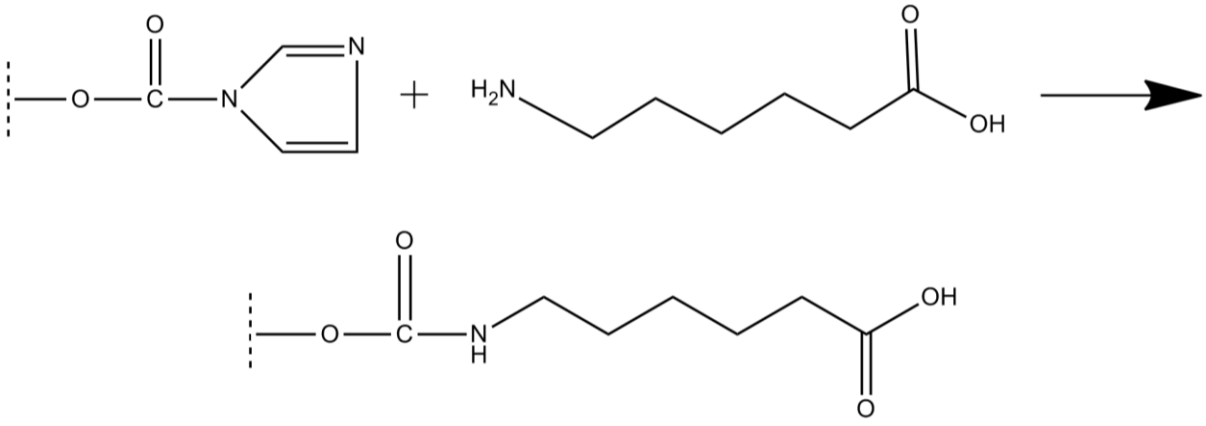


*Figure 2-16: Immobilisation of 6-aminohexanoic acid to CDI activated matrix*

Immobilisation of 6-aminohexanonoic acid following CDI activation is conducted under aqueous conditions. An alkaline solution is required to deprotonate the amine group. However, the high pH means the matrix is more susceptible to hydrolysis. With these competing reactions, a pH of 10 is recommended for the ligand coupling solution [68, 69].

Another simple ligand is benzylamine, which is an aromatic ring with an amine group. Benzylamine is soluble in acetone, hence the immobilisation reaction does not need to be done

under aqueous conditions, eliminating the risk of competing hydrolysis. The aromatic ring is strongly hydrophobic, therefore immobilisation to agarose or cellulose creates a hydrophobic interaction chromatography matrix. Benzylamine also has reported bio-affinity with glycogen phosphorylase and heparin [68], hence creating an affinity matrix.

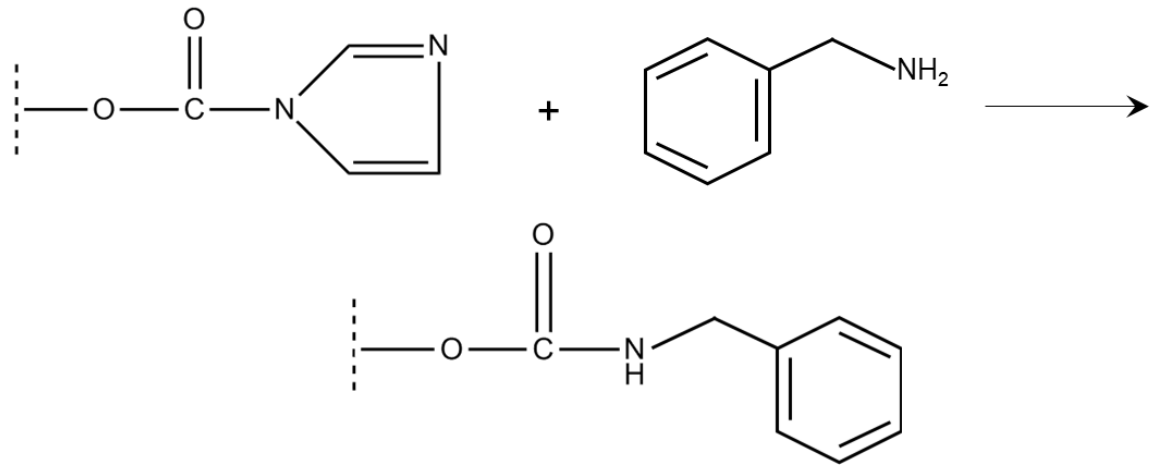


*Figure 2-17: Immobilisation of benzylamine ligand to CDI activated matrix*

### 2.3.3 Other Functionalisation Methods

Other functionalisation methods are reported for common chromatography ligands. The most predominant methods are for the substitution of hydroxyl groups for DEAE and Q ligands to create anion exchange matrices. DEAE substitution is achieved by equilibrating the stationary phase material in a solution of the diethylaminoethyl ligand 2-chloro-N,N-diethylethylamine hydrochloride (DEAE/Cl) and concentrated hydroxide. Upon increasing the temperature, the hydroxyl groups are substituted with the DEAE ligand [70, 71].

Lastly, the direct immobilisation Quaternary ammonium immobilisation to hydroxyl-containing stationary phases may be achieved by using a molecule containing an epoxide group and a Q group such as glycidyl trimethylammonium chloride (GMAC). Sodium borohydride is added to a solution of the stationary phase, 70% GMAC, and sodium hydroxide to reduce the hydroxide groups on the matrix [18]. The epoxide ring opens and forms an ester bond with the matrix, leaving the Q group available for ion exchange.

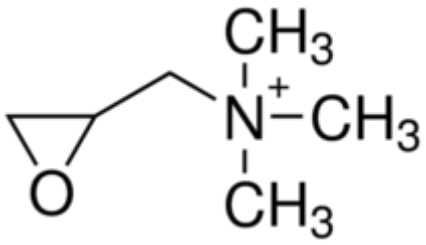


*Figure 2-18: Chemical structure of glycidyl trimethylammonium [72]*

## 2.4 3D-Printing

3D-printing, also known as additive manufacturing (AM), has been touted as one of the most disruptive technologies of the 21st Century. AM is the process whereby a 3D model is produced layer-by-layer from a computer-designed template. The first patent for AM was filed in 1986, a stereolithography patent by Hull [73], however it wasn't until the mid-2000s that the potential for 3D-printing to become part of mainstream manufacturing was realised. The nature of 3D printing means that identical objects can be manufactured every time; this characteristic may be exploited in industries where difficulties in geometric reproducibility is a problem. Tissue engineering and biomedical engineering [74-78], aviation and aerospace engineering [79], electronic engineering and microfluidics [80], and manufacturing are only a few of the many, many disciplines where 3D-printing has led to major developments.

The feed material for 3D-printers can either be solid or liquid; the 3D-printing method depends on the material and resolution of the model. Solid materials can be in filament or powder form. Filaments are thermoplastics or waxes used in a fused deposition modelling (FDM) whereby the filament is heated to its melting point, extruded through a nozzle and deposited layer-by-layer to create the 3D-model. FDM prints generally have a printing resolution between 50 μm -200 μm [81]. Powdered metals, ceramics and polymers are used in selective laser sintering (SLS) and selective laser melting (SLM). The powder bed is exposed to heat via a laser, selectively heating the layers causing them to either heat up enough that the powder molecules adhere to each other (SLS), or melt and fuse together (SLM). Reported resolution ranges between 80 μm and 250 μm [81].

Liquid-feed processes start with a photo-curable resin, or mixture of monomers and photo-initiators in solution, which are exposed to a light source, selectively curing the resin layer-by-layer in accordance with the computer design. This process is called

stereolithography. These processes can produce finely controlled geometry structures with resolutions down to 1 μm – 10 μm [82].

### 2.4.1 3D-Printing in Chromatography

Since 2014, chromatography has been a developing application for 3D-printing technologies after being introduced by Fee et al. [9]. The ability of producing controlled geometry structures means that problems with experimental reproducibility associated with random PBC can be avoided. Geometries with optimum mass transfer properties may be produced, remaining identical across columns. Furthermore the geometries are not limited to packed bed resins in a cylindrical column but could be more serpentine, tubular columns with controlled monolithic stationary phases, or a packed bed of octahedral particles [9, 83-86]. They key challenges in developing 3D-chromatography matrices include the selection of materials that are suitable for both 3D-printing and chromatography and selecting a suitable geometry for the stationary phase – whether this be spherical particles, monoliths, or something else.

#### 2.4.1.1 3D–Printed Materials and Methods for Chromatography

The material must be suitable for chromatography (see parameters outlined in Section 2.1.3) and must be able to be made into a controlled geometry structure via one of the methods in the previous section. Parameters that make a material suitable for chromatography include resistance to chemical attack, mechanical stability, high porosity, low non-specific binding, and the ability to be functionalised for a desired mode of chromatography. As was outlined in Section 2.1.3, hydrogels such as agarose and cellulose a commonly used as stationary phase materials. However, at the beginning of this project there was limited evidence of these materials being used in chromatography.

Many polymers commonly used in solid-based 3D printing are commonly thermoplastics because they have a low melting temperature, and once cast in shape do not deform and have low reactivity. Common plastics used in fused deposition modelling include acrylonitrile butadiene styrene (ABS), poly-lactic acid (PLA), polystyrene (PS) and polypropylene (PP) [81]. Because these polymers are generally unreactive, vigorous functionalisation techniques may be implemented at extreme conditions. For example heterogeneous sulfonation of a styrene group (in ABS and PP) is conducted with high sulfuric acid concentration and high temperature [87] which may prove difficult experimentally. These polymers are inherently non-porous, therefore addition of a porogen is required to increase the specific surface area

required for high adsorption. Furthermore, these polymers do not have a proven track record as chromatographic stationary phases, thus are unsuitable for this application.

Materials used in stereolithography may be easier to functionalise experimentally, as common materials are either epoxy or acrylate resins that are cured when exposed to light in the presence of a photoinitiator. These resins contain functional groups that have a simple reaction scheme to produce functional groups for ion exchange or attachment of ligands. Simon took advantage of this, creating an anion exchange absorber using copolymerisation of a bifunctional monomer containing a positively charged quaternary amine with an acrylate group, and a biocompatible crosslinker polyethylene glycol diacrylate (PEGDA) [88].

3D printing of hydrogels is an area where there is limited research available: these are generally used in tissue engineering to build scaffolds for cell growth [78, 89-92] which require different mechanical properties to those required for packed beds. The methods discussed in literature are either stereolithography with infrared lasers or fused deposition modelling, as these utilise a controlled change in temperature to gel the solution which then may be regenerated in water to form a hydrogel. Recent success has been seen in creating controlled geometry structures from cellulose [21], where a LASER was used to induce thermal gelation in a cellulose solution. Furthermore, products such as CELLINK Bio Printers show promise and development in this field. However these developments were not available when this project was in development [93].

#### 2.4.1.2 Stationary Phase Geometries

Employing 3D-printing techniques to create chromatography stationary phases opens a wide potential of geometric structures and shapes that could be used to obtain superior performance parameters and highly efficient protein capture. In this work, the chromatographic matrix must also allow solid passage, so this is taken into account in determining an appropriate column geometry. It pays to bear in mind that the application in this work is to create a column for simultaneous protein adsorption and solids removal. To narrow the scope of geometries considered for stationary phase materials, a number of criteria were applied:

- High surface area to volume ratio for adsorption.
- Good mass transfer characteristics.
- Large void space for solid passage through column.

- Feature resolution appropriate for printer.

For protein binding, high surface area to volume ratios ($S_v$) are required, as this provides more adsorption sides for proteins for a given volume of material. Spherical beads have a low $S_v$ compared with Platonic solids; a spherical unit has a $S_v$ of 4.8, while an octahedron has $S_v = 5.7$ and a tetrahedron has $S_v = 7.2$. 3D-printing would enable these shapes to be made as a packing material rather than relying on spheres. Dolamore showed that an ordered octahedral packing resulted in reduced HETP values compared with spheres [83]. However, in this application, packed beds of any bead shape are not suitable because of small void characteristic dimensions that would likely lead to blockages upon application of cells. Furthermore, bead diameters begin at 5 μm, and can be as large as 300 μm for some applications. The lower end of the scale is currently unprintable using today's available 3D-printing technologies.

Monolithic structures are considered as a suitable geometry for solid tolerant chromatography, given the channel diameter is large enough such that blockages do not occur; in other words the channel diameter is greater than the cell diameter. Ordered straight monoliths and herringbone monoliths are simple to design in a computer aided design (CAD) model, however the $S_v$ of columns with monoliths at an appropriate order of magnitude for solid passage is much smaller than with packed beads, reducing analyte capture efficiency. $S_v$ would be improved in these monolithic structures by employing a porous material as the base matrix, increasing the $S_v$ because of the porosity.

Building on the idea of using ordered monolithic structures as 3D-printable geometries is the use of triply periodic minimum surfaces (TPMS). TPMS are surfaces which produce identical interconnecting flow paths in three directions (x, y and z) with a mean curvature of zero, resulting in a minimised surface [94, 95]. Each class of TPMS structure is defined by an equation (Table 2-5), which can be manipulated to produce flow path diameters, wall diameters, and voidages of desired sizes. TPMS structures are becoming more prominent in chemical engineering with the growth of 3D printing technology moving to higher resolution. Heat exchangers, reverse osmosis membranes, ultrafiltration spacers and cell scaffolding are all areas where TPMS structures have enhanced the productivity of processes by providing good heat and mass transfer with a controllable pressure drop [96, 97]. These structures are applicable to solid tolerant chromatography as the channels allow cell passage, and if the walls are made of a porous material then the surface area can be high enough to allow protein adsorption. In-silico analysis of TPMS structures showed that HETP was

reduced compared with spherical particles because of the uniformity of flow channels [85], showing a clear benefit of employing these structures in chromatographic separations.

The overview of TPMS structures focusses on three classes: Schoen gyroid, Schwarz diamond and Schwarz primitive (Table 2-5). The equation used to produce one unit cell is shown, with the unit cell and a 2x2 unit cell shown to demonstrate how a larger repeating lattice of TPMS units may be produced. The unit cells shown in Table 2-5 may be produced in repeating structures and cut to a desired geometry using CAD software to fit into existing chromatographic hardware (ie column casings). For the development of TPMS structures as stationary phase geometries for chromatography, the following definitions are used herein: column diameter, referring to the overall diameter of the stationary phase structure; channel diameter, referring to the diameter of a single channel in a TPMS unit cell; and wall thickness, referring to the solid phase diameter/thickness of a single unit cell. These definitions are represented in the diagram below (Figure 2-19).

*Table 2-5: TPMS structure overview*

| Structure | Schwarz primitive | Schwarz diamond | Schoen gyroid |
|---|---|---|---|
| **Formula [94]** | $\cos(x) + \cos(y) + \cos(z) > 0$ | $\sin(x)\sin(y)\sin(z) + \sin(x)\cos(y)\cos(z) + \cos(x)\sin(y)\sin(z) + \cos(x)\cos(y)\sin(z) > 0$ | $\cos(x)\sin(y) + \cos(y)\sin(z) + \cos(z)\sin(x) > 0$ |
| **Specific surface area for 50% voids ($mm^{-1}$) [95]** | 2.34 | 3.84 | 3.10 |
| **Unit cell*** | 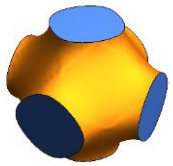 | 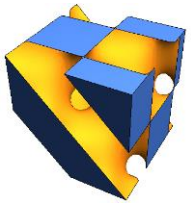 | 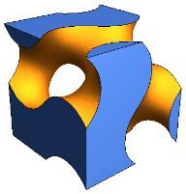 |
| **2x2x2 Unit cell*** | 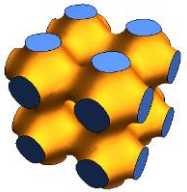 | 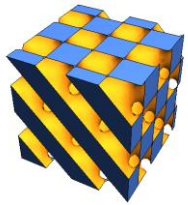 | 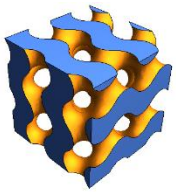 |

*Shapes generated in Wolfram Mathematica, solved where $-\pi < x,y,z < \pi$

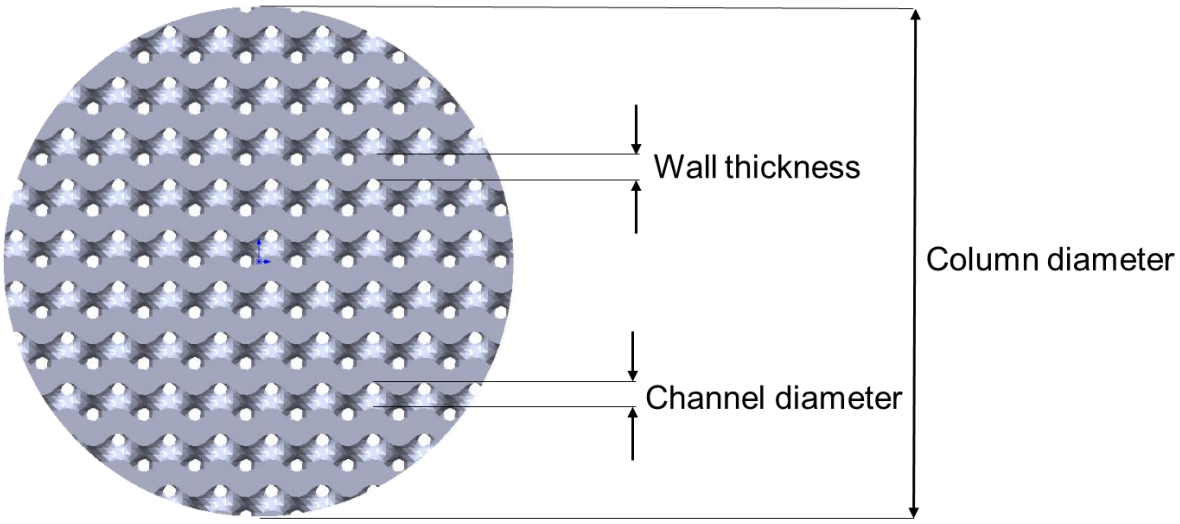


*Figure 2-19: Definitions of column diameter, wall thickness, and channel diameter for 0.5 voidage gyroid plate*

Based on data from Jung [95], the specific surface area of the two TPMS structures at 50% voidage was calculated for each channel diameter made in this research, shown in

Table 2-6. Despite the unit cells having the same voidage, specific surface area increased with decreasing channel diameter, meaning that in the context of protein chromatography, smaller channel diameter structures would be more desirable for protein capture given the ligand density increased proportionally with this increase in surface area. For the same channel diameter, Schwarz diamond had a higher specific surface area than the Schoen gyroid. This shows that the Schwarz diamond would be more effective at protein capture because of the higher specific surface area. It is important to note that these values give the macro surface area; that is, the surface area of the channel structures only. This does not take into account the surface area from the microporous structure of the hydrogels of the material. For the same type of hydrogel with the same percentage polysaccharide, crosslinker type, and ligand functionality, the porosity should be constant.

*Table 2-6: Specific surface areas of 50% voidage TPMS structures for different channel diameters*

| **Channel Diameter** | | μm | 300 | 400 | 500 |
|---|---|---|---|---|---|
| $S_v$ | Schwarz diamond | $mm^{-1}$ | 6.52 | 4.89 | 3.91 |
| | Schoen gyroid | $mm^{-1}$ | 5.15 | 3.86 | 3.09 |

The theoretical number of vertical channels for a TPMS structure can be estimated from the ratio of flow cross-sectional area to single channel cross-sectional area. The area available for flow in a 50% void TPMS structure is half the cross-sectional area of the circular diameter column. For a given flowrate, $F_0$, the velocity per channel, $u_{channel}$, can be calculated assuming the system is at steady state and the fluid is incompressible. This is summarised in Equations 2-44 to 2-47.

$$A_{flow} = \frac{\pi}{8} d_{column}^2 \tag{2-44}$$

The area of one channel (assuming circular) is given by

$$A_{channel} = \frac{\pi}{4} d_{channel}^2 \tag{2-45}$$

Therefore the number of channels may be simplified to

$$N_{channel} = \frac{d_{column}^2}{2 d_{channel}^2} \tag{2-46}$$

From this, the velocity in a single channel may be calculated from

$$u_{channel} = \frac{\left(\frac{F_0}{N_{channel}}\right)}{A_{channel}} \tag{2-47}$$

## 2.5 Direction of Current Work

In this chapter the topic of chromatography was discussed with respect to the main methods of chromatography practised in industry, highlighting PBC as the "state of the art", despite it being identified as a cause of an economic and through-put bottleneck in downstream processing. It was concluded that in order to reduce the bottleneck in downstream processing, an alternative to PBC which combines solids removal and primary protein capture is required. 3D-printing methods may be employed to create a stationary phase matrix suitable for this application, hereafter referred to as "solid-tolerant chromatography".

For a column to be suitable for solid-tolerant chromatography, there is a trade-off in stationary phase design, as efficient protein adsorption requires a high surface area with small flow channels to avoid protein loss via advection, while solid passage requires large diameter flow channels to prevent solid capture in the column. Therefore, in this work, columns are made from porous hydrogels (cellulose and agarose) in TPMS (gyroid and Schwarz diamond).

The hydrogels' porous networks provide high surface area for protein adsorption, and TPMS channels are designed large enough to permit solid passage.

3D-printing methods can be used to create the TPMS structure, however at time of process development 3D-printing technologies did not include the ability to print hydrogels to the resolution required for this work. Instead, a negative template of the TPMS structures could be printed out of a soluble material, and the hydrogel solution could be cast into this mould to create the controlled-geometry TPMS hydrogel column. This process maintains the principle of creating a controlled geometry TPMS hydrogel column using 3D-printing methods, although the column itself is not directly 3D-printed.

On top of their high porosity, cellulose and agarose have documented functionalisation for several modes of chromatography. Following the manufacture of columns using the templating method, columns are functionalised with a ligand for chromatography. CDI was shown to be a widely used activating agent for hydroxyl-containing polysaccharides and is suitable to be used in this research. Ligands 6-aminohexanoic acid and benzylamine are amine containing compounds, easily immobilised to the CDI-activated polysaccharide backbone, and result in chromatography matrices suitable for in cation exchange and hydrophobic chromatography respectively. The immobilisation of DEAE ligands to hydroxyl containing stationary phases is also well understood. These three modes of chromatography are explored; however, the focus is on the cation exchange columns.

Methods to characterise chromatographic performance were presented in this chapter, and include ion exchange capacity, static binding capacity, protein breakthrough and dynamic binding capacity, and height equivalent to a theoretical plate. These analyses are employed to determine the effectiveness of these columns as adsorbents. Theoretical cell recovery can be compared with experimental recovery, and the effect of the presence on solids in a feedstock on protein adsorption under dynamic conditions. Microscope imaging and RTD studies are used to analyse the channel and pore structure of the columns, providing insight into protein adsorption efficiency, cell recovery percentage, and the effectiveness of the functionalisation procedure. All in all, this work aims to show the manufacture, development, and characterisation of solid-tolerant chromatography columns made using 3D-printing techniques.

# Chapter 3. General Materials and Methods

This chapter serves to outline the processes followed in the design, manufacture, characterisation and testing of the TPMS columns prepared in this research. The chromatography columns were produced by designing a negative template of the column in Solidworks, printing the template on a 3D printer, then filling the template with either cellulose or agarose which was then gelled, forming a solid gel column. To remove the 3D-printed template, the columns were immersed in acetone which dissolved the print build material. The columns were then functionalised for either cation exchange, anion exchange or hydrophobic interaction chromatography and tested. The chemicals and equipment used in each of the experiments are presented below (Table 3-1 and Table 3-2), as many of these appear across multiple experimental steps. The chronology of the methods presented in this chapter will follow the chronology of results presented in the subsequent chapters of this work as accurately as possible.

*Table 3-1: Chemicals used in the experimental methods followed in this thesis*

| Chemical | Grade | Source |
|---|---|---|
| 1,1'-carbonyldiimidazole | Reagent | Sigma Aldrich |
| 2-chloro-N,N-diethylethylamine hydrochloride | Analytical | Sigma Aldrich |
| 6-aminohexanoic acid | Analytical | Sigma Aldrich |
| Acetic acid | Glacial | BDH Lab Supplies |
| Acetone | Technical | Thermo Fisher Scientific |
| Agarose | Molecular biology | Bio-Rad |
| Benzylamine | Analytical | Sigma Aldrich |
| Blue dextran | Analytical | Sigma Aldrich |
| Bovine serum albumin | Fraction V, IgG Free | Invitrogen Corporation |
| Cellulose | Highly purified fibres | Sigma Aldrich |
| Coomassie Brilliant Blue stain | Analytical | Thermo Fisher Scientific |
| Cytochrome c (bovine heart) | ≥95% | Sigma Aldrich |
| Deionised water | 18 MΩ cm resistivity | MilliQ |
| Disodium hydrogen orthophosphate | Analytical | Thermo Fisher Scientific |
| Dithiothreitol (DTT), reducing agent | 500 mM, 10X concentrated | Thermo Fisher Scientific |
| Epichlorohydrin | Analytical | Sigma Aldrich |

| | | |
|---|---|---|
| Ethanol | Analytical | Thermo Fisher Scientific |
| Hydrochloric acid | Analytical | Bio Lab |
| Isopropanol | Analytical | BDH Lab Supplies |
| Lithium dodecyl sulfate (LDS) buffer | 4X concentrated | Thermo Fisher Scientific |
| Lysozyme (egg white) | 95% | Sigma Aldrich |
| Methanol | Analytical | BDH Lab Supplies |
| Novex Sharp Pre-stained Protein Standard | Analytical | Thermo Fisher Scientific |
| Sodium bicarbonate | Analytical | Thermo Fisher Scientific |
| *Saccharomyces cervisiae* | Food | Local market |
| Sodium dodecyl sulfate (SDS) buffer | 20X concentrated | Thermo Fisher Scientific |
| Sodium chloride | Analytical | Arcos Organics |
| Sodium dihydrogen orthophosphate | Analytical | Thermo Fisher Scientific |
| Sodium hydroxide | Analytical | Thermo Fisher Scientific |
| Urea | Analytical | Thermo Fisher Scientific |
| VSO | Analytical | Regal Castings Ltd. |
| α-lactalbumin (bovine milk) | ≥85% | Sigma Aldrich |
| β-mercaptoethanol | Analytical | Thermo Fisher Scientifc |

*Table 3-2: Equipment used in experimental methods in this research*

| Equipment | Supplier |
|---|---|
| 1HAE-25-M104X Vacuum Pump | Gast |
| ÄKTA Start Chromatography Hardware | GE Healthcare |
| ÄKTA10 Explorer Chromatography Hardware | GE Healthcare |
| Eppendorf Centrifuge 5810R | Global Science |
| Gyrozen Micro Centrifuge 1730R | Bio-Strategy |
| ImageQuant LAS 500 Chemiluminescence CCD Camera | GE Healthcare |
| Ismatec Peristaltic Pump IPC | Cole Parmer |
| Kudos Ultrasonic Cleaner | Alphatech Systems Ltd. |
| Labconco Freezone 2.5 Freeze Dryer | Total Lab Systems Ltd. |
| LabServ Overlay 27 Oven | Contherm Scientific Ltd. |
| NanoDrop™ 2000c | Thermo Scientific |
| Nikon SMZ-1B Optical Microscope with ToupCam | ProSci Tech |
| pH-meter CP105 | Elmetron |

| | |
|---|---|
| Samsung Timesaver 1000 W Microwave | Local Electronics Store |
| JSN 7000F field emission high resolution scanning electron microscope | JEOL |
| Silverson L4RT Stirrer | Advanced Packaging Systems Ltd. |
| Solidscape 3Z Pro 3D Printer | Regal Castings Ltd. |
| Spinning Wheel | University of Canterbury |
| Ultrospec 2100 Pro UV/Vis Spectrophotometer | Amersham Biosciences |
| Up! Mini 3D Printer | PP3DP |
| Yellow line, Yellow Mag HS 7 Hot Plate/Magnetic Stirrer | Total Lab Systems Ltd. |

## 3.1 TPMS Template Design

The progression of TPMS column design is shown in Figure 3-1 using a gyroid as an example. Equations used to form the TPMS structures were given in Table 2-5, from which a 3D unit cell of TPMS gyroid packing was produced in Wolfram Mathematica, saved as a. stl file and imported to Solidworks (a). The unit cell was scaled appropriately to create the 300 µm, 400 µm, or 500 µm channel size with 50% voidage, and copied in the x and y directions to make a flat, square plate of gyroid cells (b). The flat plate was then cut to a 10 mm diameter circle (c) and each circular layer duplicated and stacked vertically to create the three-dimensional model of the column (50 mm long, 10 mm diameter) (d). The .stl file was then uploaded to the Solidscape 3Z Works program, where the file was converted to a .3zp file suitable for the Solidscape Pro 3D printer. A slice layer thickness of 0.0508 mm was selected as it was determined to be the best trade off to minimise file size and maximise resolution, this was used for all columns. For example, a unit cells for 500 µm, 400 µm, and 300 µm channel gyroids would have 17.2, 13.8 and 10.3 layers respectively meaning adequate resolution going from the .stl file to the printed model could be achieved. The Solidscape 3D printing material was a proprietary wax (Midas [98]), and support material was another proprietary wax (Melt [99]) which dissolved in VSO.

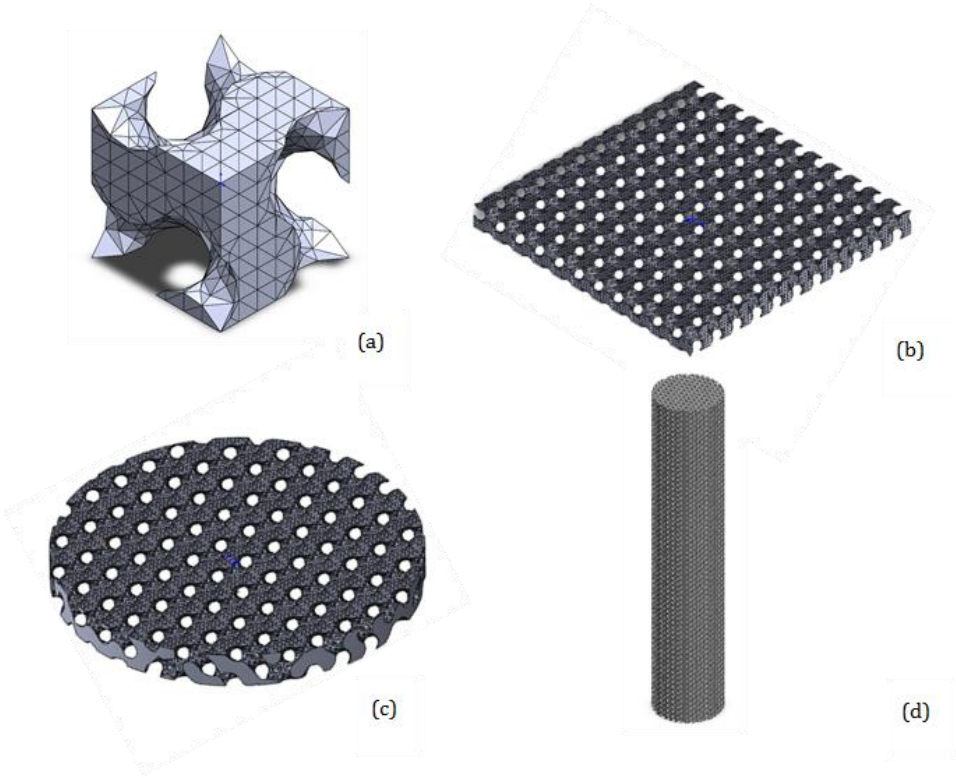


*Figure 3-1: TPMS column design progression in Solidworks: (a) unit cell imported from Wolfram Mathematica; (b) unit cell patterned in x and y dimensions; (c) linear patterned flat plate cut to 10 mm diameter; (d) plate patterned vertically to make 50 mm long column*

## 3.2 Hydrogel Solution Preparation

### *3.2.1 Agarose*

6% w/w agarose solutions were prepared by dissolving powdered agarose in a hot water solution. The solution was heated in a microwave until boiling, being stirred every 20 seconds. The hot agarose was centrifuged at 7000 rpm and 40 °C for 30 seconds in order to remove air bubbles from solution. The solution had to be used immediately otherwise the agarose would gel at ambient temperature. The solution was then used to fill the column templates, as per the procedures described later in this chapter (3.3 and , Section 3.15).

### *3.2.2 Cellulose*

6% w/w cellulose was added to a 12% urea 8% sodium hydroxide which was mixed using a Silverson L4RT mixer at -12 °C until all cellulose was dissolved. Another 2.5% w/w cellulose added to the solution which acted as a physical crosslinker, and 5% w/w epichlorohydrin was added which acts as a chemical crosslinker. The cellulose solution was then used to fill in the 3D printed column template. When in the appropriate mould, the solution was gelled at

75 °C in an oven, build material was removed using acetone, and then the cellulose column was regenerated in water for a week. The column was stored in 20% ethanol until required for functionalisation and testing.

## 3.3 TPMS Column Manufacture

A Solidscape 3Z Pro wax printer was used to print the TPMS columns, and an Up! Mini 3D Printer was used to print the components used to encase the column while the hydrogel filling procedure was followed. The column casing components consisted of a 50 mm long, 10 mm ID cylinder, and a top and bottom cap with entry and exit ports approximately 4 mm inside diameter and 7 mm outside diameter. The caps were designed in this configuration as they would fit a Luer lock syringe which could be used to apply the hydrogel solution to the column template. An orthographic sketch of the column casing is illustrated in Figure 3-2 (a), where the casing dimensions are apparent. An exploded isometric view of the column casing with TPMS column inserted is shown in Figure 3-2 (b).

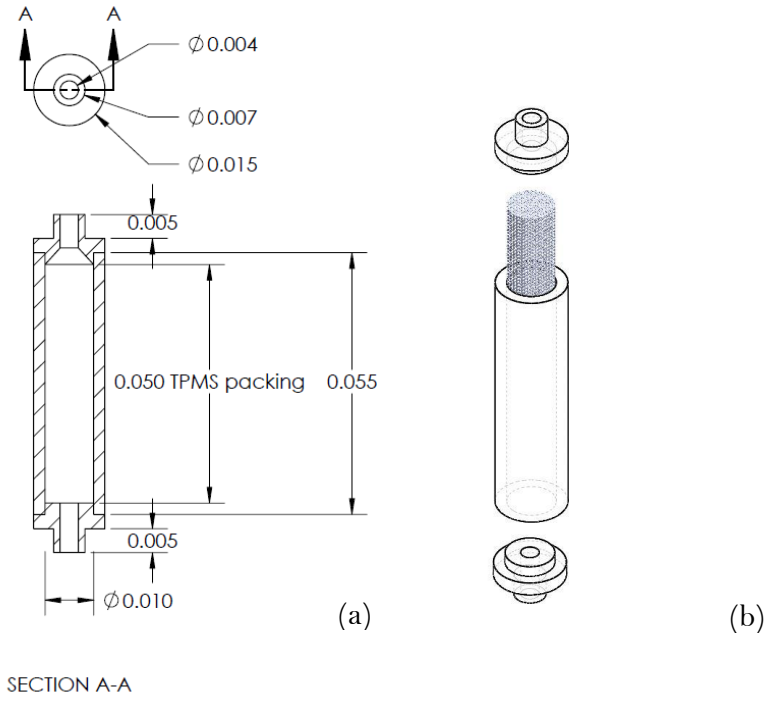


*Figure 3-2: (a) Orthographic section view of column casing apparatus used in column templating (dimensions in mm); (b) exploded isometric view of TPMS column in casing*

The encased TPMS column was included in the column filling apparatus shown below. A Gast 1HAE-25-M104X vacuum pump was connected to a Büchner flask, which was

connected to the encased column via a butterfly valve with 5 mm ID polyethylene tubing. Each connection was sealed with Parafilm to ensure there were no leaks in the system.

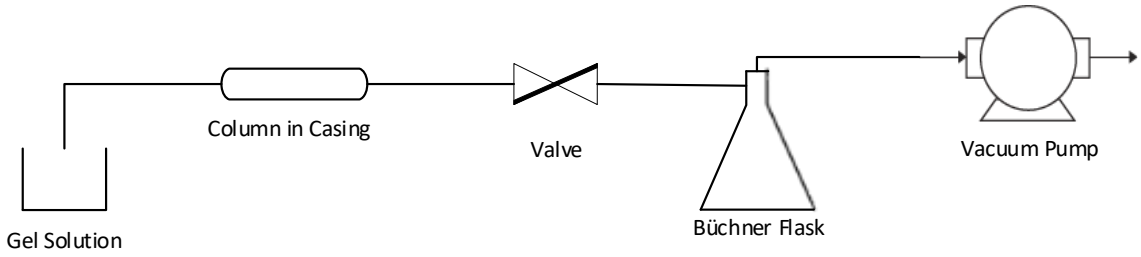


*Figure 3-3: Column filling apparatus showing gel solution reservoir which flows through the TPMS column in casing by vacuum drawn on the system by vacuum pump*

Following printing of the column templates, support material was removed from the matrix by submerging the column in a 50 °C bath of VSO. The column template was left in VSO for 72 hours, then dried in an oven at 50 °C for 24 hours. An example of a 500 μm gyroid column with support material removed is shown in Figure 3-4 below. The gyroid structure is apparent in the image.

*Figure 3-4: 500 μm gyroid wax column, 50 mm long, 10 mm diameter, made on Solidscape Pro 3D printer with support material removed*

The column template was placed in the casing apparatus as outlined above (Figure 3-2). Agarose or cellulose solutions were prepared as in Section 3.2, and column filling apparatus setup up in accordance with Figure 3-3. The solution was then poured into the filling apparatus, and vacuum pump switched on. The valve was slowly opened until the gel solution was observed to be just flowing from the inlet beaker through the column. Once the column

was filled with gel solution, the valve was shut off, column casing removed and placed either in -18 ˚C freezer (for agarose) or an oven at 75 ˚C (for cellulose) so the solutions would transition from solution to gel.

Once the gels were formed, the 3D-printing material was removed by submerging the column in 100% acetone solution. Once all build material was observed to be removed, the columns were washed into 20% ethanol and stored in a refrigerator at 4°C until they were functionalised. It should be noted that cellulose shrinks irreversibly by approximately 3% in acetone; however, as the CDI activation steps are done in acetone, this was seen as an unavoidable problem.

## 3.4 Column Imaging

Two microscopes were used to study the structure and microstructure of the TPMS columns produced in this research: an optical microscope to see the shape of the channels, and a scanning electron microscope (SEM) to see not only the channels but also the porous microstructure of the hydrogel columns. The optical microscope required no sample preparation, however in order to prepare samples for the SEM the agarose and cellulose columns were snap frozen in liquid nitrogen, then dried in a Lanconco Freeze drier. The dried column segments were snapped in two in order to reveal a fracture surface and coated with gold using an Emitech K975X Coater. Samples were placed on carbon paper and analysed in the SEM.

## 3.5 Batch CDI Activation

The equipment used and procedure followed to activate cellulose and agarose for ligand coupling with amine-containing ligands was the same for both agarose and cellulose columns.

Methods from Bethell et al and Hermansen et al [69] [18] were adapted for agarose and cellulose activation and subsequent ligand coupling: 1,1'-carbonyl diimidazole (CDI) was used to activate the hydroxyl groups in the polysaccharide gels. The columns were sequentially washed from aqueous into acetone, with three column volumes of the following mixtures of %acetone/%water added: 30/70, 50/50, 70/30, 100/0. Following this, the columns were placed in three column volumes of fresh acetone to which 0.2 g CDI was added. Each mixture was left on a spinning wheel for 1 hr.

The spinning wheel was an in-house manufactured piece of equipment similar to a Ferris wheel to which centrifuge tubes could be attached. Continued rotating motion promoted constant mass transfer of reactants to the column without the use of a magnetic stirrer which would damage the column.

Following activation, the reactant mixture was decanted from the column and the column was then washed with two column volumes of acetone to remove unreacted CDI groups. The CDI activated columns could be stored in acetone without hydrolysis of the active imidazole groups occurring, however the columns were usually functionalised immediately following activation.

## 3.6 Batch Functionalisation

### *3.6.1 Cation Exchange (CM)*

To couple the ligand 6-aminohexanoic acid to the agarose and cellulose columns, the columns were added to a 6 ml solution of 0.5 M 6-aminohexanoic acid and 1 M sodium bicarbonate, made up to pH 10 using NaOH. 6-aminohexanoic acid forms a covalent bond to the surface of the agarose via an amine linkage, with a free carboxyl group at the end of the ligand for cation exchange. The solution was reacted on a spinning wheel for 48 hours, after which was placed in sodium phosphate buffer at pH 7 (if not being used for protein capture immediately after ligand coupling).

### *3.6.2 Hydrophobic Interaction*

Hydrophobic interaction chromatography columns were created by immobilising a benzylamine ligand to the CDI activated 400 µm channel gyroid agarose matrices. A 6 ml solution of 1:0.11 volumetric ratio of acetone to benzylamine was made and the activated column added to the solution which was placed on a spinning wheel at room temperature for 48 hours. Following ligand coupling, the column was washed into 20% IPA and stored in a 4 °C refrigerator until used.

### *3.6.3 Anion Exchange (DEAE)*

400 µm channel gyroid agarose columns were functionalised with the DEAE ligand 2-chloro-N,N-diethylethylamine hydrochloride using a method based on that developed by Toufik and Labarre [71]. The agarose was placed in 4 M NaOH and 3 M DEAE at a ratio of 1 g agarose:

27 mL DEAE: 20 mL NaOH and stirred in a water bath at 30 °C for 90 minutes. Following reaction, the column was washed in 15 mL of 1 M NaCl, then washed in 15 mL 1 M NaOH followed by 15 mL 1 M HCl three times. The column was stored in 20% ethanol until used.

## 3.7 Recirculating CDI Activation and Functionalisation

In an effort to improve the binding capacity of the column, the CDI activation and CM ligand coupling methods were changed from a batch functionalisation to recirculating functionalisation. 50 mL of reactants (either CDI/acetone mixture, or 6-aminohexanoic acid/sodium bicarbonate solution made to the same concentrations described in Sections 3.4 and 3.6) were placed in a 100 mL Schott bottle and placed on a magnetic stirrer. A SNAP® column (Essential Life Sciences) with 10 µm polyethylene frits and Kalrez O-rings (acetone resistant) was used to encase the hydrogel column, and an Ismatec IPC peristaltic pump with Tygon MHLL tubing 0.76 mm ID was used to recirculate the solution around the column. The connections between each unit were 0.75 mm ID PEEK tubing. A simplified diagram of the setup is shown below (Figure 3-5).

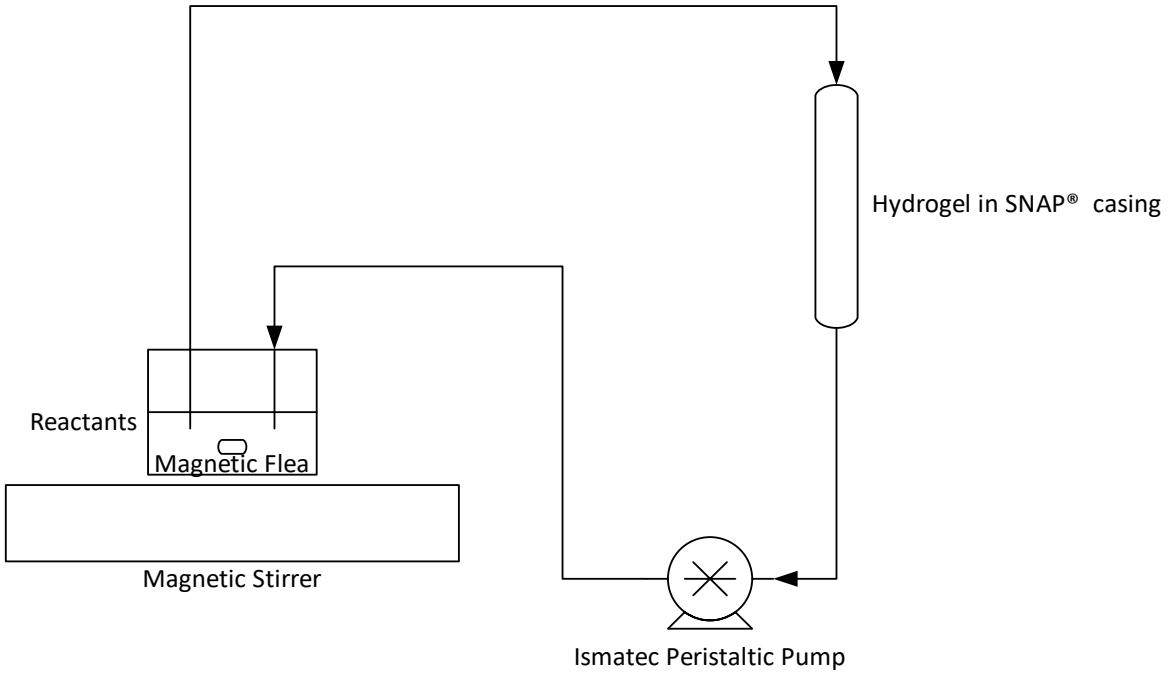


*Figure 3-5: Recirculating functionalisation experimental setup*

The volumetric flowrate for recirculation was set at 1.0 mL/min on the Ismatec pump. The activation step was left for 1.5 hr, following which 20 mL acetone was drawn through the column via syringe to remove any unreacted imidazole groups. The ligand coupling solution

was then applied to the column for 24 hours. Following functionalisation with the ligand, the column was washed into 20% ethanol and stored at 4 °C until used.

## 3.8 Ion Exchange Capacity

Ion exchange capacity for each column was determined by titration method, adapted from Stone and Carta [100]. For the cation exchanger, the surface groups were suspended in 1 M HCl in order to become protonated and left for an hour under agitation. The HCl was then removed, and the method was repeated twice more. After the final protonation step, the gel was washed with DI water until the pH of the eluent was constant at 7. The gel was then suspended in 20 mL of 0.5 M NaCl/0.05 M NaOH and left for 12 hours in a stirred bath. 10 mL of the supernatant was then removed and titrated against 0.1 M HCl. In order to calculate the ion exchange capacity of the column, the volume of 0.1 M HCl required to neutralise a control solution of 0.5 M NaCl/0.05 M NaOH was also determined by titration. Both volumetric amounts were converted to a molar basis. The actual amount of 0.1 M HCl required for neutralisation of 0.5 M NaCl/0.05 M NaOH exposed to the column was subtracted from the control amount of 0.1 M HCl for neutralisation; the difference in values giving the amount of NaOH consumed by the column. Ion exchange capacity (IEX) in equivalent small ion moles per unit volume of column (eQ/ml) is given in Equation 3-1, $n_{control}$ is the number of moles of HCl required for neutralisation of the control sample, and $n_{actual}$ is the number of moles of HCl required for neutralisation of the solution exposed to the column, and $V_{column}$ is the volume of the column.

$$IEX = \frac{n_{control} - n_{actual}}{V_{column}} \tag{3-1}$$

## 3.9 Binding Capacity Measurement

Columns were patted dry and weighed, then equilibrated in binding buffers described in Table 3-3. The supernatant was removed, and 5 ml of protein solution was added to each column. The solutions were left overnight on a spinning wheel, after which the supernatant was removed, and concentration of remaining protein measured using a NanoDrop™. The columns were each washed three times in binding buffer, then washed three times with elution buffer. The concentration in each of these fractions was analysed in the NanoDrop™ and used to determine the amount of protein bound to the column at equilibrium. This procedure was followed five times for each column at different initial protein concentrations: 50 mg/mL, 20 mg/mL, 5 mg/mL, 2.5 mg/mL and 1.0 mg/mL. Equlibrium binding capacities were

calculated by fitting curves to the Langmuir equation (Equation 2-3) using the least squares method. SMA and Freundlich models (Equations 2-6 and 2-7) were also fit to these curves, shown in Appendix 1.

## 3.10 Bind-and-elute Experiments

### *3.10.1 Protein Only*

Each unique TPMS column geometry, channel size, material, and functionality was tested on and ÄKTA10 or ÄKTA Start to prove the columns could operate as they were designed. Firstly, each column was proved to have protein binding capability, then the cell recovery was tested, and finally the protein binding capability in the presence of cells was determined. Each column was placed in a SNAP® column casing tested under the parameters outlined in Table 3-3. Each buffer prepared with filtered with a 0.22 μm filter to remove any suspended contaminants and sonicated in the ultrasonic cleaner for 15 min to remove air bubbles.

*Table 3-3: Buffer and protein parameters for bind-elute proof-of-concept experiments*

| Column | Binding Buffer | Elution Buffer | Protein | ÄKTA |
|---|---|---|---|---|
| CM | 20 mM sodium phosphate buffer, pH 7.0 | 20 mM sodium phosphate + 1 M NaCl, pH 7.0 | 2.0 mg/ml cytochrome c in 20 mM sodium phosphate buffer, pH 7.0 | ÄKTA 10 |
| DEAE | 20 mM sodium phosphate buffer, pH 7.0 | 20 mM sodium phosphate + 1 M NaCl, pH 7.0 | 2.0 mg/ml BSA in 20 mM sodium phosphate buffer, pH 7.0 | ÄKTA Start |
| HIC | 20 mM sodium phosphate buffer + 2 M ammonium sulfate, pH 6.0 | 20 mM sodium phosphate, pH 6.0 | 2.0 mg/ml α-lactalbumin in 20 mM sodium phosphate buffer + 2 M ammonium sulfate, pH 6.0 | ÄKTA Start |

The columns were attached to the ÄKTA hardware, equilibrated in 10 column volumes (CV) of binding buffer. 2.0 mL protein sample was injected onto the column at 1 mL/min, with 1 mL fractions collected. Following sample injection, the column was washed with binding buffer to remove any unbound protein sample, then the buffer was changed to elution buffer. These experiments were repeated at 0.25 mL/min and 2 mL/min in order to determine the effect of flowrate on protein binding capacity.

The 280 nm peaks in the chromatogram were integrated using UNICORN software to determine the area underneath, and then values compared with calibrations done for each protein to determine the mass of protein in each peak. The fractions collected were then analysed in the NanoDrop™ to compare the protein concentration in each fraction with the concentration determined by peak analysis.

HETP for each bind-and-elute experiment were calculated using equations 2-22 to 2-27, with Gaussian parameters for HETP determined using equations 2-11 to 2-15. Sample calculations are shown in Appendix 2.

### *3.10.2 Protein and Yeast*

Cell passage and the effect of cells on binding capacity was measured by performing bind-elute experiments on each column using an on-sample of 0.5 w/w% yeast in binding buffer only, and yeast with protein in binding buffer. The buffer and protein concentration and pH were the same as was outlined in Table 3-3. All fractions were collected and analysed on the NanoDrop™ at 280 nm and on the Spectrophotometer at OD 600 nm for cell concentration. These values were compared with the recorded peak intensities at 280 nm and 600 nm from UNICORN software.

## 3.11 Gel Electrophoresis

Fractions collected from the protein and yeast runs on G300A-CM were analysed for protein concentration using gel electrophoresis. 16.25 µL of each fraction was pipetted into Eppendorfs, to which 6.25 µL and 2.5 µL of LDS buffer and β-mercaptoethanol were added, respectively. Eppendorfs were placed in the gel block and heated at 95 °C for 15 min to denature the proteins in each sample. Samples were then centrifuged at 11,000 rpm for 5 mins. 10 µL of each sample was pipetted into individual lanes of the NuPAGE 4-12% Bis-Tris gel (in sequential order, following the order the fractions were collected). 10 µL of protein standard was pipetted into three lanes of the gel. The gel was placed in the buffer tank which was filled with 1X SDS running buffer, and the tank was run at 200 V for 40 mins.

Following this, the gel was removed and stained with Coomassie Brilliant Blue stain solution (1% Coomassie Brilliant blue in 100 mL/L acetic acid) for 24 hours. After 24 hours, the stain was removed and destain (10% acetic acid, 50% methanol, 40% deionised water) was applied twice for another 24 hours, until the blue colour was removed from the gel. The gel was imaged using the LAS500 Camera.

## 3.12 Protein Breakthrough

Column breakthrough experiments were completed for the cellulose and agarose CM columns. The columns were packed into a SNAP® column casing and attached to the ÄKTA10 Explorer. 2.0 mg/ml cytochrome c was continuously loaded on to the column at a constant flowrate. Each run was left until no change in outlet concentration was overserved. The flowrates tested were 0.25 mL/min, 1.0 mL/min and 2.0 mL/min. For the 400 μm cellulose gyroid, 5.0 mL/min and 10.0 mL/min were also tested. 5.0 mL fractions were continuously taken during each run, which were then analysed in the NanoDrop™ to measure protein concentration. The results were analysed where saturation binding capacity and dynamic binding capacity at 10% and 50% were determined for each column.

## 3.13 CDI Reactivity

The NanoDrop™ was used to determine the activity of CDI over time in acetone and water, to gain insight into any limitations of the CDI activation method. 0.01 g of CDI was placed into a quartz cuvette in the NanoDrop™, to which 1.0 mL of acetone was added. The run started, and absorbance measurements were taken every 30 seconds to measure the CDI concentration in the acetone over time. Each trial was run for one hour. The experiment was repeated with 1.0 mL of deionised water instead of acetone.

## 3.14 Cell Recovery

1.0 mL of 0.5% w/w yeast samples were prepared in 20 mM sodium phosphate buffer, pH 7.0 in order to test the number of cells recovered in a single pulse of yeast through each of the CM columns. Columns were placed in SNAP® casings and attached to the AKTA10 Explorer. After column equilibration, the sample was loaded onto the column at 1.0 mL. The flow-through of yeast cells was observed by monitoring the UV output at 600 nm. After two column volumes, the buffer flowrate was increased to 10 mL/min to push out any entrapped cells. Fractions were collected across the run, and the optical density of these samples at 600 nm was measured using the Spectrophotometer, as well as the intensity of the peaks recorded on Unicorn software and were used to determine the mass of yeast in each fraction run. This was repeated for different sample loading flowrates of 1.0 mL/min, 2.0 mL/min, 5.0 mL/min, 7.5 mL/min, and 10.0 mL/min. The wash flowrate was always 10.0 mL/min.

## 3.15 Monolithic Column Fabrication

30 mm long, 10 mm diameter columns with 16 x 1 mm ID straight monolithic channels (Figure 3-6) were made from cellulose and agarose and used in the RTD studies to determine the differences in key properties of the two hydrogels.

*Figure 3-6: Solidworks model of 30 mm long, 10 mm dimeter column with 16 x 1 mm diameter channels*

A negative template for the column was designed in Solidworks (Figure 3-7) and printed out of acrylonitrile butadiene styrene (ABS) on an Up! Mini 3D-printer. The smaller diameter section at the top of the template had nine x 1 mm holes in the top to allow the cellulose or agarose solution to be distributed evenly to the monolithic section of the template. A similar section was used at the bottom of the template to enable flow of solution, but a 20 mm diameter cap was included to stopper the template into the template casing. The open end of the column casing was capped using one of the caps from the TPMS filling procedure. The template was placed in a 10 mm ID casing (the same used in Section 3.3) and filled with agarose or cellulose solution. The columns we left to gel, casing removed, then ABS template dissolved out of the column using acetone. The columns were left in 20% ethanol until used.

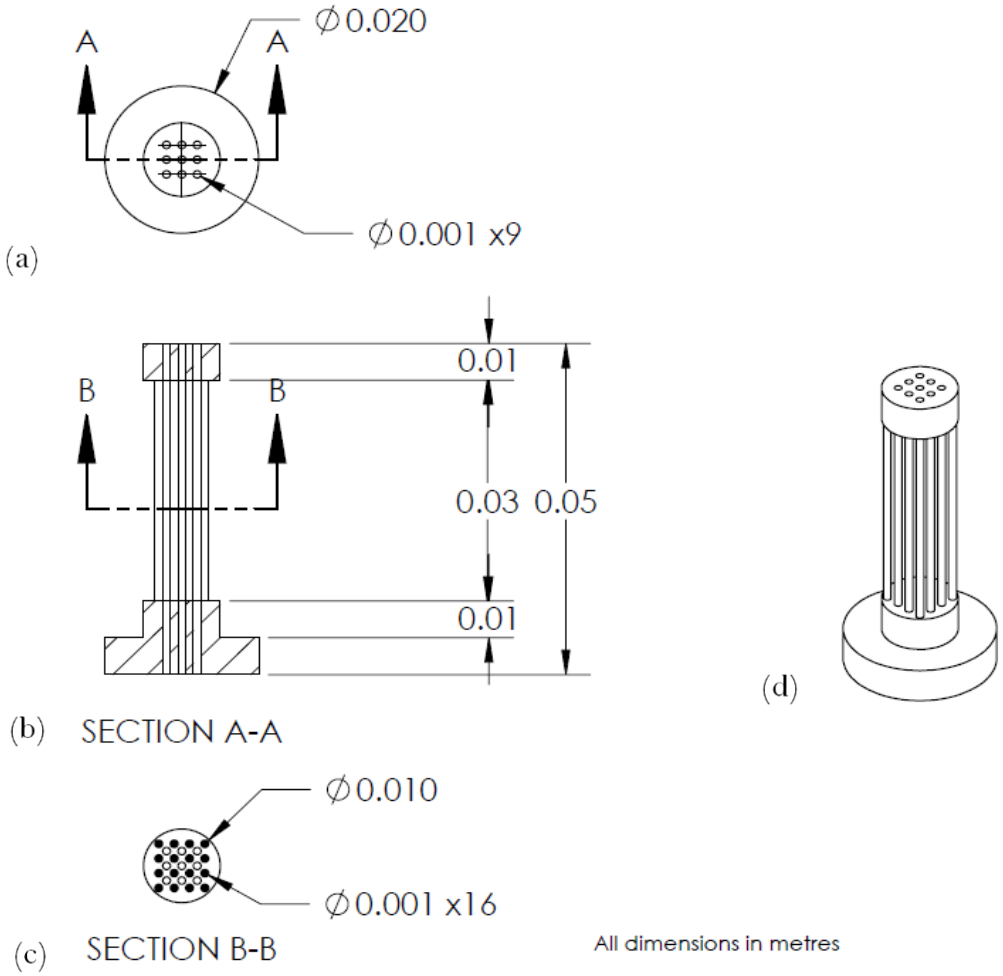


*Figure 3-7: Sketch of monolithic column negative template; (a) plan view, (b) section A-A, (c) section B-B, (d) isometric view*

## 3.16 Hydrogel Penetration Determination

30 mm long agarose monoliths columns were made and functionalised using the batch and recirculating methods outlined in Section 3.15. Columns were then submerged in 50 mg/ml cytochrome c in 20 mM sodium phosphate buffer at pH 7.0 and left for protein to bind for 24 hours. Unbound protein was removed by washing the columns in buffer three times. The columns were then cut into 18 slices and washed again in binding buffer. The Leica microscope was used to take images of the slices, and radial penetration of cytochrome c into the monolith channels and wall was measured using Fiji.

## 3.17 Inverse Size Exclusion Chromatography/Residence Time Distribution

Inverse size exclusion and residence time distribution use the same method, although determine slightly different parameters. Two inert tracers were used to determine mean void and pore volume on selected TPMS columns, and the monolithic columns designed in Section 3.15. 1.0 mg/mL blue dextran and 1.0% v/v tracer solutions were prepared in deionised water. Hydrogel columns were placed in SNAP® column casings and equilibrated in deionised water. 100 µL tracer was injected onto the column, and the UV output was recorded. For each column and tracer, at least 5 injections of tracer were made. Finally, the monoliths were removed from the SNAP® casings, and the same tracer pulses were applied the empty column to determine the dead volume of the hardware, which was subtracted from the mean residence volume.

# Chapter 4. Column Prototyping and Adsorption Characterisation Under Static Conditions

## 4.1 Introduction

With the design and manufacture methods of TPMS hydrogel columns for chromatography described in the previous chapter, it is appropriate to start the discussion of these columns with an analysis of the actual hydrogel structures achieved by the negative templating method, and proof that the hydrogels were successfully functionalised for chromatography. This chapter is split into two main sections. The first section presents the geometric results: optical microscope and SEM images to analyse the TPMS channel structure achieved on the hydrogels and inverse size exclusion chromatography results showing the differences in channel voidage and pore voidage on different TPMS structures of agarose and cellulose. The second section quantifies the adsorption capacity of the columns under static conditions: ion exchange capacity was determined to give the ligand density of the TPMS hydrogel structures, and equilibrium binding capacity was determined for common proteins. These adsorption characteristics were compared with commonly used protein adsorption media. The results herein are a proof-of-concept for TPMS hydrogels to act as adsorptive media.

## 4.2 Column Prototyping

The TPMS columns were manufactured based on processes outlined in Chapter 3 are presented in Table 4-1 below. Each column was designed with a voidage of 50%, meaning that the wall thickness was the same size as the channel size. Agarose gyroids with channel sizes of 300 μm, 400 μm, and 500 μm were made, while cellulose gyroids with 400 μm and 500 μm were made. A 300 μm channel size gyroid of cellulose was not made due to difficulties encountered in casting the columns with cellulose, as the high viscosity of the solution caused the template to break. Two agarose Schwarz diamond columns were also made, one with 400 μm channel size and one 500 μm channel size. A 300 μm Schwarz column was not able to be produced because the file size of the completed column was too large for the computer processing power available at the time to convert the model to a .stl file. Finally, due to processing defects, the columns were cut to size using a scalpel, meaning not all columns were the specified 5 cm length. Column lengths and TPMS surface areas are also included in Table

4-1. The surface areas were calculated by multiplying the TPMS unit cell specific surface area [95] by the column volume, yielding the surface area of the TPMS geometry which did not include the surface area of the porous structure.

*Table 4-1: TPMS columns prototyped and tested in this chapter*

| Column ID | Material | TPMS | Channel Diameter (μm) | Functional Group | Length (cm) | TPMS Surface Area ($cm^2$) |
|---|---|---|---|---|---|---|
| G300A-CM | Agarose | Gyroid | 300 | CM | 3.9 | 157.7 |
| G400A-CM | Agarose | Gyroid | 400 | CM | 4.7 | 142.5 |
| G500A-CM | Agarose | Gyroid | 500 | CM | 4.7 | 114.1 |
| G400C-CM | Cellulose | Gyroid | 400 | CM | 4.5 | 136.4 |
| G500C-CM | Cellulose | Gyroid | 500 | CM | 4.6 | 111.6 |
| SD400A-CM | Agarose | S. Diamond | 400 | CM | 4.5 | 172.8 |
| SD500A-CM | Agarose | S. Diamond | 500 | CM | 4.4 | 135.1 |
| G400A-DEAE | Agarose | Gyroid | 400 | DEAE | 3.3 | 100.0 |
| G400A-HIC | Agarose | Gyroid | 400 | Benzene ring | 3.6 | 109.1 |

CM columns made from agarose and cellulose were functionalised using the CDI activation method with 6-aminohexanoic acid immobilised to the polysaccharide matrices. Two further 400 μm agarose gyroid columns were produced: one activated with CDI with benzylamine immobilised to the agarose matrix to create a hydrophobic interaction chromatography column, and one activated with the concentrated NaOH with a DEAE ligand immobilised to the agarose matrix create an anion exchange column. These last two columns were included as a proof-of-concept for the wide range of chromatographic functionalisation that could be achieved using the 3D-printing prototyping method for chromatography columns.

In determining gyroid structures that could be printed, templates down to 250 μm channel diameter and wall thickness were achieved however the files were too large to produce columns larger than 1 cm long. In addition, the pressures required to fill the column templates with gel solution were much higher than for larger channel diameters because of the change in permeability. These pressures often resulted in the template structure breakage when the hydrogel solution was applied to fill the TPMS template. Therefore, the smallest

channel diameter in the columns was 300 μm as this did not result in the template breaking while being filled with hydrogel solution. Despite these features not being in the same range as beaded resins used in HPLC (on the order of 5 μm), these channels are of a similar scale to "Big Beads" (100 – 300 μm) [101], meaning the TPMS columns should provide competitive protein adsorption to some commercial chromatography resins.

As further 3D-printing techniques are developed, and computational limitations are overcome, it is expected that TPMS columns with smaller diameter channels and a larger overall volume will be able to be made. The columns in this research were limited to 1 cm diameter and 5cm long; for column chromatography, longer columns are desirable for better peak resolution, and wider columns reduce wall effects. Advancements in 3D-printing technologies would make the TPMS columns made in this research more sought-after for adsorption-only processes, as smaller feature are likely to yield a higher surface area, hence greater protein binding capacity, and improve the potential applications of the columns in protein processing. For example, currently the CELLINK BIO X printer can print to 1 μm resolution in the x, y, and z domain [93]. The CELLINK BIO X was used to print cell scaffolds out a multitude of materials including cellulose, alginate and collagen using extrusion and inkjet methods. Furthermore, the printer can produce structures with high enough resolution for cartilage, muscle, and organ structures [93]. The specifications required for TPMS columns would be easily achievable on this printer because of the resolution available and range of materials with which it can print. The high resolution would mean the negative templating step is not required, and the final column produced would not be marred by the slight surface roughness caused by coarse printing layers. Surface roughness caused by templating is discussed in the next section.

### 4.2.1 Structure Confirmation

The progression of SolidWorks design, to 3D printed model, to agarose column to carboxy-methyl functionalised chromatography column with cytochrome c bound is shown in Figure 4-1 below for a 500 μm gyroid agarose column. Comparison between the CAD model (Figure 4-1 (a)) and the Solidscape printed template (Figure 4-1 (b)) clearly shows TPMS features replicated in the printing process. In the agarose column (Figure 4-1 (c)), it is more difficult to see the features, and air bubbles in the channels are more apparent. An image of these columns presented by Fee in Current Opinion in Chemical Engineering [51] however shows the TPMS features with much more clarity (Figure 4-2). This demonstrates

the successful prototyping of a chromatography column with a controlled geometry and proven adsorptive capabilities.

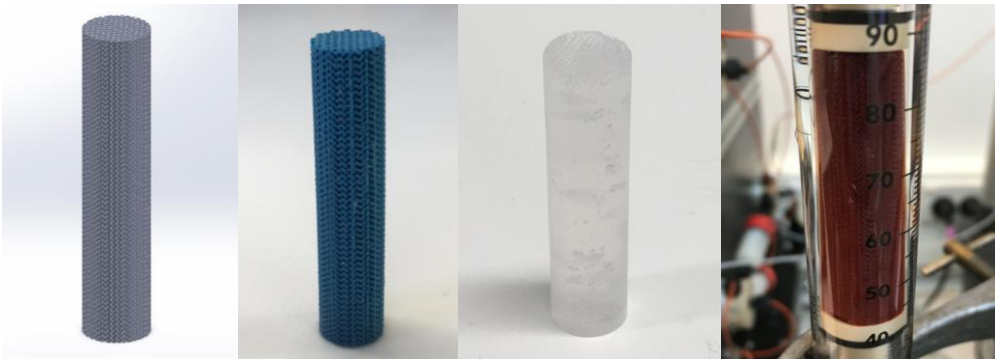


*Figure 4-1: Progression of TPMS column design to functional chromatography column. (a) SolidWorks model, (b) Solidscape printed template, (c) agarose column, (d) cytochrome-c bound to agarose column in glass casing*

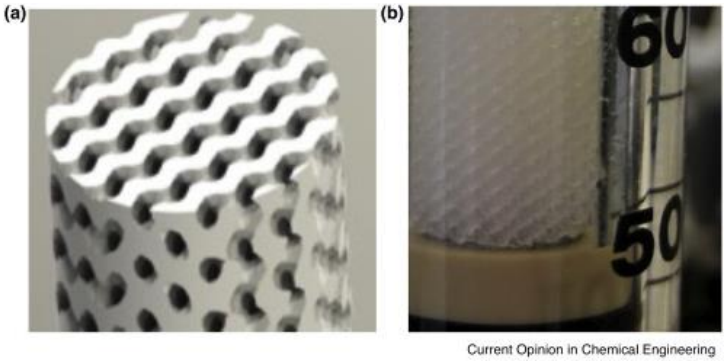


*Figure 4-2: Gyroid TPMS (a) SolidWorks design and (b) 6% agarose hydrogel in glass casing [51]*

The SolidWorks design was successfully printed as a gyroid structure, with good fidelity between the column design and printed structure. Images from the optical microscope show the gyroid shape is maintained in the structure (Figure 4-3). In Figure 4-3 (a) lines were added to the image to explicitly demonstrate the sinusoidal gyroid nature of the channel structure achieved as per the design. In Figure 4-3 (b) one of the main limitations of the printing technique becomes apparent: the printing layer and file slice resolution compared with the channel diameter means that the channel surfaces are not smooth, rather there is a roughness apparent on the surface. It is expected that the roughness will propagate through the production of the hydrogel columns from the template. This could cause problems in several aspects of the column performance: the roughness will increase localised turbulence and axial dispersion in the columns and provide edges onto which cells may become entrapped. The former would hinder protein binding at higher velocities by increasing axial dispersion [102], and the latter would reduce cell passage through the columns, especially at

low velocities. Furthermore, the effects of the layers apparent in the structure are likely to become more prominent for smaller channel diameters because of a defect size to channel diameter ratio, meaning smaller channels could see more cell entrapment. These are limitations of both the computing power required to process smoother curved surfaces (reduce pixelated roughness) and the 3D printing resolution.

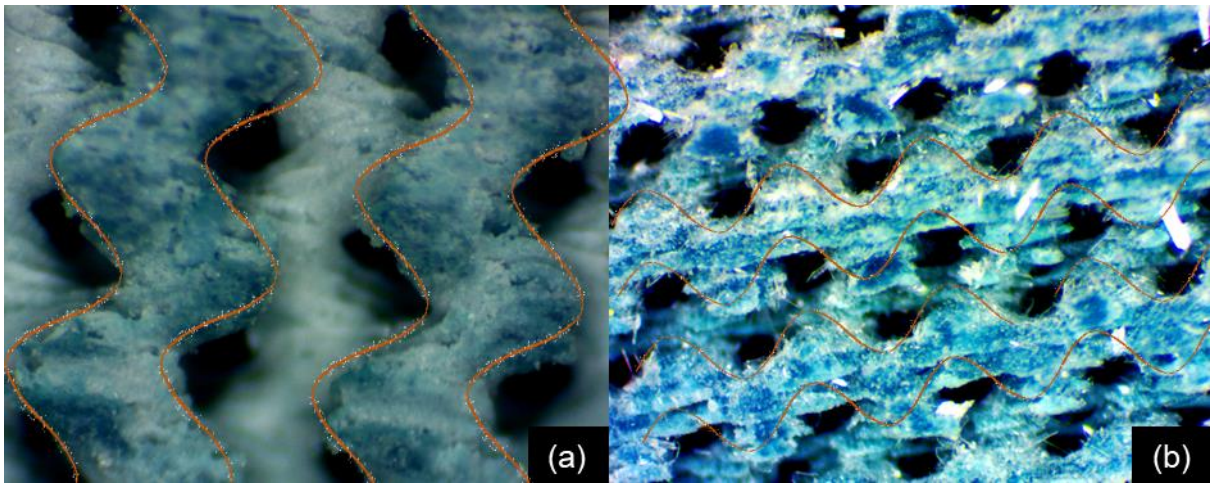


*Figure 4-3: Optical microscope images of 3D-printed 500 µm gyroid template: (a) gyroid channel lattice; (b) gyroid lattice with roughness from printing resolution*

Smoothing the template using a chemical method is a possibility to prevent the roughness in the channel walls of the TPMS columns. However, the chemical selected must not completely dissolve the template, or dissolve it to a degree whereby the walls of the template become smaller, and the template is no longer identical to the designed, controlled geometry structure that is required. The template material was a proprietary wax which was soluble in wax and hot water. Smoothing of the surface was attempted with 1.0 mL of 5% w/w acetone pulsed through the lattice. However, this was not attempted until after the hydrogel columns were made, so the columns in this research have the roughness from the template. It is recommended that future columns produced using this method incorporate a template smoothing step.

Moving from the 3D-printed template to the hydrogel columns, optical microscope images were taken to confirm the structure of the TPMS design was present in the hydrogel columns for all geometries and channel sizes produced in this work. The gyroids are shown in Figure 4-4, where the gyroid structure was apparent in the three different channel sizes. Likewise, the Schwarz diamond images (Figure 4-5) prove that the Schwarz diamond lattice was successfully produced using the negative templating method. The channel diameters were correct as per the template specifications, meaning the macro structure of the TPMS design

was successfully prototyped in a hydrogel column. The limitation of these images is they do not provide resolution much higher than the same order of magnitude as the channels themselves. Scanning electron microscopy (SEM) was instead used to provide images of the columns' features in higher resolution.

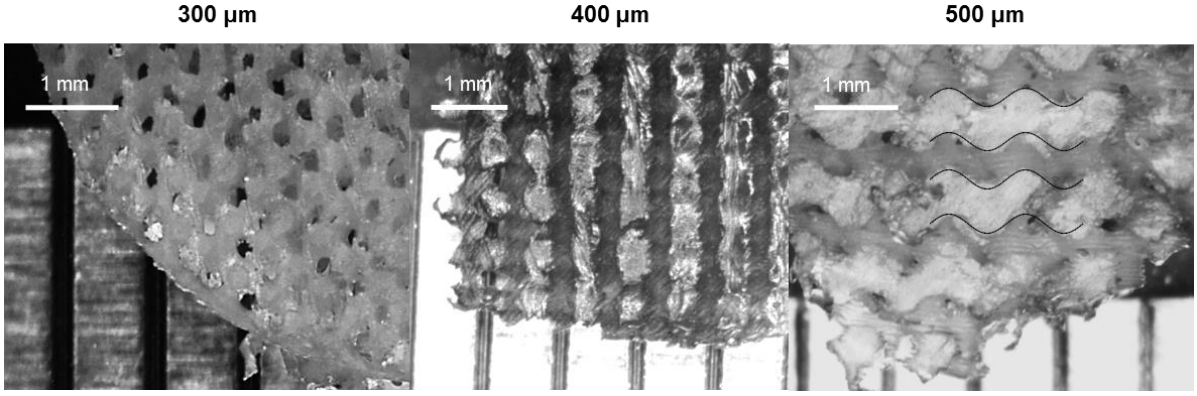


*Figure 4-4: Optical microscope images of gyroid hydrogel columns. Lines added to 500 µm gyroid image to highlight the channels and walls*

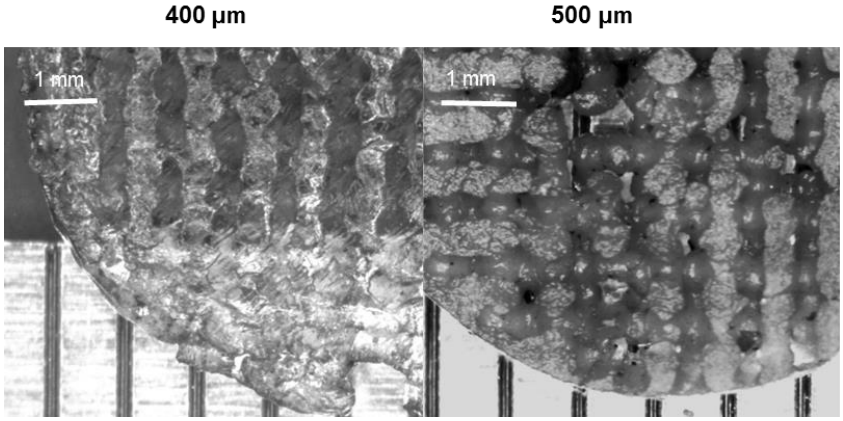


*Figure 4-5: Optical microscope images of Schwarz diamond hydrogel columns*

SEM images were taken to obtain a clearer view of the channel structure and potential roughness of the TPMS columns (Figure 4-6). The SEM images support the results shown by the optical microscope whereby the gyroid and Schwarz diamond macrostructure of the TPMS channels were successfully produced by the negative templating method. Furthermore, the SEM images show the structures were produced in both cellulose and agarose hydrogels, both with good fidelity between the SolidWorks model and final hydrogel structure.

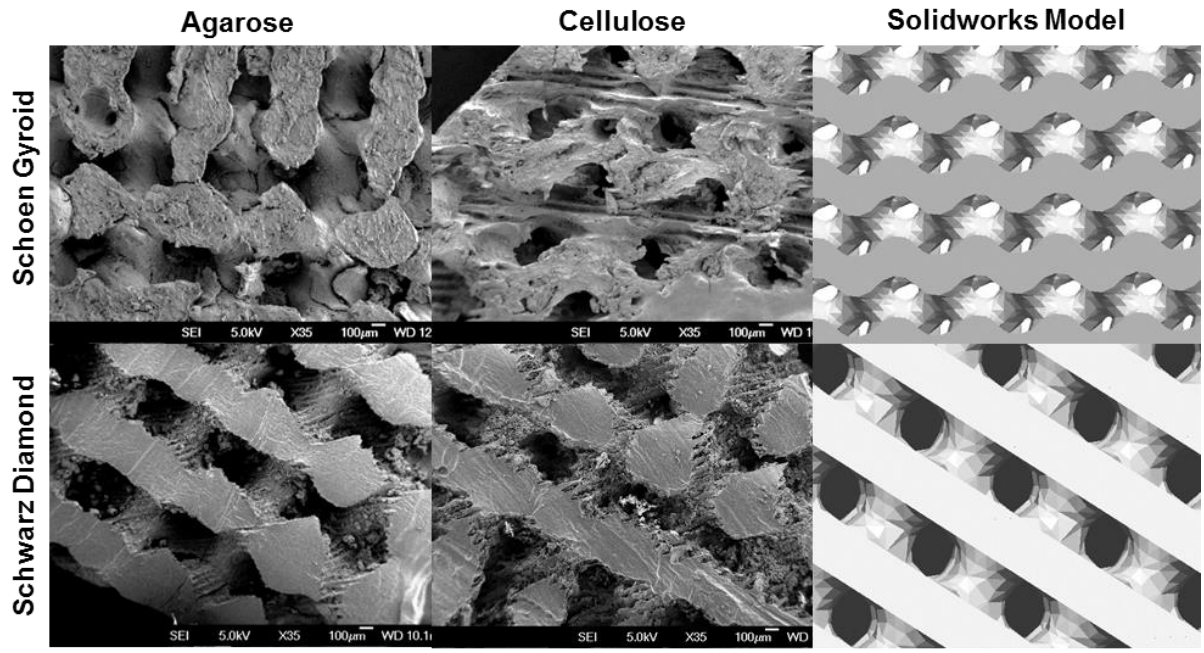


*Figure 4-6: Scanning electron microscope images of cellulose and agarose Schwarz diamond and gyroid columns compared with the initial SolidWorks model*

The propagation of 3D-printed layers from the negative template through to the final hydrogel column are evident in the SEM images, and have been highlighted below (Figure 4-7). The implications of this on protein binding and solid passage have already been speculated, and evidence of these effects are discussed in results presented later. Based on the images presented, there was no obvious difference in agarose and cellulose columns on the macroscale. This was expected as the templates were identical.

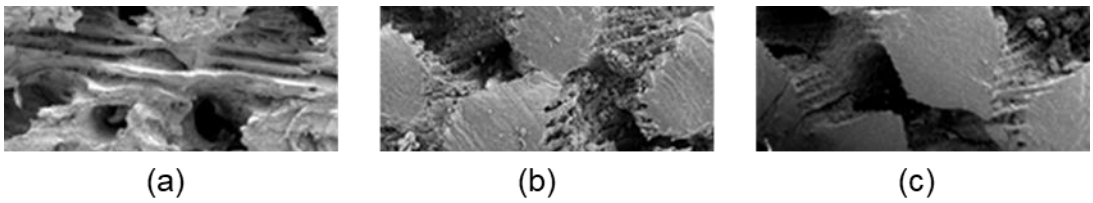


*Figure 4-7: Instances where layering effect of 3D-printer propagated through to final hydrogel column: (a) cellulose gyroid, (b) cellulose Schwarz diamond, (c) agarose Schwarz diamond*

## 4.3 Inverse Size Exclusion Chromatography

Acetone and blue dextran tracers were used to generate RTD curves in the inverse size exclusion chromatography experiments on G400A-CM, SD400A-CM and G400C-CM in order to quantify the pore volume in different columns. Each TPMS column was designed with an interstitial void fraction of 0.5, which corresponds to the interstitial void volume or

the volume of the channels, although the columns had an unknown pore volume. The curves showed a clear difference in elution of the two tracer molecules: acetone peaks had a long tail because the molecule is small and interacted with the entire pore volume, while blue dextran is large and was excluded from the pores, only flowing through the interstitial volume hence eluting earlier than acetone (Figure 4-8). The mean elution volume of blue dextran corresponded to the interstitial volume, in this case the volume of the TPMS channels, and the mean elution volume of acetone was the total void volume in the columns: the sum of the interstitial volume and pore volume. The difference between the mean elution volume of acetone and blue dextran on each column gave the pore volume.

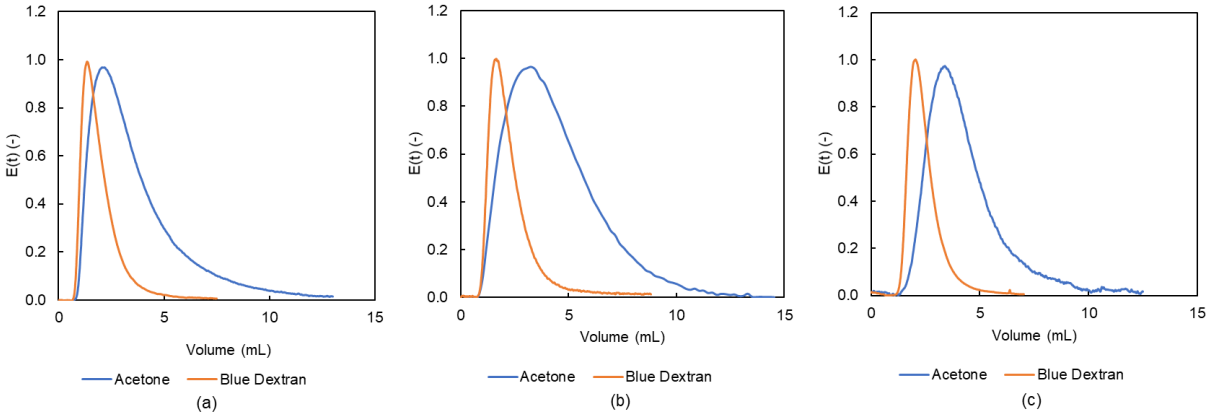


*Figure 4-8: RTD curves of acetone and blue dextran on (a) G400A-CM; (b) SD400A-CM and (c) G400C-CM*

The dead volume of the chromatographic hardware was measured to be 1.0 mL which was subtracted from the mean residence volumes of each tracer. Total void fraction, interstitial fraction, and pore fractions were calculated from the mean elution volumes (Table 4-2). Given each TPMS column was designed with the same interstitial voidage, the mean elution volume of blue dextran and hence interstitial fraction should have been equal for each column. In reality, these were 0.26, 0.40 and 0.41 for G400A-CM, SD400A-CM and G500C-CM respectively, demonstrating a significantly lower interstitial void fraction than was designed. The measured pore volumes resulted in total void fractions over 0.90 in SD400A-CM and G400C-CM. These are not unreasonable values: a column packed with 6% Sepharose Fast Flow beads have been measured to have a total void fraction of 0.90 with pore fraction 0.55 [103], and cellulose has void and pore fractions above 0.90 and 0.6 respectively [104].

*Table 4-2: Elution volumes and void fractions determined from inverse size exclusion experiments for G400A-CM, SD400A-CM and G500C-CM.*

| | **Blue Dextran Mean Elution Volume** (mL) | **Acetone Mean Elution Volume** (mL) | **Total Void Fraction, $\varepsilon$** (-) | **Interstitial Fraction, $\varepsilon_i$** (-) | **Pore Fraction, $\varepsilon_p$** (-) |
|---|---|---|---|---|---|
| G400A-CM | 0.96 | 2.53 | 0.69 | 0.26 | 0.43 |
| SD400A-CM | 1.42 | 3.28 | 0.93 | 0.40 | 0.53 |
| G400C-CM | 1.45 | 3.32 | 0.94 | 0.41 | 0.53 |

Based on structure confirmation via microscopy (Section 4.2.1), columns were assumed to have been produced as per the TPMS design, however columns used in actual chromatography experiments could not be inspected for their internal structure as this would have required the columns to be broken. Therefore, there is a possibility that sections of the columns were plugs of solid hydrogel caused by template breakages upon filling the templated structure, or where the hydrogel solution dissolved the template before filling. The plugs of hydrogel would reduce the interstitial and pore volume. In the latter case, this would support the fact that G400A-CM had a lower interstitial volume than was designed, as the agarose hydrogel solution was at 40 ˚C, potentially dissolving parts of the 3D-printed template. This is a limitation of the negative templating method whereby a combination of vacuum and syringe were used to make the columns because a constant and uniform pressure was difficult to maintain when filling the column templates. A filling system with good process control or a hydrogel 3D-printer would be much more effective in ensuring all columns produced conformed to the design structure.

Steps to negate the inconsistency in negative templating have already been made, where success in producing basic controlled geometry structures and even TPMS structures using direct 3D-printing have seen consistent success. The work by Huber et. al. [21] points towards TPMS hydrogel structures being printed directly, meaning that problems with negative templating will no longer be an issue.

## 4.4 Static Adsorption Characterisation

The static adsorption ability of ion exchangers is presented using two measures: ion exchange capacity for small ions (such as $Na^+$ or $Cl^-$) which can give the total ligand density assuming one ion adsorbs to one ligand, and the equilibrium binding capacity of certain analytes. Ion exchange capacity was determined using the titration method, and equilibrium binding

capacity was determined by applying the Langmuir model to adsorption experiments (following methods from Sections 3.8 and 3.9).

### 4.4.1 Ion Exchange Capacity

For ion exchange capacity of the CM columns, the number of moles of HCl used to neutralise a supernatant of 0.05 M NaOH/0.5 M NaCl which previously had the protonated cation exchange column immersed in it was determined via acid/base titration. This value was compared with the number of moles required to neutralise a 0.05 M NaOH/0.5 M NaCl control solution that was not immersed in the column. In the column supernatant, there were more $H^+$ ions, so required less NaOH than the control to reach the equivalence point. The opposite was used in determination of the ion exchange capacity of the DEAE column, where the column was immersed in HCl and supernatant titrated against NaOH. For a strong acid/base titration, the equivalence point is at pH 7.0 which was shown experimentally in the control solutions (Figure 4-9). The example titration curve for the control samples showed the equivalence point was at pH 7. Again, the opposite was done in determination of the ion exchange capacity of the DEAE column, where the column was immersed in HCl and supernatant titrated against NaOH.

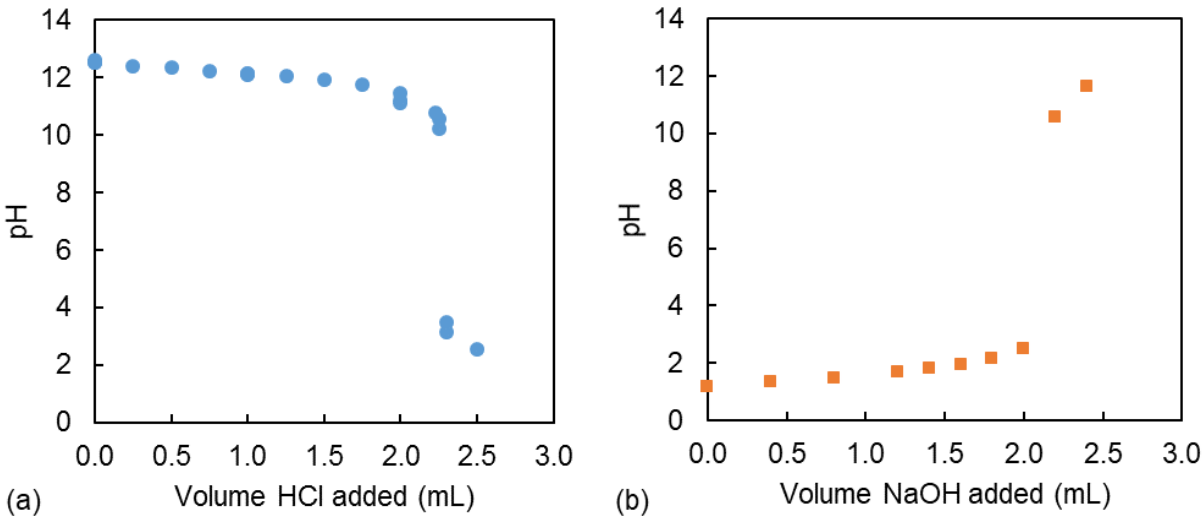


*Figure 4-9: Neutralisation of ion exchange capacity reference solutions for (a) 0.05 M NaOH and (b) 0.05 M HCl*

The ion exchange capacity (*IEX*) in μeQ/ml was calculated using Equation 3-1. This value gave the maximum number of $H^+$ or $OH^-$ that would bind to the cation or anion exchanger respectively; in other words, the number of ion exchange ligands on the resin assuming 1:1 ion adsorption to ligand sites which is valid for small ions.

Ion exchange capacities for the ion exchange columns are given below (Table 4-3). Table 4-3 gives the ion exchange capacities on a column volume basis and on a surface area basis. The surface area in these calculations was the surface area based on TPMS features only, not considering the microporous structure. It was assumed that porosity of each hydrogel would be constant, regardless of the characteristics of the TPMS features and that the ligand immobilisation density on each type of hydrogel would also be constant.

*Table 4-3: Ion exchange capacities of CM and DEAE columns*

| Column | Ion exchange, volume basis | Absolute uncertainty | Ion exchange capacity, surface area basis | Absolute uncertainty |
|---|---|---|---|---|
| | μeQ/mL | μeQ/mL | μeQ/cm² | μeQ/cm² |
| G500A-CM | 35.6 | ±0.8 | 1.15 | ±0.03 |
| G400A-CM | 49.3 | ±1.3 | 1.28 | ±0.04 |
| G300A-CM | 65.1 | ±1.6 | 1.26 | ±0.04 |
| SD500A-CM | 50.6 | ±1.2 | 1.29 | ±0.04 |
| SD400A-CM | 70.3 | ±2.3 | 1.44 | ±0.05 |
| G500C-CM | 54.5 | ±1.5 | 1.76 | ±0.05 |
| G400C-CM | 78.9 | ±2.6 | 2.04 | ±0.07 |
| G400A-DEAE | 80.1 | ±1.3 | 2.08 | ±0.04 |

Ion exchange capacity increased with decreasing channel diameter, and the cellulose columns had a higher ion exchange capacity than their agarose counterparts. SD400A-CM had the highest ion exchange capacity for all the agarose columns; it was the agarose column with the largest surface area based the TPMS geometry hence more area for ligand immobilisation and subsequent ion binding. G300A-CM had the highest ion exchange capacity for the agarose gyroid columns, at 65.1 ± 1.6 μeQ/ml, which decreased to 49.3 ± 1.3 μeQ/ml and 35.6 ± 0.8 μeQ/ml for G400A-CM and G500A-CM respectively. The trend in decrease in ion exchange capacity with increasing channel diameter tracked closely to the trend in decreasing specific surface area with increasing channel diameter. This is demonstrated by having a nearly constant ion exchange capacity on a surface area basis, also shown in Table 4-3. For each hydrogel type, it was assumed that the surface area attributed to the gel by pores is constant, so would cancel out in an analysis. Going between G300A-CM and G400A-CM, this assumption appears to be hold, as the ion exchange capacities on a surface area basis were 1.26 ± 0.04 μeQ/cm² and 1.28 ± 0.04 μeQ/cm². This shows that the porosity and ligand

immobilisation density was constant. However, for G500A-CM, the ion exchange capacity on a surface area basis was lower, at 1.15 ± 0.03 μeQ/cm². According to the previous assumptions, this should have been constant. The results from inverse size exclusion chromatography showing that columns were not produced as per the TPMS design likely mean that the surface area analysis was incorrect. Furthermore, the microporous structure was likely not constant, because changing with ligand density as the functionalisation changes the hydrogen bonding in the hydrogel structure, responsible for holding the hydrogel structure together. However, the effects of functionalisation processes on cellulose and agarose are not widely understood. The degree of crosslinking and gelation time effects the porosity of cellulose, however similar studies on agarose, and studies considering ligand immobilisation have not been done [20].

The cellulose columns had a higher ion exchange capacity on both the volume basis and surface area basis compared with their agarose counterparts. For example, the ion exchange capacity for G500A-CM was 35.6 ±0.8 μeQ/mL, while for G500C-CM the ion exchange capacity was 54.5 ±1.5 μeQ/mL. There are several reasons for cellulose having a higher ion exchange capacity than agarose, such as more available ligand immobilisation sites because of a higher percentage of polysaccharide available, or greater surface area from cellulose hydrogels having smaller diameter pores than agarose. Cellulose had a greater percentage of polysaccharide in the hydrogel because of its addition as a physical crosslinker and hence providing more hydrogel groups in the matrix for the ion exchange ligand to be immobilised to: there was a total of 7.5% w/w cellulose in the hydrogel solution compared with 6% w/w in the agarose solution. This alone does not contribute to the increased capacity; if it did, the expected ion exchange capacity for G500C-CM and G400C-CM would be approximately 44.5 μeQ/ml and 61.6 μeQ/ml respectively. This was calculated on the by increasing the ion exchange capacity of the agarose columns made with 6% agarose to 7.5% agarose. This assumption leads to a lower ion exchange capacity than was observed, therefore it is clear that the porosity of the cellulose contributed to the higher ion exchange capacity in cellulose.

The same trend in increasing ion exchange capacity with decreasing channel diameter (and hence surface area) that was seen in the agarose columns was also observed in the cellulose columns; capacity increased from 54.5 ±1.5 μeQ/mL to 78.9 ± 2.6 μeQ/mL from G500C-CM to G400C-CM. Again, the higher surface area of smaller channel diameter columns was attributed to this. However, there was an even more significant difference in ion exchange capacity on a surface area basis for the cellulose columns compared with the agarose columns, CCM had an ion exchange capacity on a surface area basis of 1.76 ± 0.05 μeQ/cm² and

G400C-CM was 2.04 μeQ/cm². As before, this would be constant if the surface area contribution of the pores were constant, but it is likely that this was not the case in cellulose. It was observed that porosity varied significantly for cellulose hydrogels produced at the same gelling and crosslinking conditions [20]. The cellulose TPMS columns in this research reflected these conclusions, leading to differences in the ion exchange capacity on a surface area basis. This would make consistent reproducibility of a cellulose column difficult to ensure in a product.

The ion exchange capacity of G400A-DEAE was high on both a volume and surface area basis compared with columns of other functionalities tested. The ion exchange capacity on a volume basis was 80.1 ± 1.3 μeQ/ml, and on a surface area basis was 2.08 ± 0.04 μeQ/cm². This was an unexpected result, given the functionalisation step was performed at a lower temperature than was recommend in literature. Because the column was an agarose hydrogel, functionalisation was performed at 30 °C rather than 60 °C as per the literature [71] in order to prevent the agarose hydrogel to melt at the higher temperature. However, it is generally noted in commercial resins that weak anion exchange resins have a higher ion exchange capacity than weak cation exchange resins.

In comparison with commercially available ion exchange resins (capacities given in Table 4-4 below), the ion exchange capacities of the TPMS columns were significantly lower, even falling outside the lower range of these ion exchange capacities. The lower limit on CM-Sepharose Fast Flow was 90 μeQ/mL, and the highest ion exchange capacity for the agarose TPMS columns was 65.1 ± 1.6 μeQ/mL, demonstrating significantly lower ion exchange capacity. This was not an unexpected result, as the specific surface area of the beads was significantly higher than the specific surface area of the TPMS columns, meaning the beads had a higher ligand density than the TPMS columns, hence a higher ion exchange capacity.

*Table 4-4: Ion exchange capacities of commercial resins (data from manufacturers)*

| Resin | Ion Exchange Capacity | |
|---|---|---|
| | Lower Limit (μeQ/mL) | Upper Limit (μeQ/mL) |
| CM-Sepharose Fast Flow [2] | 90 | 130 |
| CM-Cellufine C-500 [105] | 70 | 140 |
| DEAE-Sepharose Fast Flow [106] | 110 | 160 |
| DEAE-Sepharose CL-6B [107] | 130 | 170 |

CM-Cellufine C-500 has a higher maximum ion exchange capacity than CM-Sepharose Fast Flow, demonstrating the same trend as the TPMS columns where the cellulose columns had a higher ion exchange capacity compared with the agarose columns with the same channel diameter. Studies have shown that the pore diameter of cellulose beads is smaller than that of agarose (approximately 10 μm compared with 20 μm) [108], meaning that the specific surface area for the material itself is higher than agarose, which was also discussed by Johnson [108]. The actual porosity of the agarose and cellulose TPMS columns is investigated later, and likely contributes to the differences in the ion exchange capacities of the columns.

### 4.4.2 Protein Equilibrium Binding Capacity

The equilibrium binding capacity was determined for each ligand immobilised to agarose as well as cellulose functionalised for cation exchange chromatography. The protein used to bind to the weak cation exchanger was cytochrome c from bovine heart, bovine serum albumin (BSA) was used on the DEAE column (anion exchange), and α-lactalbumin was used on the HIC column (HIC). The data points show each isotherm approaching equilibrium, hence the Langmuir adsorption isotherm was assumed fitted to each dataset (Figure 4-10). This assumed monolayer coverage of binding sites, which is reasonable given the large size of the proteins unlikely to allow more than a single adsorption layer as charge effects cannot propagate through. Langmuir isotherms were fit to each data set using the least squares method, and Langmuir parameters determined using this method are given in Table 4-5.

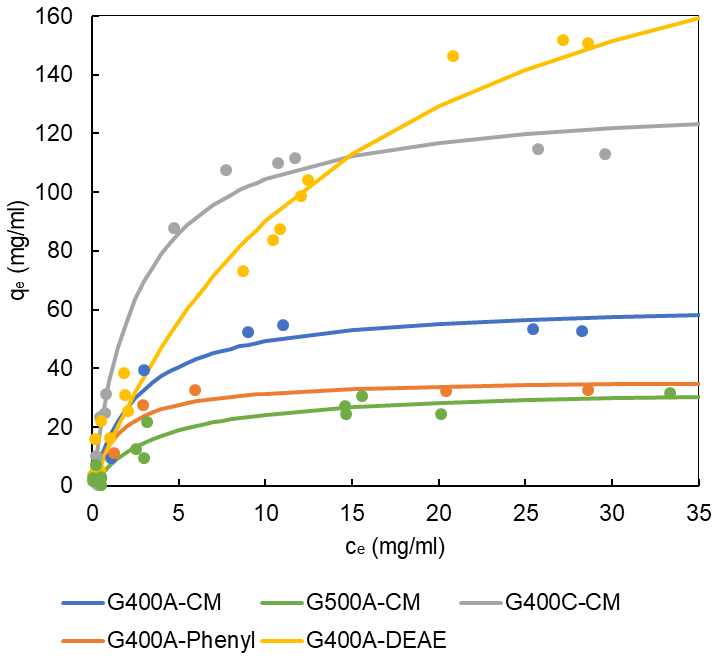


*Figure 4-10: Adsorption isotherms TPMS hydrogel columns with Langmuir model fitted*

*Table 4-5: Langmuir parameters determined using least squares method*

| | $q_e$ | $K$ |
|---|---|---|
| | mg/ml | ml/mg |
| G400A-CM | 62.8 | 0.364 |
| G500A-CM | 33.6 | 0.259 |
| G400C-CM | 132.8 | 0.367 |
| G400A-DEAE | 229.7 | 0.064 |
| G400A-HIC | 36.4 | 0.626 |

Most notable in these results was the high binding capacity of G400C-CM compared with G400A-CM. The equilibrium binding capacity was 132.8 mg/ml for the cellulose cation exchanger, and 62.8 mg/ml for the agarose cation exchanger of the same geometry. The higher binding capacity of cellulose compared with agarose was mimicked by Levison et al who found CM Cellufine C-500 had a lysozyme binding capacity of 151 mg/ml, and CM Sepharose FF had a lysozyme binding capacity of 106 mg/ml [109]. Cellulose has a higher porosity than agarose, yielding a greater surface area to volume ratio, hence higher immobilised ligand density and binding capacity.

The equilibrium constants calculated for the CM columns indicate a relatively low affinity for the protein to the CM ligands immobilised to the hydrogel columns. In the buffering conditions and pH, a high protein concentration is required in the liquid for there to be a high concentration in the adsorbed phase and hence high protein adsorption. Buffer salt concentration was 20 mM, and pH was 7.0, meaning the ionic strength of the buffer was not too high such that protein binding was not favoured, and there was sufficient charge difference between the buffer and the protein isoelectric point (pI) (approximately 9.6). 6-aminohexanoic acid selected as a CM ligand is a weak acid and is usually used as a spacer arm for chromatography resins rather than a dedicated ion exchange ligand.

Commercial resins DEAE-Sepharose Fast Flow and DEAE-Sepharose CL6B are reported to have binding capacities for HSA of 110 mg/ml and 170 mg/ml respectively [106, 107], which is contrasted by data from Levison who tested BSA binding to the same agarose resins and obtained binding capacities of 48 mg/ml and 78 mg/ml and the binding respectively [109]. The binding capacity of BSA to the agarose TPMS columns was 229.7 mg/ml from the Langmuir analysis, higher than those stated by manufacturers of DEAE beads, and those tested by Levison. This result is in accordance with the high ion exchange capacity that was observed for the same column. This show perhaps good potential for the DEAE column to be used as a 3D printed chromatography matrix. However, for the majority of this research, CM columns are the focus. These results show the versatility and possibility for this type of column with a high binding capacity to be further developed.

Lastly, the hydrophobic interaction chromatography agarose column demonstrated competitive protein binding using hydrophobic interactions compared with commercially available resins. Phenyl-agarose beads have binding capacities ranging from 20-40 mg/ml depending on the ligand density and protein used as analyte [110, 111]. Commercial HIC resins often have degree of ligand substitution specified (low or high substitution) meaning the ligand density is strongly controlled, which could be an avenue to pursue in future developments with hydrophobic TPMS columns. In preliminary development of the HIC column, ligand substitution was too high resulting in a column which shrunk rather than swelled in aqueous solutions because the water-repelling ability of the ligand was greater than the water-absorbing ability of the agarose. Clearly the is an optimum ligand density that results in high hydrophobic protein binding without the column becoming too hydrophobic.

The ion exchange capacity of each resin was used to calculate the maximum binding capacity of capacity of the proteins used in the binding experiments above, assuming 1:1 binding of protein to ligand, called $q_0$. Comparison between $q_0$ and $q_m$ from Langmuir analysis showed a large discrepancy because of steric and charge effects of proteins (Table 4-6) [52]. On the CM column, steric hindrance and effective charge should be the same because the protein-ligand interaction is the same, and buffering conditions were the same. Curve fitting of a steric mass action (SMA) model did not yield a good fit to the experimental data for typical effective charge or steric hindrance parameters, therefore these results were not presented. Future experiments measuring the variation in binding capacity at different mobile phase salt concentrations would ensure these parameters could be determined. However, the SMA model does not take into account exclusion of proteins from pores on a size basis, and as the pore characteristics of these hydrogels was unknown, is a likely reason for the model to not accurately describe the data. Likewise, the interaction between ligand density and steric parameters were not understood; these could also account for these differences.

*Table 4-6: Experimental equilibrium binding capacity ($q_e$) and maximum binding capacity ($q_0$) of proteins to columns*

| | $q_e$ mg/mL | $q_0$ mg/mL | $z+\sigma$ - |
|---|---|---|---|
| G400A-CM | 62.8 | 607.2 | 9.7 |
| G500A-CM | 33.6 | 438.9 | 13.1 |
| G400-C-CM | 132.8 | 972.5 | 7.3 |
| G400A-DEAE | 229.7 | 5327.4 | 23.2 |

## 4.5 Conclusions

In this chapter, the successful creation of TPMS hydrogels for chromatography was demonstrated. Gyroid and Schwarz diamond columns were made from agarose and cellulose hydrogels, and good fidelity between the TPMS design and actual structures was observed. Channel features down to 300 μm were produced, which are on a similar scale to beaded resins using in PBC. However, the negative templating method resulted in a few column defects observed: SEM images showed a layering effect present on the columns, thought to have propagated through to the hydrogel structure from the 3D-printed template. ISEC experiments showed that in some cases, the TPMS channel structure may not have been uniform inside the hydrogel columns produced, as interstitial void fraction measurements did

not equal the interstitial void fraction design. These issues associated with the negative templating technique are not anticipated to be a problem for hydrogels 3D-printed directly, as developments in this area are becoming more and more available.

The TPMS hydrogel structures were successfully functionalised for cation exchange, anion exchange, and hydrophobic interaction chromatography. Ion exchange capacity of small ions showed ligand density increased with decreasing channel diameter, because the surface area of the columns increased with decreasing surface area. Cellulose hydrogels were measured to have a higher adsorption capacity than their agarose counterparts, because of the higher surface area attributed to the cellulose pore structure, and the use of added cellulose as a physical crosslinker providing more polysaccharide to have cation exchange ligands immobilised to. Protein adsorption experiments showed Langmuir adsorption behaviour, however the ligands selected had poor affinity to the proteins selected for adsorption, despite an overall competitive protein binding capacity compared with pack-bed chromatography resins. The theoretical maximum protein adsorption on the hydrogels calculated based on the small-ion capacity results did not correlate to the protein adsorption capacities measured experimentally, indicating steric and charge hindrance of the binding sites from large proteins. However, steric mass action law models could not be used to describe this behaviour. It was likely the unknown pore size and distribution of the columns mean that proteins were excluded from some of the pore structures.

All in all, this chapter has shown a world first technique: the creation of controlled geometry chromatography structures, made using 3D-printing techniques. The application for columns made in the chapter to be patented was filed in 2016 [50], demonstrating this was a world-first achievement. Different TPMS geometries and feature sizes made from commonly used chromatography stationary phase material (agarose and cellulose), functionalised for common types of chromatography show the potential for this technique to be employed in process chromatography.

# Chapter 5. Dynamic Characterisation of Protein Adsorption to TPMS Hydrogel Columns and Functionalisation Limitations

## 5.1 Introduction

In Chapter 4, TPMS hydrogels were shown to have been successfully made into the controlled geometry structure and functionalised for different modes of chromatography. The adsorption performance was analysed under static conditions, giving the maximum binding capacity of model proteins to the columns. As chromatography is a dynamic process, the adsorption performance of the columns under flow is important to characterise because mass transfer effects can limit protein capture efficiency. In this chapter, protein adsorption to the columns is characterised under dynamic conditions. Protein bind-and-elute experiments demonstrate the columns' ability to adsorb protein from an injected mobile phase, then elute the adsorbed protein when an elution buffer is applied. From these elution peaks, the reduced plate height is calculated, showing the columns' efficiencies compared with other chromatography media. Breakthrough curves show the mass transfer limitations apparent on the columns, which is supported by dynamic binding capacity data at 10% protein breakthrough. These results show that there is a flowrate and channel diameter limitation on the columns' protein adsorption abilities. Potential sources of this limitation are discussed and investigated, such as the functionalisation step limiting the amount of protein binding, and the hydrogel pore structure being unpredictable and changing with functionalisation.

## 5.2 Protein Bind-and-elute

Protein bind-and-elute experiments were conducted on each column to prove successful protein capture and elution for different TPMS geometries (gyroid and Schwarz diamond), hydrogel materials (agarose and cellulose), and chromatographic functionalities (CM, DEAE, and HIC). These columns were made using the negative templating method and functionalised using batch functionalisation methods. Bind-and-elute experiments were run as described in Section 3.10.1.

### 5.2.1 Agarose Gyroids

2 mL samples of 2 mg/mL cytochrome-c in 20 mM sodium phosphate buffer at pH 7.0 were loaded onto the agarose gyroid columns at 1 mL/min, and then eluted with 1 M NaCl in 20 mM sodium phosphate, pH 7.0. The chromatograms below (Figure 5-1) show some unbound cytochrome-c flowing through each column at the beginning of each run, then protein eluting upon the addition of the salt buffer, confirming successful ion exchange. This proves the capability of the column as a cation exchanger, as in the neutral buffer solution, cytochrome-c (pI 9.5 – 10.5) is positively charged, meaning that it will bind to the negatively charged cation exchange ligands coupled to the agarose matrix. The magnitude of the peaks varies for each column: the unbound cytochrome-c peak increases with increasing channel diameter, while the elution peak decreases with increasing channel diameter. This means that the amount of cytochrome-c adsorbed to the columns increased with decreasing channel diameter, because the surface area of columns with smaller diameter channels was higher. A higher surface area means a higher ligand density, hence the increase in protein binding capability.

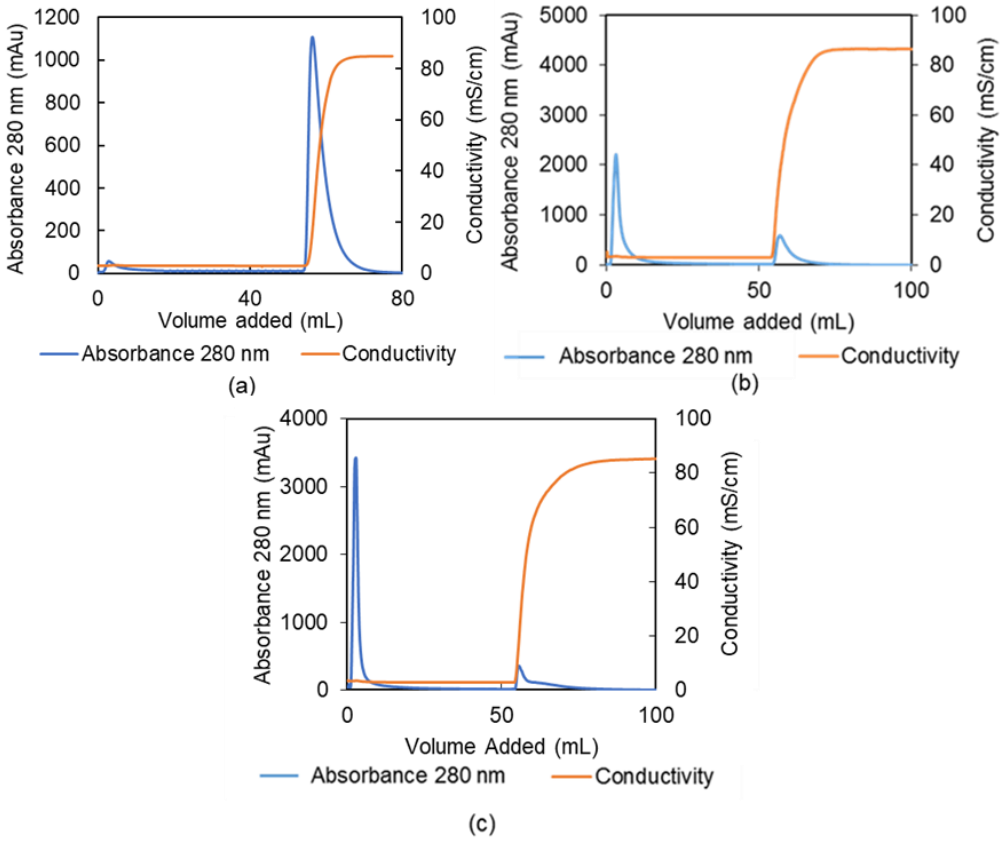


*Figure 5-1: Protein proof-of-concept chromatograms for (a) G300A-CM, (b) G400A-CM, (c) G500A-CM*

By integrating the area under each peak in the chromatograms, the cytochrome-c bound from the initial sample was calculated, proving binding decreased with increasing gyroid channel diameter (Table 5-1). The highest protein binding percentage was on G300A-CM, where 95.1% of the initial sample was bound and eluted from the ion exchange column. With increasing channel diameter, protein bound in the on-sample decreased: 31.4% was bound to the 400 μm gyroid, and 22.0% to the 500 μm gyroid column. This was expected because despite each column having the same volume, the specific surface area of the 300 μm column was higher; hence there was a higher ligand density. This result shows the G300A-CM provides close to maximum protein capture at 1.0 mL/min, meaning this is a promising sized column for protein capture in process chromatography. On the other hand, at 1.0 mL/min G400A-CM and G500A-CM bound less than 50% of the protein loaded on to the column, meaning neither of these columns provide good protein capture capability for process chromatography.

*Table 5-1: Protein bound on agarose gyroid columns from 2 mL, 2.0 mg/mL cytochrome-c*

| Column | Protein Adsorbed (%w/w) |
|---|---|
| G300A-CM | 95.1% |
| G400A-CM | 31.4% |
| G500A-CM | 22.0% |

As the channel diameter increased, it was likely that most of the cytochrome-c was carried out of the column via advection without diffusing through the pores and adsorbing. This is an early indication that the TPMS columns do not overcome the mass transfer limitations associated with PBC, and perhaps are not suitable as an alternative if operated in a conventional bind-and-elute chromatography process.

Other notable observations in these experiments were the asymmetry of the flow-through and elution peaks; each peak has a sharp rise in absorbance initially, followed by a long tail once the maximum is reached. This indicates the pore diffusion limitation present on the columns as it takes a long time for protein to completely diffuse out of the pores in comparison with fast advection [52]. This is supported by the protein capture results in Table 5-1, where protein recovery was lower for larger diameter channels. Carta and Jungbauer also state that at higher flowrates, peaks become more asymmetric as diffusion is much slower in comparison with the convective mass transport. In order to analyse if this statement applied to the TPMS columns, bind-and-elute experiments were repeated on the agarose gyroid CM columns at

three different flowrates: 0.25 ml/min, 1.0 ml/min, and 2.0 ml/min. The chromatograms are shown below (Figure 5-2), where 2.0 ml of 2.0 mg/ml cytochrome c was loaded onto the column in 20 mM sodium phosphate buffer, pH 7.0, and eluted in the same buffer with 1.0 M NaCl.

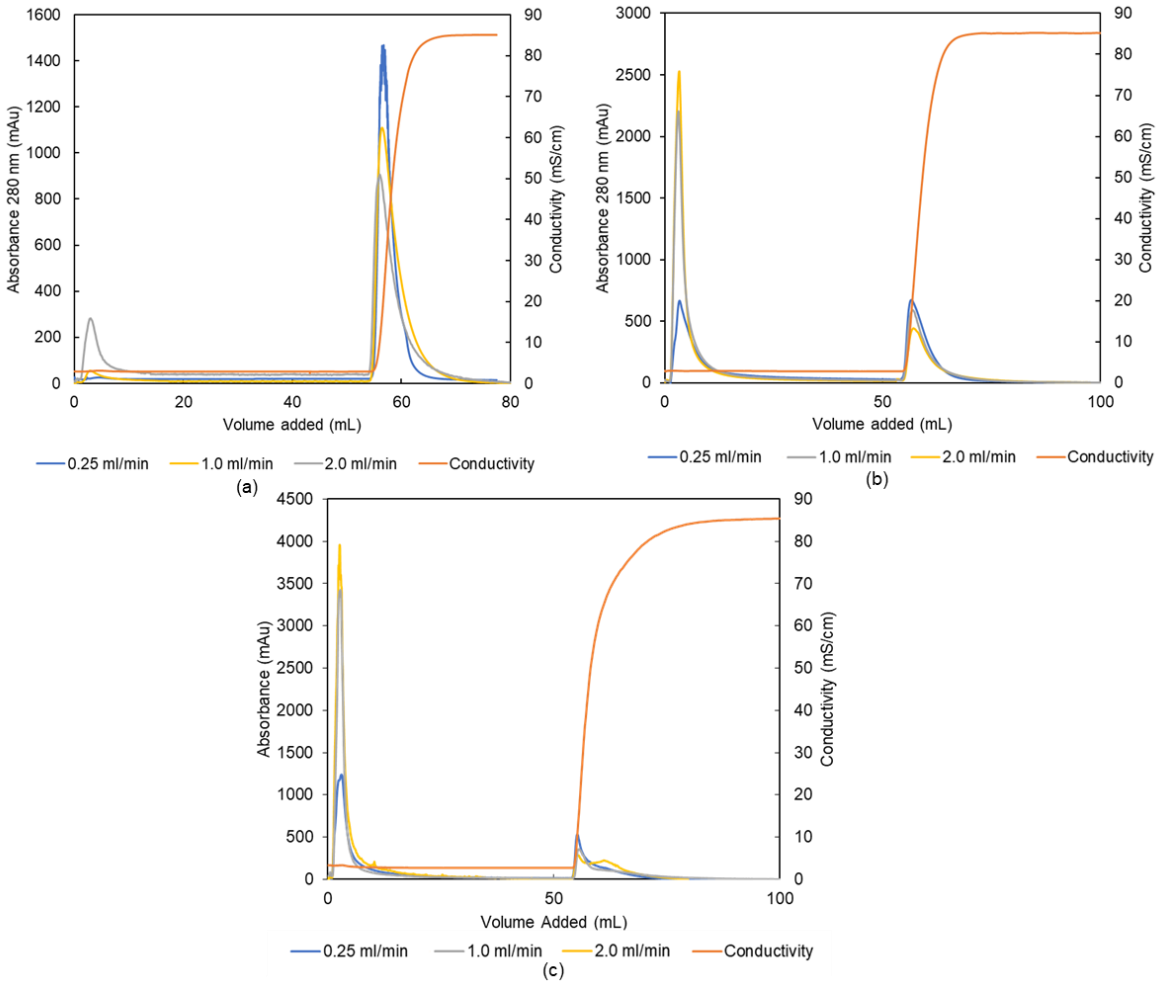


*Figure 5-2: Chromatograms demonstrating flowrate dependence of protein capture on (a) G300A-CM, (b) G400A-CM and (c) G500A-CM*

For each column, the amount of unbound cytochrome-c increased with increasing flowrate, and the amount of cytochrome-c adsorbed to the column decreased with increasing flowrate. The amount of protein adsorbed to the columns as a percentage of the total sample loaded on to the columns is show in Table 5-2 below. G300A-CM had the highest amount of protein bound at all flowrates, and nearly all the cytochrome-c adsorbed to the column at 0.25 ml/min. This is because the flowrate was slow enough for protein to diffuse into the pores and adsorb, rather than being entrained out of the column at higher flowrates. Even at

higher flowrates, G300A-CM maintained a high protein capture compared with the agarose gyroids with larger channel diameters.

*Table 5-2: Protein bound on agarose gyroid columns from 2 mL, 2.0 mg/mL cytochrome-c at different flowrates*

| | **Protein Adsorbed (%w/w)** | | |
|---|---|---|---|
| **Column** | 0.25 ml/min | 1.0 ml/min | 2.0 ml/min |
| G300A-CM | 99.0% | 95.1% | 83.9% |
| G400A-CM | 52.2% | 31.4% | 28.4% |
| G500A-CM | 30.5% | 22.0% | 20.9% |

Across all the chromatograms presented, elution of the protein was observed almost immediately upon the addition of salt into the column. Adsorption experiments in the previous chapter foreshadowed this; whereby the equilibrium constants determined in Langmuir analyses were low, indicating low affinity of cytochrome c to the CM ligand. This showed that cytochrome c was weakly bound to the CM ligand. 6-amino hexanoic acid is not commonly used as a CM ligand, rather it is used as a spacer between the stationary phase matrix and ligand. Other ligands could be considered to overcome this.

Linear velocities (sometimes referred to as superficial velocity) for each flowrate were calculated and shown in Table 5-3 below. Linear velocities can be a more meaningful way of expressing operating rates for process chromatography because adsorption and mass transfer parameters are dependent on velocities, and it is easier to find how long a chromatography run will take based on column length. The velocities tested in these columns are very low in the context of typical preparative process chromatography; the lowest velocities for chromatography start at approximately 75 cm/h, and are operated at an average of 450-600 cm/h [15]. The implications of this on the TPMS hydrogel columns tested in this research is that the best protein capture was achieved at the lowest velocity which is an impractical velocity at which to operate commercial chromatographic processes. Chromatography columns range from a few centimetres in length for some lab scale applications, to 1-2 m long for columns implemented in large scale processes. This means chromatography runs would have to be extremely long to achieve a competitive protein capture on the columns.

*Table 5-3: Linear velocities and Reynolds number for 10 mm diameter TPMS hydrogel columns*

| Volumetric flowrate | Linear velocity | Reynolds Number | | |
|---|---|---|---|---|
| | | G300A-CM | G400A-CM | G500A-CM |
| mL/min | cm/h | (-) | (-) | (-) |
| 0.25 | 19.1 | 0.016 | 0.021 | 0.026 |
| 1 | 76.4 | 0.064 | 0.085 | 0.106 |
| 2 | 152.8 | 0.127 | 0.169 | 0.212 |

Reynolds numbers give a little more insight, despite interstitial velocities being very similar for each column, these increase with flowrate and channel diameter. Each of these show the columns in the laminar flow regime. However it has been noted that gyroids can generate local turbulence [96] which could complicate the understanding.

#### 5.2.1.1 Reduced Plate Height

Reduced plate height was determined and plotted against the dispersion number and Peclet number for each elution peak from the bind-and-elute experiments (Figure 5-3). Because affinity of cytochrome c to the CM ligand was low, desorption of cytochrome c from the ion exchange ligand was fast, and did not influence the shape of the elution peaks. The long tail in the elution peaks indicates both a diffusion limitation and axial dispersion limitation, and the effect of these is broken down in Figure 5-3 below. Large dispersion numbers were observed at higher flowrates and increased with increasing channel diameter. At higher dispersion numbers, higher reduced plate heights were calculated, meaning dispersion resulted in poorer chromatographic efficiency. The Peclet numbers calculated were large due to the small molecular diffusion coefficient for cytochrome c, showing the columns to be in the mass transfer limiting zone on a typical van Deemter curve, rather than in the axial dispersion limited zone.

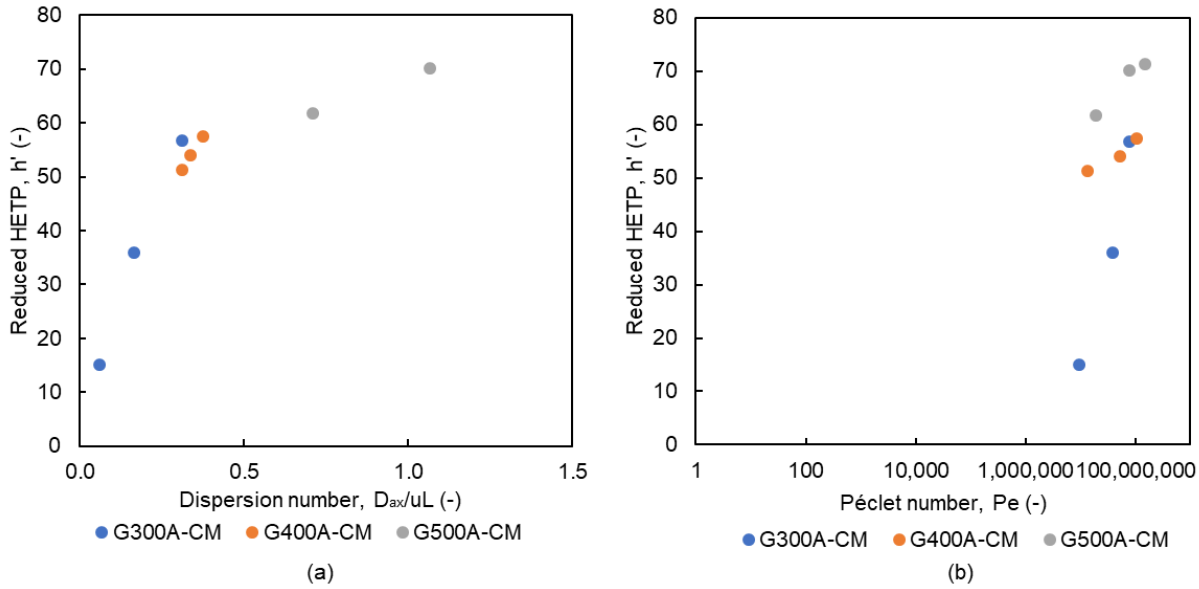


*Figure 5-3: Reduced plate height against (a) dispersion number; and (b) Peclet number*

Simulations predicting reduced plate height for gyroids of 0.5 voidage did not take into account the porosity of the columns producing a single curve for reduced plate height against Peclet number [85], while in Figure 5-3 each channel diameter gyroid had a different plate height for similar Peclet numbers. This is because the advective mass transfer rates were lower on columns with smaller channel diameter, which was not taken into account in the simulations, and also accounted for the reduced plate heights determined experimentally being significantly higher than those determine in the simulations. For these columns to operate at the minimum reduced plate height identified by van Deemter curves, the flowrate required is significantly lower than those tested; as the lowest flowrate tested was 0.25 mL/min, operating lower than this would result in extremely long processing times.

The dispersion number was divided by the Peclet number to give the relative effect of axial dispersion and molecular diffusion. These ratios yielding low values prove that diffusion dominated dispersion, however the relative effects of dispersion did vary with Reynolds number and in columns with different diameter channels. The effect of dispersion was higher relative to diffusion at low Reynolds numbers and more apparent on columns with greater diameter channels. On G300A-CM, the ratio was relatively constant with Reynolds number indicating dispersion effects were at their maximum, and diffusion was dominating. In G400A-CM and G500A-CM, this point was not reached at the flow rates tested; instead, a decreasing trend in the ratio was observed with increasing Reynolds number, showing dispersive effects reducing in magnitude compared with diffusion. Overall, these results show

that slow diffusion of cytochrome c was mainly responsible for high reduced plate height values rather than axial dispersion. This is supported by the general thesis that at higher Reynolds numbers, axial dispersion is reduced [112].

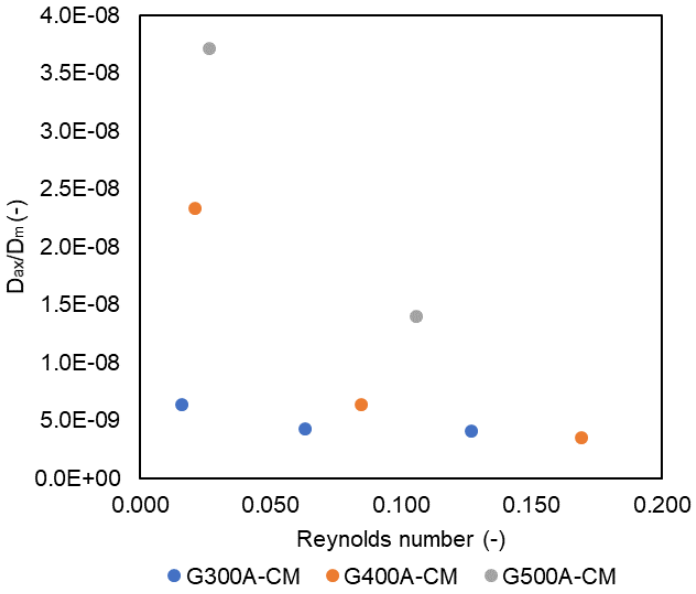


*Figure 5-4: Relative magnitude of axial dispersion and molecular diffusion at various Reynolds numbers*

The diameter and length of the TPMS columns tested in this research were not designed for optimum chromatographic efficiency; rather, the computational and technical limitations of the CAD and 3D-printing software and hardware determined the design constraints, with this research serving as proof the columns can be produced for solid-tolerant chromatography, and identifying areas for improvement and optimisation. Reduced plate height can be decreased with an increase in column diameter, as dispersive and wall effects are minimised [113]. As was concluded in Chapter 4, developments in 3D-printing and associated technologies will mean geometries that optimise plate height can be designed and printed for more efficient chromatographic performance.

### 5.2.2 Other Columns

Subsequent TPMS hydrogel columns made using the 3D-printing method also demonstrated successful protein adsorption. These chromatograms are shown in Figure 5-5. Successful protein binding was achieved on an agarose SD500A-CM, G400C-CM, G400A-DEAE, and G400A-HIC. Each run shown in Figure 5-5 was conducted at 1.0 ml/min (76.2 cm/h).

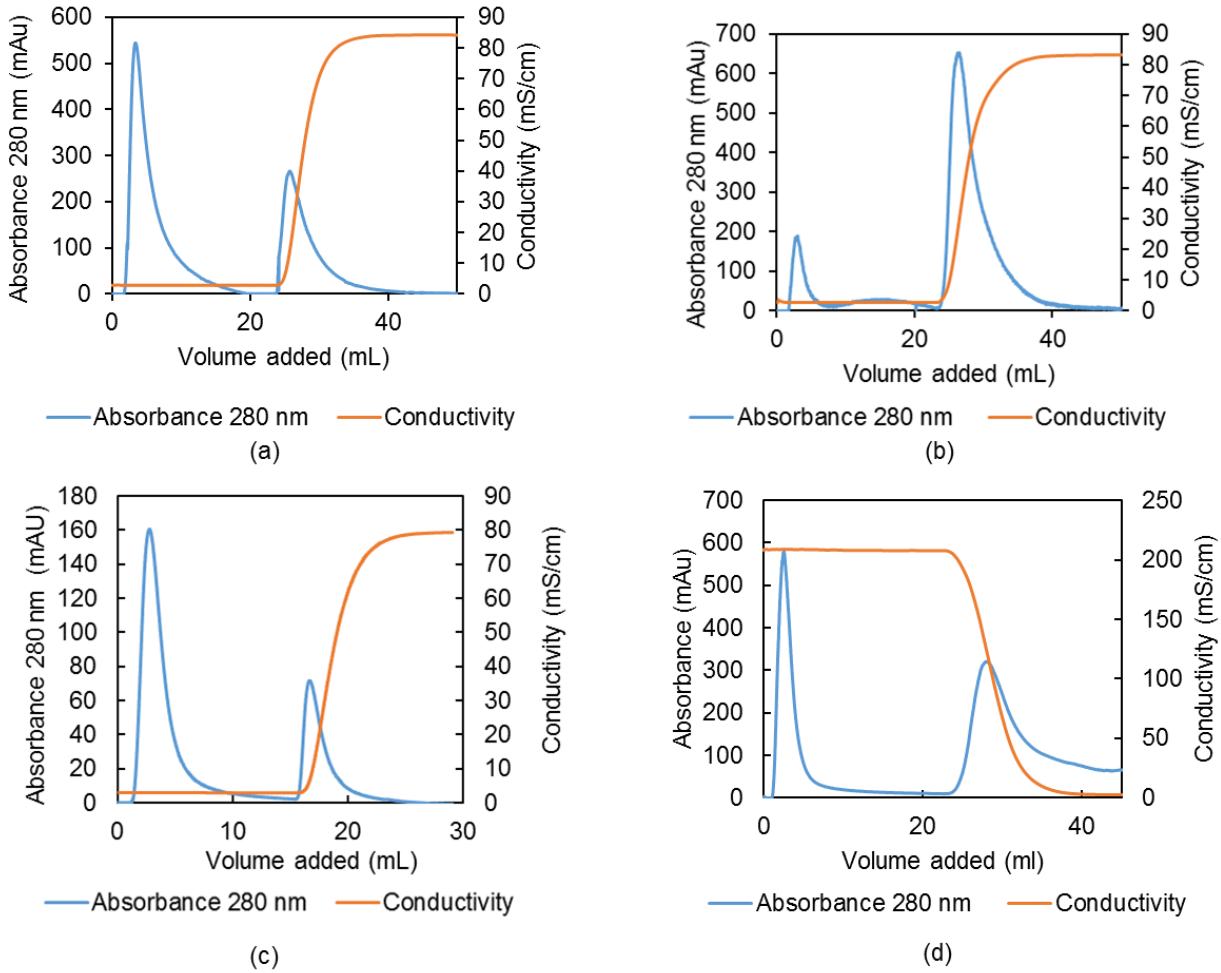


*Figure 5-5: Bind and elute proof-of-concept experiments for (a) SD500A-CM, (b) G400C-CM, (c) G400A-DEAE, (d) G400A-HIC*

For SD500A-CM monitoring the UV absorbance at 280 nm over the course of the run (Figure 5-5 (a)) showed that 37.5% of cytochrome-c loaded on to the column was bound and subsequently eluted with the addition of salt elution buffer. In comparison with G500A-CM in the previous section, protein capture was much greater on the Schwarz diamond; it was closer to that of G400A-CM. The Schwarz diamond structure has a higher specific surface area compared with the same diameter channel gyroid, meaning it will have a greater binding capacity which is reflected in this result.

Protein capture on G400C-CM was demonstrated on the chromatogram in Figure 5-5 (b). A small flow-through peak is observed compared with the elution peak, equating to a cytochrome-c capture of 89.2%. Compared with protein capture on the same geometry agarose column (G400A-CM), this amount was more than twice that of the agarose column, providing early evidence of the superior protein capture performance of the cellulose columns compared with agarose columns.

G400A-DEAE was successfully functionalised for anion exchange chromatography. In a neutral pH buffer, BSA was bound to the column and subsequently eluted using 1 M NaCl. The theoretical pI of BSA is 4.7, meaning in pH 7 it is negatively charged, hence its ability to bind to a DEAE ligand under these buffering conditions. Approximately 67.4% of BSA was bound to the column and subsequently eluted (Figure 5-5(c)). This amount was not large compared with what a commercial column would achieve (closer to 100% protein bound), especially given G400A-DEAE had the highest equilibrium binding capacity out of all the TPMS columns made. These results were likely due to the mass transfer limitations present on these columns, as previously discussed.

Protein capture on the benzylamine agarose hydrophobic matrix was demonstrated on the chromatogram (Figure 5-5 (d)), confirming its capability as a hydrophobic interaction chromatography column. The peaks at an absorbance of 280 nm show protein was eluted from the column as salt concentration decreased; in a low-salt buffer, the protein refolds and hydrophobic amino acid groups are no longer on the surface of the column, and the desorb from the hydrophobic ligand. The first peak between 1.5 – 10 mL buffer added is the flow-through of unbound α-lactalbumin. Once the buffers were changed and the conductivity decreased another peak was detected, thus proving successful protein capture at elution based on hydrophobicity. Analysis of the peak sizes showed that 65% of protein is captured and subsequently eluted with the elution buffer. Again, this is not high efficiency protein capture, but it does show the successful manufacture, functionalisation, and protein capture capability based on hydrophobic interactions of a TPMS hydrogel column.

The chromatograms in Figure 5-1 and Figure 5-5 all demonstrated a clear limitation in the TPMS columns: ideally there would be no flow-through peak as all protein would be captured then subsequently eluted upon buffer change, however this was not the case. Large flow-through peaks were observed, the larger of which were seen in TPMS structures with greater diameters and at higher mobile phase flowrates. Good protein capture was only achieved at low flowrates, meaning long operating times, in TPMS structures with smaller features would work in a practical protein adsorption applications.

## 5.3 Protein Breakthrough

A key indicator of chromatography column performance is the result of adsorption breakthrough studies as they provide inside to how well the columns perform at conditions closer to at which they are operated (ie under flow). Breakthrough studies were conducted

with a continuous 2.0 mg/ml protein on-sample loaded onto the columns and run until no change in outlet concentration (UV absorbance at 280 nm) was observed on the Unicorn software. Fractions were collected every five millilitres and analysed on the NanoDrop to measure protein concentration. Breakthrough curves were plotted and the area above the breakthrough curve calculated using the trapezium rule to find the amount of protein adsorbed to the column for each run.

Breakthrough curves are presented for the CM columns made in this research (previously outlined in Table 4-1). The effect of channel size, operating linear velocity, geometry, and hydrogel type were of interest to determine the best operating parameters for the TPMS hydrogel columns. The breakthrough curve gradient, saturation binding capacity (at 100% breakthrough) and dynamic binding capacities (at 10% breakthrough) are of interest here.

Breakthrough studies provide insight into column performance in processing systems but can also indicate kinetic and mass transfer limitations that may be occurring in the microscopic level. As was indicated in the bind-and-elute experiments, the large channel size of the TPMS columns and small pore diameter means pore diffusion limits the performance of larger channel columns given advective mass transport was faster than diffusion. Because of the diffusion limitation, breakthrough studies may show a critical operating linear velocity, where the fast advection process is balanced against slow diffusion.

The following discussion separates the breakthrough performance of agarose and cellulose columns for independent analysis, then finally all columns' results are analysed in conjunction with each other, along with the dynamic binding capacities.

### *5.3.1 Agarose Columns*

#### 5.3.1.1 Gyroids

Agarose gyroids were tested at three linear velocities: 19.1 cm $h^{-1}$, 76.4 cm $h^{-1}$, and 152.8 cm $h^{-1}$. Breakthrough curves were plotted (Figure 5-6) as a function of column volumes of protein loaded onto the column.

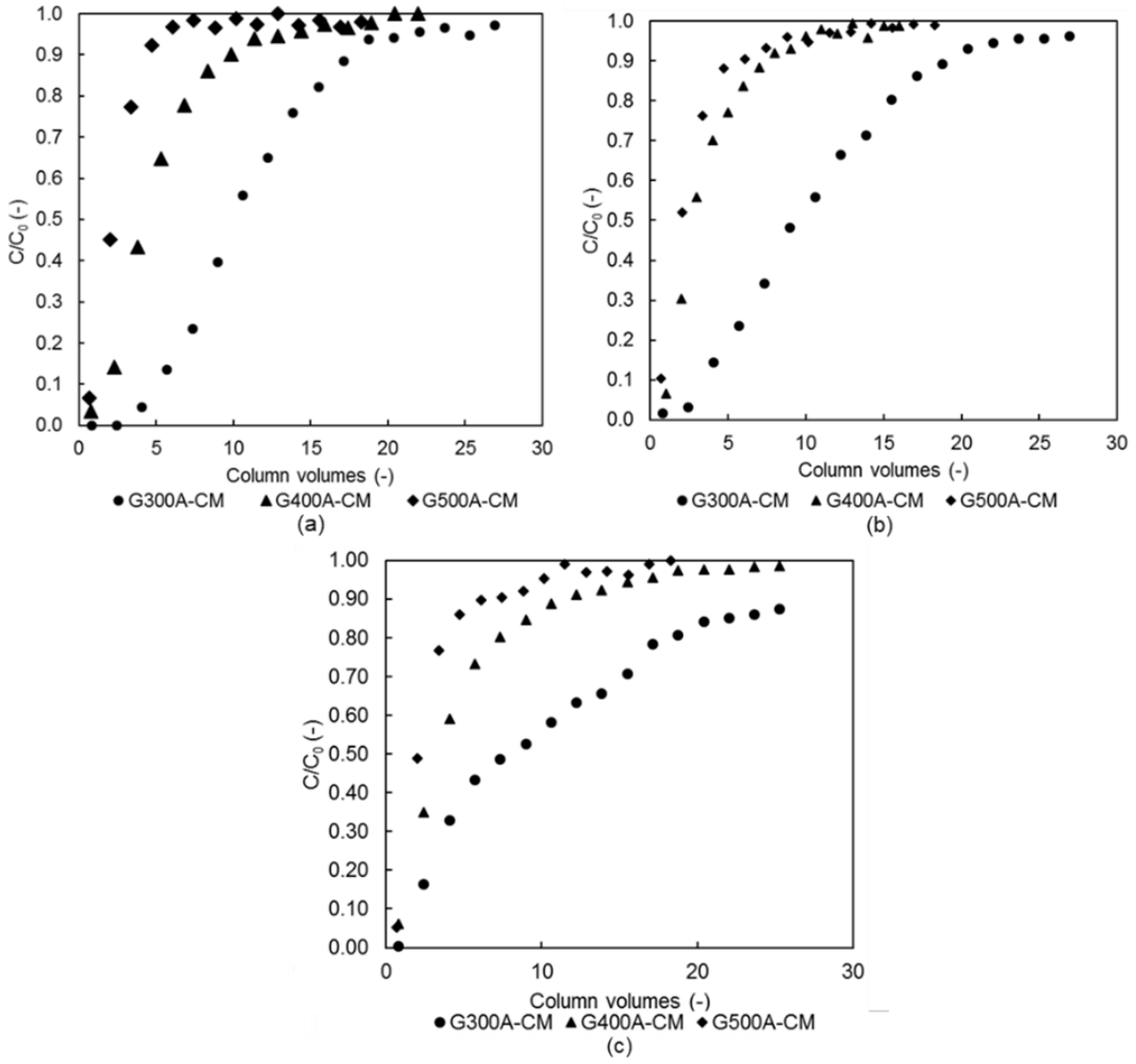


*Figure 5-6: Cytochrome c breakthrough on G300A-CM, G400A-CM and G500A-CM at (a) 19.1 cm $h^{-1}$, (b) 76.4 cm $h^{-1}$ and 152.8 cm $h^{-1}$*

For each agarose gyroid, cytochrome c breakthrough was most efficient at the lowest linear velocity tested (19.1 cm $h^{-1}$), which is evident in the breakthrough curves because the mass transfer zone was reached after more column volumes of protein were added to the column, meaning more protein was bound. G300A-CM had the best breakthrough performance at each velocity tested with saturation binding capacities (SBCs) shown in Table 5-4. These capacities were more than double those on G400A-CM and G500A-CM. As previously mentioned, this was because of the surface area of the columns increased with decreasing channel diameter, hence there was a higher ligand density with more sites available for protein adsorption.

In comparison with the equilibrium binding capacities (EBC) determined in the static adsorption experiments (Section 4.4.2), the SBC for G400A-CM and G500A-CM were both lower. Under dynamic conditions and with a lower on-sample concentration, the columns cannot attain the equilibrium binding conditions [52].

*Table 5-4: Saturation binding capacities for agarose gyroids at different linear velocities. SBC determined by integrating the area above the breakthrough curve*

| **Column ID** | **Linear Velocity** cm $h^{-1}$ | **SBC** mg/ml |
|---|---|---|
| G300A-CM | 19.1 | 22.1 |
| | 76.4 | 21.2 |
| | 152.8 | 21.8 |
| G400A-CM | 19.1 | 10.5 |
| | 76.4 | 9.6 |
| | 152.8 | 9.4 |
| G500A-CM | 19.1 | 7.8 |
| | 76.4 | 6.3 |
| | 152.8 | 5.7 |

Despite the clear differences in breakthrough performance shown in the breakthrough curves from the curves, the actual SBCs showed an almost constant value on G300A-CM and G400A-CM over each linear velocity tested. Because of the higher surface areas of G300A-CM and G400A-CM, they were possibly not as limited by pore diffusion as G500A-CM. This indicates that G300A-CM could be operated at the highest flowrate without a loss in capacity, vastly improving processing times without losses in yield.

In both G400A-CM and G500A-CM at 76.4 cm $h^{-1}$ and 152.8 cm $h^{-1}$ the breakthrough performance was very similar. The columns reached the mass transfer zone almost as soon as protein solution was applied to the column, and 100% saturation was reached after approximately 15 column volumes and 12.5 column volumes for G400A-CM at the higher velocities and G500A-CM at the higher velocities respectively. The small effect of linear velocity on breakthrough shows that mass transport via advection dominated at higher linear velocities, while at 19.1 cm $h^{-1}$ there was enough time for cytochrome c to diffuse into the pores and adsorb, rather than being entrained out of the column as was the case at higher velocities. Mass transfer approaches a point where advection is so large that the influence of diffusion is negligible, as seen in the larger diameter channel columns.

### 5.3.1.2 Schwarz Diamond

Cytochrome c breakthrough performance on agarose Schwarz diamond columns demonstrated the same dependence on linear velocity and channel diameter as the agarose gyroid columns (Figure 5-7). The shape of the breakthrough curve of SD400A-CM at 19.1 cm $h^{-1}$ show excellent initial breakthrough with lots of protein binding initially, reaching the mass transfer zone after approximately 20 column volumes of protein loaded onto the column. With the increase in velocity, the mass transfer zone was reached significantly faster, with very little difference between 76.4 cm $h^{-1}$ and 152.8 cm $h^{-1}$, demontrating advection dominated at these flowrates.

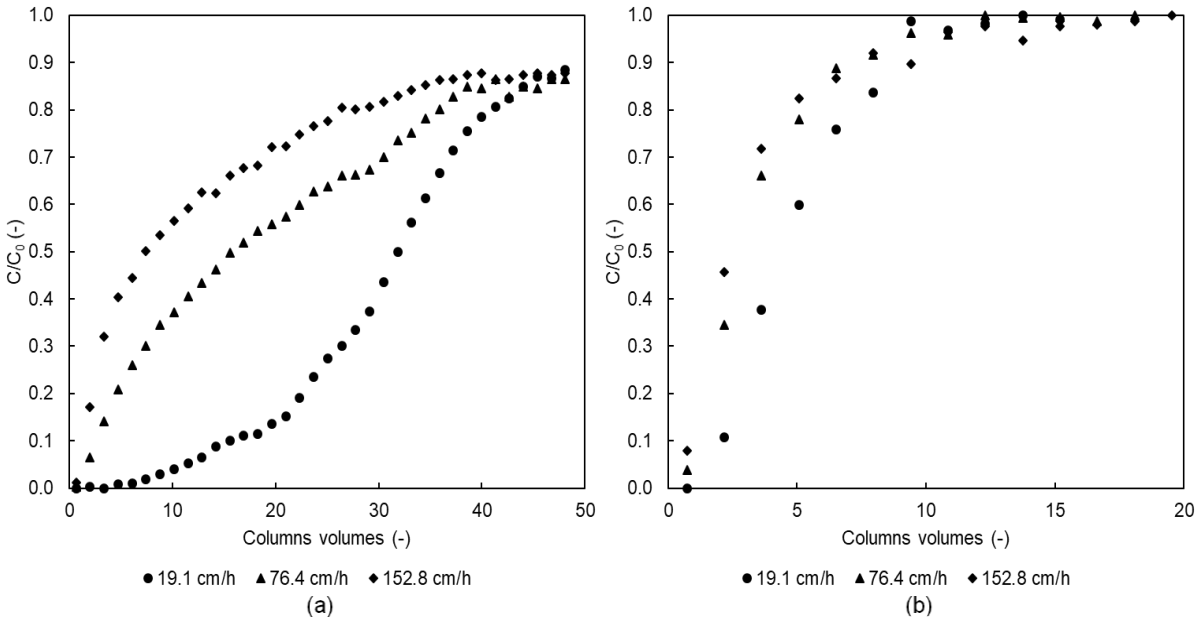


*Figure 5-7: Cytochrome c breakthrough at 19.1 cm $h^{-1}$, 76.4 cm $h^{-1}$ and 152.8 cm $h^{-1}$ on (a) SD400A CM and (b) SD 500 A CM*

A key observation from Schwarz diamond breakthrough curves was the significant difference between the performance of the SD400A-CM and SD500A-CM, where a significantly higher amount of protein was bound to the column in the former. SD400A-CM reached saturation after 45 column volumes of cytochrome c was loaded onto the column, while saturation was observed between 15-20 column volumes of cytochrome c loaded on to SD500A-CM. At 19.1 cm $h^{-1}$ the saturation binding capacities are were 65.6 mg/mL and 10.5 mg/mL for SD400A-CM and SD500A-CM respectively Table 5-5. This difference was not seen as distinctly between the different channel size agarose columns, and is not accounted for in the differences in the specific surface area of the columns. The reason for this was unclear.

*Table 5-5: Saturation binding capacities for SD agarose at different linear velocities.*

| Column ID | Linear Velocity cm $h^{-1}$ | SBC mg/mL |
|---|---|---|
| SD400A-CM | 19.1 | 65.6 |
| | 76.4 | 42.4 |
| | 152.8 | 30.9 |
| SD500A-CM | 19.1 | 9.8 |
| | 76.4 | 7.2 |
| | 152.8 | 7.0 |

#### 5.3.1.3 Agarose Combined Results

The specific surface area of a Schwarz diamond unit cell is greater than that of a gyroid of the same channel diameter, it thereby follows that the protein breakthrough was better on the Schwarz diamond columns. On SD500A-CM and G500A-CM the saturation binding capacities were 9.8 mg/mL and 7.8 mg/mL respectively at 19.1 cm $h^{-1}$; higher capacities were observed on SD500A-CM compared with G500A-CM for the higher linear velocities, too. Saturation binding capacity of SD500A-CM was closer to G400A-CM, the latter being 10.5 mg/mL at 19.1 cm $h^{-1}$.

For each type of hydrogel, it would be expected that the saturation binding capacity on a surface area basis would be constant at the same linear velocity, because ligand density and pore size distribution should be constant with surface area. When the saturation binding capacity was determined on a surface area basis, G400A-CM, G500A-CM and SD400A-CM had very similar values, averaging approximately 0.22 mg/$cm^2$, which showed there was a uniform ligand density and uniform pore size distribution and ligand density across these agarose gels, which was expected for agarose columns prepared using an identical method. Saturation binding on a surface area basis on G300A-CM was just under double that the Schwarz diamond but was also constant with linear velocity; on average 0.42 mg/$cm^2$. This value could be attributed for a more effective functionalisation method resulting in higher ligand density because of the high surface area of G300A-CM, although it wasn't expected to have such a high value compared with the other agarose gyroids. SD400A-CM also had a higher saturation binding capacity on a surface area basis, the maximum was 1.34 mg/$cm^2$. This reduced to 0.87 mg/$cm^2$ at 76.4 cm $h^{-1}$, and 0.63 mg/$cm^2$ at 152.8 cm $h^{-1}$. This indicates

that as the flowrate was increased, less of the column was penetrated by the protein loaded on to the column, which correlates to a pore diffusion limitation, because ion exchange groups immobilised to the hydrogel were in the pore structure. At least 50% of the available surface area SD400A-CM was in the microporous structure based on this correlation. Because this was not observed in all columns, this indicates either the pore size distribution was not constant across all gels, the functionalisation process did not result in uniform ligand immobilisation across the TPMS gels, and/or the pore size distribution changed once functionalised, and the amount of functionalisation/ligand density affected the degree of this change.

*Table 5-6: Saturation binding capacity on surface area basis for agarose TPMS columns*

| **Column ID** | **Linear velocity** cm $h^{-1}$ | **Saturation binding/surface area** mg/$cm^2$ |
|---|---|---|
| SD400A-CM | 19.1 | 1.34 |
| | 76.4 | 0.87 |
| | 152.8 | 0.63 |
| SD500A-CM | 19.1 | 0.25 |
| | 76.4 | 0.18 |
| | 152.8 | 0.18 |
| G300A-CM | 19.1 | 0.43 |
| | 76.4 | 0.41 |
| | 152.8 | 0.42 |
| G400A-CM | 19.1 | 0.24 |
| | 76.4 | 0.22 |
| | 152.8 | 0.22 |
| G500A-CM | 19.1 | 0.25 |
| | 76.4 | 0.20 |
| | 152.8 | 0.19 |

### 5.3.2 Cellulose Columns

Cytochrome c breakthrough experiments on the cellulose TPMS gyroid columns yielded significantly better column breakthrough performance compared with the agarose TPMS columns. At 19.1 cm $h^{-1}$, the column entered the mass transfer zone after approximately 25 column volumes of protein added, and good mass transfer was observed for the entire run. At 76.4 cm $h^{-1}$ and 152 cm $h^{-1}$ the initial gradient was very steep indicating slow mass transfer, but after approximately 10 column volumes the gradient reduced, indicating mass transfer

was faster. The gradient then gradually increased until it levelled off, but the concentration of the effluent did not reach that of the feed hence the column was not saturated, indicating ongoing pore diffusion and dilution effects. The shape of these two curves was unique, indicating a combination of mass transfer and axial dispersion limitations, but not to the same degree as the other columns operated at the same velocities. This initial rise in gradient of the breakthrough curve means the residence time of the protein was shorter than the mass transfer time required for proteins to get to binding sites. Cellulose hydrogels generally have a higher surface area than agarose because of its higher porosity, yielding a higher ligand density, hence more binding sites, and better adsorption (as observed with the ion exchange capacity and equilibrium binding capacity).

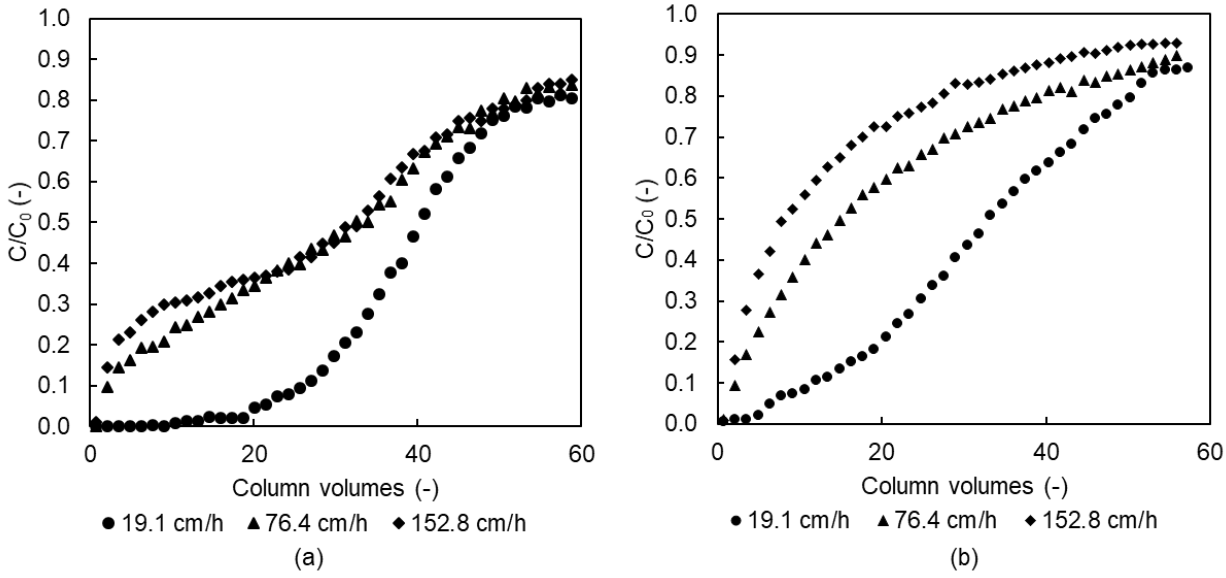


*Figure 5-8: Cytochrome c breakthrough at 19.1 cm $h^{-1}$, 76.4 cm $h^{-1}$ and 152.8 cm $h^{-1}$ on (a) G400C-CM; and (b) G500C-CM*

Saturation binding capacities are given in Table 5-7 and were the higher on the cellulose columns compared with that of their agarose counterparts, but again did not reach the equilibrium binding capacities of the column. For example, SBC on G400C-CM at 19.1 cm $h^{-1}$ was 84.5 mg/ml; the highest of all TPMS columns tested at approximately 70% of the equilibrium binding capacity. As with the agarose columns, SBC increased with decreasing channel diameter and decreased with increasing linear velocity. SBCs varied significantly with linear velocity, indicating that at the highest velocities tested the columns were not exhausted; rather pore diffusion was so slow that any changes in concentration due to adsorption were negligible as advection was the dominant form of mass transfer.

*Table 5-7: SBC of cytochrome c on G400C-CM and G500C-CM*

| **Column ID** | **Linear Velocity** cm $h^{-1}$ | **SBC** mg/ml |
|---|---|---|
| G400C-CM | 19.1 | 84.5 |
| | 76.4 | 63.0 |
| | 152.8 | 57.9 |
| G500C-CM | 19.1 | 66.2 |
| | 76.4 | 46.4 |
| | 152.8 | 38.1 |

Breakthrough experiments at a further three linear velocities were conducted on G400C-CM in order to determine the limit of the column until similar breakthrough performances to those of the agarose column was observed. Linear velocity was increased to 382 cm $h^{-1}$ (5.0 ml/min), 573.0 cm $h^{-1}$ (7.5 ml/min), and 763.9 cm $h^{-1}$ (10.0 ml/min), and all breakthrough curves for G400C-CM are plotted below (Figure 5-9). At these higher velocities, the breakthrough profile almost immediately reached the mass transfer zone, yielding significantly lower SBC than those determined at lower linear velocities on G400C-CM. At the two highest velocities, SBC was almost constant at 23.9 mg/ml (Table 5-8). This shows the column reached a limiting velocity where pore diffusion was almost obsolete, and SBC was independent of linear velocity.

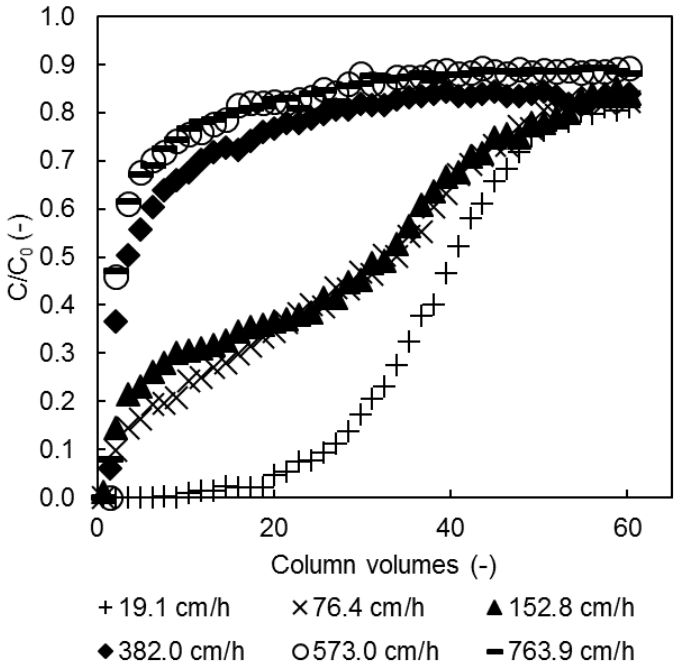


*Figure 5-9: Cytochrome c breakthrough on G400C-CM at 19.1 cm $h^{-1}$, 76.4 cm $h^{-1}$, 152.8 cm $h^{-1}$, 382.0 cm $h^{-1}$, 573.0 cm $h^{-1}$, and 763.9 cm $h^{-1}$*

*Table 5-8: SBC of cytochrome c on G400C-CM at all velocities*

| **Linear Velocity** cm $h^{-1}$ | **SBC** mg/ml |
|---|---|
| 19.1 | 84.5 |
| 76.4 | 63.0 |
| 152.8 | 57.9 |
| 382.0 | 31.0 |
| 573.0 | 23.8 |
| 763.9 | 23.9 |

### 5.3.3 Dynamic Binding Capacities

Dynamic binding capacities (DBCs) were calculated by integrating the area above the breakthrough curve until the eluent ratio was 10% of the protein loading concentration ($DBC_{10\%}$) and 50% of the protein loading concentration ($DBC_{50\%}$).

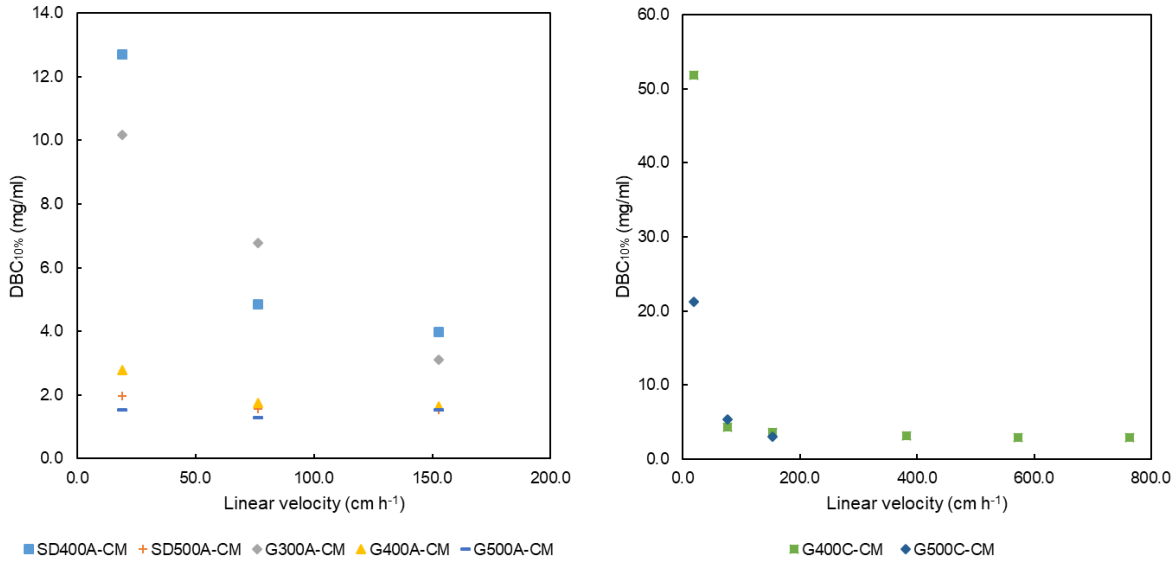


*Figure 5-10: Cytochrome c $DBC_{10\%}$ on (a) agarose TPMS columns and (b) cellulose TPMS column. Charts are separated to give better resolution to lower DBC values on agarose columns*

DBC was dependent on linear velocity, where as the linear velocity increased, the dynamic binding capacity decreased, demonstrating that dynamic binding capacity was limited by mass transfer, as with the saturation binding capacity. On agarose, the highest $DBC_{10\%}$ was 12.7 mg/ml on SD400A-CM followed by 10.2 mg/ml on G300A-CM. G400C-CM and G500C-CM had the highest $DBC_{10\%}$ of all columns, 52.0 mg/ml and 21.2 mg/ml respectively, which again decreased significantly as linear velocity increased and dominated prevailed as the controlling form of mass transfer. As with SBC, $DBC_{10\%}$ approached a point where it did not change with linear velocity, meaning pore diffusion was negligible, and most of the mass transport was through advection.

Compared with commercially available resins, $DBC_{10\%}$ were significantly lower on the TPMS hydrogel columns. Cellulose based resins made by Cellufine are reported to have dynamic binding capacities of 220 mg/ml and 130 mg/ml for lysozyme, significantly higher than 52.0 mg/ml for cytochrome c on G400C-CM. $DBC_{10\%}$ on G400C-CM was comparable to the $DBC_{10\%}$ of ribonuclease A to CM Sepharose Fast Flow [2], likely because of the high density of binding site on cellulose and greater surface area because of the microporous structure. The TPMS agarose columns had $DBC_{10\%}$ much lower than the Sepharose resins. On commercially available resins, $DBC_{10\%}$ experiments are generally performed at 300 cm $h^{-1}$; at

this linear velocity, $DBC_{10\%}$ of the TPMS columns is advection controlled, yielding the lowest DBCs.

*Table 5-9: $DBC_{10\%}$ of commercially available CM resins*

| Resin | Protein | $DBC_{10\%}$ (mg/ml) | Source |
|---|---|---|---|
| Cellufine Max CM | Lysozyme | 220 | [105] |
| Cellufine C-500 | Lysozyme | 130 | [19] |
| CM Sepharose Fast Flow | Ribonuclease A | 50 | [2] |
| CM Sepharose CL-6B | Ribonuclease A | 120 | [16] |

Dynamic binding capacity is often referred to as the "usable" part of the column and operating beyond this value results in inefficient use of time and materials because the eluent from the column contains a high amount of analyte. Based on the mass transfer limitations observed on these columns, $DBC_{10\%}$ was very low in comparison with commercially available resins. Hence dynamic binding capacity at 50% breakthrough ($DBC_{50\%}$) was calculated and plotted against linear velocity (Figure 5-11). Again, the highest values were at the lowest linear velocities for columns with smaller channel diameters.

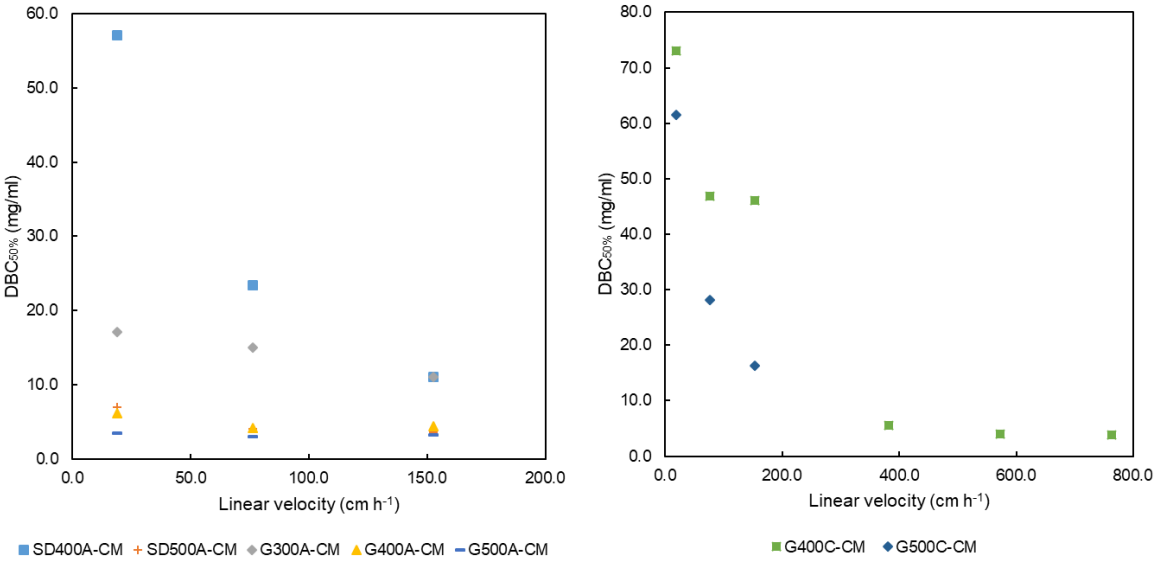


*Figure 5-11: Cytochrome c $DBC_{50\%}$ on (a) agarose TPMS columns and (b) cellulose TPMS column. Charts are separated to give better resolution to lower DBC values on agarose columns*

#### 5.3.3.1 Operating Time

TPMS hydrogel chromatography columns had the best protein breakthrough at lower linear velocities in columns with smaller diameter channels. The dynamic binding capacities showed the same trend, meaning it could be recommended to operate these columns at a very low linear velocity. On the opposite end of this spectrum however, it was often noted that there was a point where the protein binding capacity became independent to the linear velocity, meaning it may be more time-efficient to operate the columns at a higher velocity. Figures below shows the protein capture per minute, called the binding flux, in time taken to achieve 10% dynamic binding capacity (Figure 5-12 (a)) and 50% dynamic binding capacity (Figure 5-12 (b)) at the different linear velocities tested in the protein breakthrough experiments.

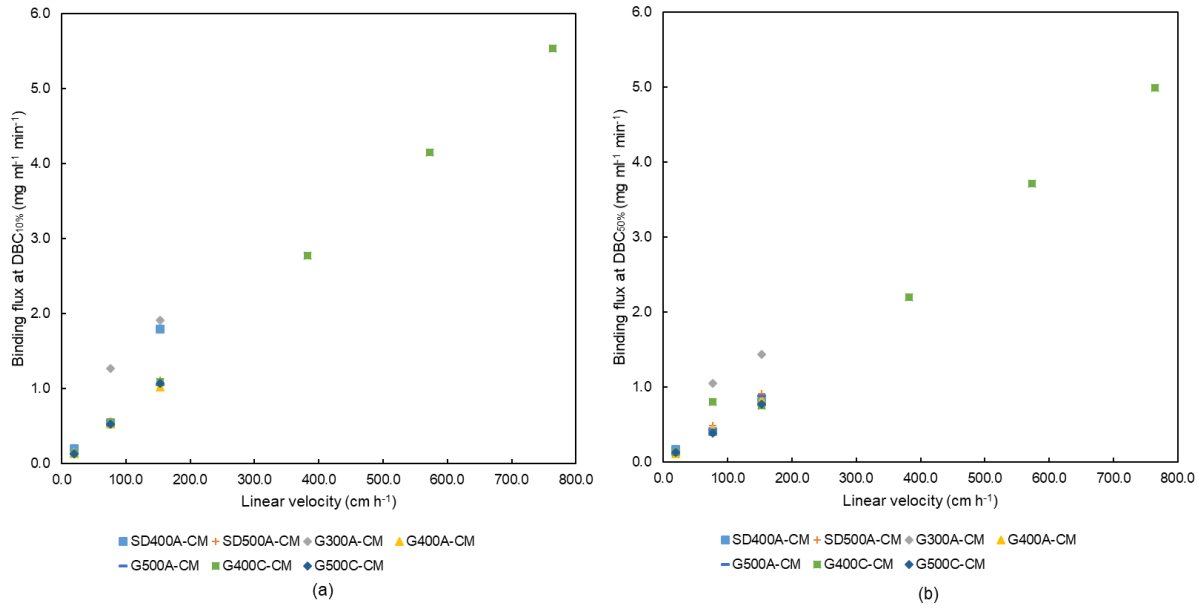


*Figure 5-12: Binding flux at (a) $DBC_{10\%}$ and (b) $DBC_{50\%}$ on all TPMS hydrogel columns*

When only considering the first three linear velocities tested (19.1 cm/h, 76.4 cm/h and 152.8 cm/h), G300A-CM and SD400A-CM had the highest protein binding flux, with just under 2.0 mg $ml^{-1}$ $min^{-1}$ when the linear velocity was 152.8 cm $h^{-1}$. In other words, G300A-CM and SD400A-CM operated with a mobile phase flowrate achieve faster protein capture up until 10% saturation of the columns, meaning it is more protein is adsorbed per unit time at these flow rate than at the lower flowrates, despite $DBC_{10\%}$ being significantly higher at lower flowrates. Based on trends for other columns, it was expected that increasing the operating velocities for these columns would not result in further reduction of $DBC_{10\%}$, so it could in fact be more efficient to operate these columns at an even higher linear velocity. The

only downside of this is that at higher linear velocity, the column uses more sample and buffer per minute. Determination of the optimum operating flowrate would have to consider operating costs and cost of consumables, as well as physical constraints such as pressure drop, as this increases with increasing flowrate, and high pressure drops can lead to column deformation and compaction. Further investigation into the optimisation is recommended for these parameters, to determine a flow rate that maximises protein adsorption, but minimises pumping and buffer costs, and minimises pressure drop.

Overall, binding flux was more efficient for 10% dynamic binding capacity compared with 50% dynamic binding capacity. The exception was G400C-CM at 76.4 cm $h^{-1}$ which was higher at $DBC_{50\%}$ due to nature of the mass transfer which appeared to favour diffusion at this point despite being advection controlled initially.

## 5.4 Functionalisation Limitations

Adsorption results thus far have shown successful protein adsorption to the TPMS hydrogels functionalised for various forms of chromatography; however, the functionalisation process had unknown effects on the on the porous microstructure of the hydrogels, and the overall effectiveness of the functionalisation methods were not considered in significant detail. In producing the TPMS CM columns, the agarose structures were activated and functionalised using a batch procedure, whereby the column was immersed in the reaction mixture in a centrifuge tube while the reaction progresses (for both activation and functionalisation). With activating agents and functionalisation reactants present in excess in solution, it was assumed that the functionalisation yields for the columns was at its maximum. However, the batch method and assumptions did not consider the mass transfer of products and reactants, or the possibility of reactants reacting with solution components rather than the hydrogel. For example, 6-aminohexanoic acid immobilisation to the active imidazole group on the hydrogel competed with the hydrolysis of the active imidazole group at pH 10, and the slow diffusion of the ligand into the microporous structure could have resulted in high hydrolysis rates. In this section, the different steps of the CDI activation and ligand immobilisation procedure are discussed, with some experimental improvements suggested.

### *5.4.1 Limitations of Functionalisation Procedure*

CDI activation occurred with the hydrogel suspended in acetone rather than water, as CDI readily hydrolyses in water [114]. Acetone used in this research was technical grade, with a purity of 98%, meaning there was residual water in the activation solution. CDI was added

in excess to react with the water and maintain maximum activation yield of the hydroxyl groups on the hydrogel. In order to test if CDI reacting in acetone was significant, solutions of CDI in water and CDI in acetone placed in cuvettes, and the change in UV-vis absorbance over time was measured to track the consumption of CDI. Results for CDI in water clearly showed the consumption of CDI in water, completely reacting within 1 minute (Figure 5-13). However, this method could not be used to track the same consumption in acetone, because acetone saturated the UV detector when measuring the UV-vis absorbance, meaning addition of CDI could not be detected. Visual observation of the addition of CDI to water noted the vigorous formation of bubbles in water, while bubble formation was not seen with the addition of CDI to acetone, indicating no reaction occurred. Because there was no observed reaction, CDI was added in excess to the CDI/acetone/hydrogel solution, and because the hydrogels were successfully functionalised with a high ligand density, it is safe to assume that rapid hydrolysis of CDI was not a limiting factor in functionalisation of hydrogels.

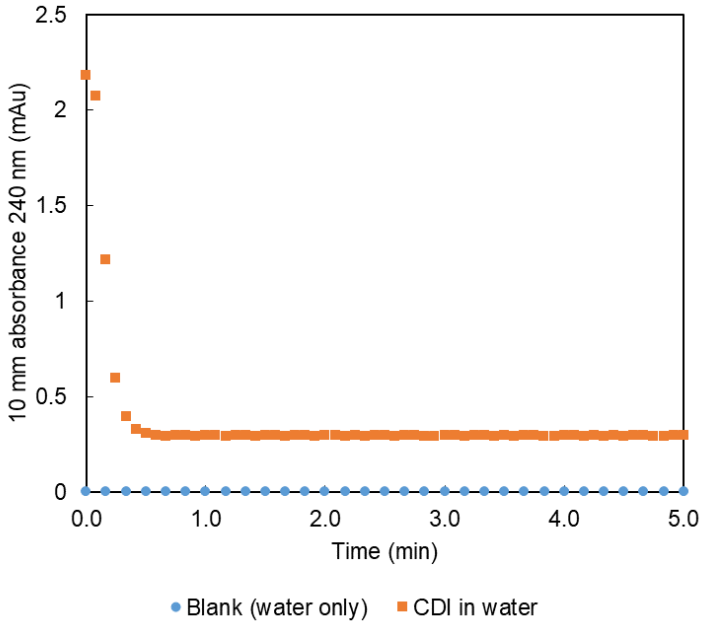


*Figure 5-13: CDI consumption in water compared with water blank, measured on NanoDrop*

Immobilisation of 6-aminohexanoic acid to hydrogel was conducted in the aqueous phase because of the nature of the ligand. This meant that the ligand immobilisation reaction competed with the hydrolysis reaction of the reactive imidazole intermediate on the surface of the hydrogel following CDI activation. The ligand immobilisation solution was 0.5 M 6-aminohexanoic acid and 1 M sodium bicarbonate, made up to pH 10 using 10 M NaOH, added dropwise. At pH 10, hydrolysis of the reactive imidazole group was recorded to be slow, taking 10 hours for complete hydrolysis. Hearn et al. found good immobilisation of the

ligand still occurred at this pH, although there will have been some competition between the immobilisation and hydrolysis reactions [68]. This reaction would further be limited with the by the slow diffusion of the ligand into the microporous structure, meaning the hydrolysis could have been more limiting than originally thought.

To see if the functionalisation was mass transfer limited, and if the imidazole intermediate hydrolysis was significant, a recirculating functionalisation system was created (Section 3.7). 30 mm long monoliths were made according to the description in Section 3.14 and were activated with CDI and functionalised with 6-aminohexanoic acid using both the batch methodology and the new recirculating method.

The CM TPMS columns analysed in previous chapters were functionalised using a batch functionalisation technique, where the column was placed in a 50 ml centrifuge tube with the functionalisation reactants and agitated for the reaction duration. The agitation provided good mass transfer via forced convection to the outer walls of the columns, but not through the channels, which relied on mass transfer via diffusion. In the previous chapters the ligand density was assumed to be uniform across the hydrogel surface in the whole column, however it was unknown if this was the case. In order to improve the mass transfer of reactants through the channels, a low flowrate recirculating functionalisation method was developed to provide flow through the channels, promoting advective mass transfer and improving the distribution of ligands immobilised to hydrogel surface.

Agarose monoliths were used to compare the effectiveness of the batch functionalisation method with the recirculating functionalisation method. TPMS hydrogel columns were not used due to the availability of the Solidscape printer, and the fact that the following analysis required the columns to be cut into slices. Monoliths immobilised with the CM ligand were left if highly concentrated cytochrome c solutions to fully saturate the columns in protein. Columns were then sliced into discs and analysed for cytochrome c distribution. It was assumed that cytochrome c distribution correlated directly to the ligand distribution. Cytochrome c adsorbed to the columns was clearly seen in rings around the internal monoliths of the columns as well as around the outer radius of the column. A representation of the cytochrome c adsorption to columns functionalised by both methods is shown in Figure 5-14. In both (a) and (b), the slices correspond to the outer ends of the column (furthest left and right), and the middle two slices are examples of the internal cross-section. Complete protein binding and ligand distribution was demonstrated on the ends of the columns where the hydrogel was fully saturated with the red protein. Slices taken from inside the column

showed slight penetration of protein into the pores of the column through the monolith channels, and non-uniform distribution around the outer diameter of the column functionalised using the recirculating method, where there were segments of the wall with no apparent protein adsorption. Please note the breakage shown in Figure 5-14 (a) was due to the handling of the column after the experiment was conducted.

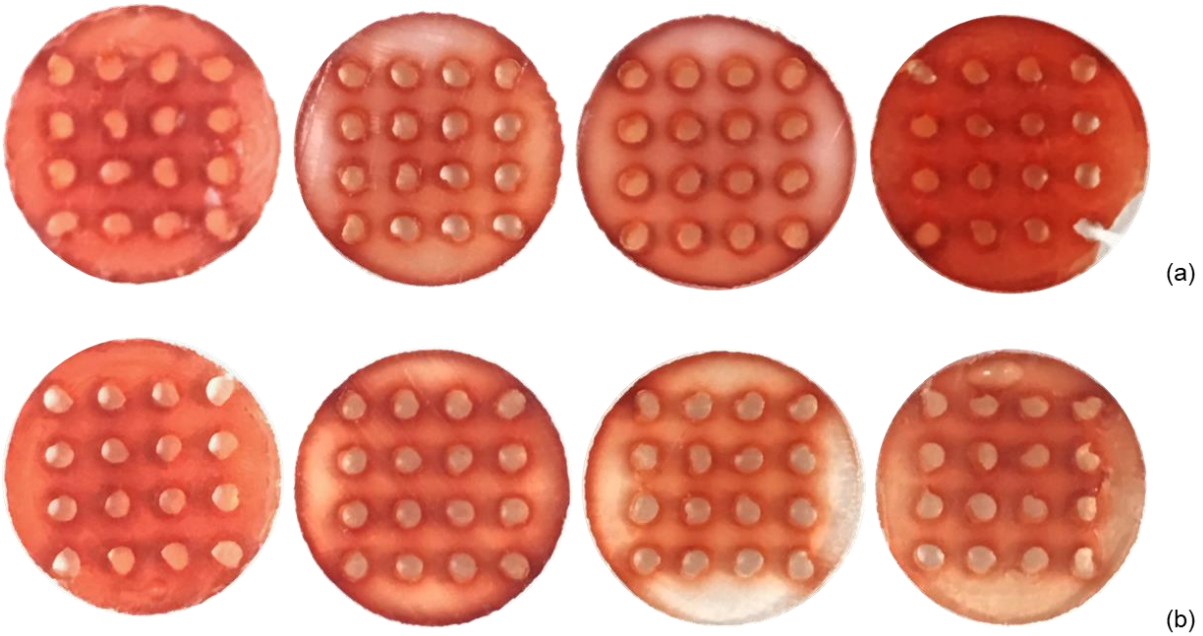


*Figure 5-14: Cytochrome c adsorbed to segments of monolith agarose column functionalised using (a) batch method, and (b) recirculating method. Example slices are far top (far left), inner (middle two) and bottom (far right).*

Images of each slice of the agarose columns were analysed using Fiji, where the thickness of the cytochrome c rings around the monolith channels and columns' outer walls were used determine the depth of penetration of the ligands within the hydrogel and the uniformity of the ligand immobilisation. The average penetration depth for cytochrome c in the internal monolith channel as a function of column length was plotted for both the batch and recirculating functionalised column (Figure 5-15). The average penetration length inside the columns were 0.120 $\pm$ 0.005 mm and 0.170 $\pm$ 0.005 mm for columns functionalised using the batch adsorption method and recirculating method respectively. The penetration depth increased using the recirculating functionalisation method, meaning mass transfer was improved within the channel because of the greater thickness of the cytochrome c layer around each channel wall meant there was more ligand immobilisation. This also means that the batch functionalisation method was limited by the rate that the ligand was transferred to the active imidazole intermediate on the hydrogel surface, and competitive hydrolysis of the

active intermediate was a factor in the ligand immobilisation yield obtained using the batch method.

Along the length of the column functionalised using the batch method, cytochrome c penetration of the monolith channels decreased slightly, averaging from 0.17 ± 0.03 mm in the first internal slice of the column to 0.09 ± 0.02 mm in the last slice, and the overall variance in these results was 0.006 mm². When considering this result in the context of the TPMS columns, the low variance indicates that ligand immobilisation density was uniform on the columns. For batch functionalisation, it was expected that slices closer to the ends of the column would have the higher ligand immobilisation because of shorter diffusion lengths of CDI for activation and ligands used in functionalisation. When longer diffusion times were necessary, such as to the centre of the column, there was potential for the reactive imidazole intermediate to hydrolyse before coming into contact with the ligand.

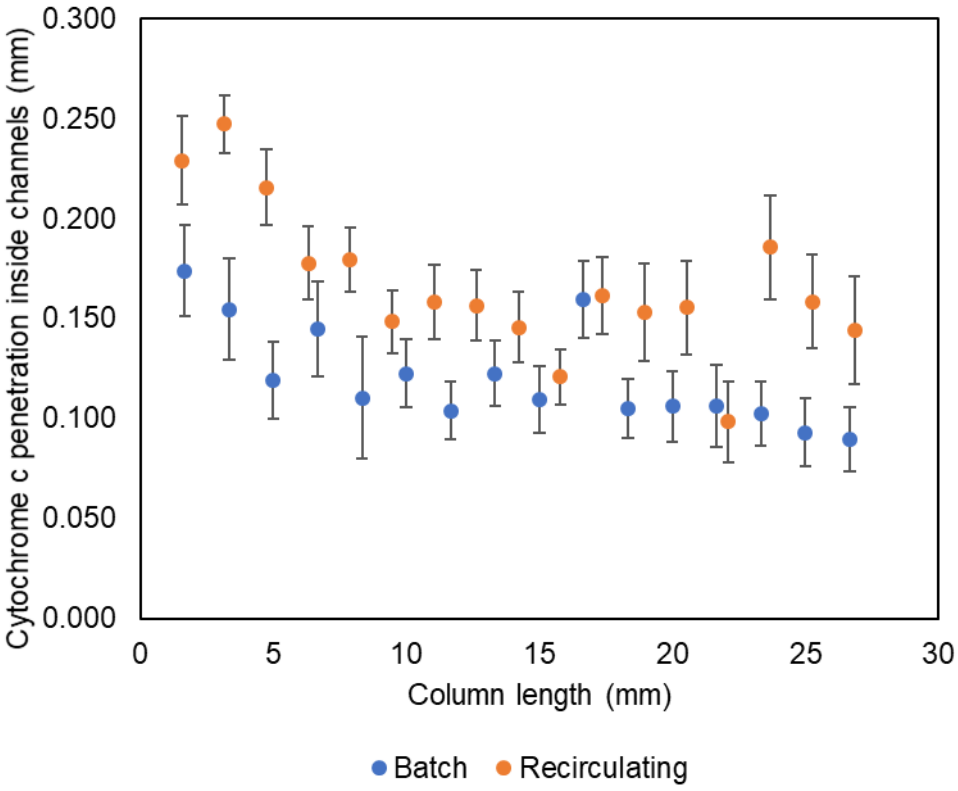


*Figure 5-15: Average cytochrome c penetration inside monolith channels on 30 mm agarose columns functionalised using batch and recirculating methods*

The variance in the channel functionalisation depth on the columns functionalised using the recirculating method was 0.009 mm², larger than that of the batch-functionalised columns. This shows that ligand immobilisation was less uniform within the channels along the channel lengths, although the overall average depth of penetration was larger than the

batch-functionalised column. The larger penetration depth means the recirculating functionalisation method increased the mass transfer rate of functionalisation reactants from the bulk channel flow to the channel walls and was not limited by the rate of diffusion of the reactants within the internal porous structure of the channels. With a greater penetration depth compared with the batch functionalisation method, the ligand density and hence protein binding capacity of monoliths functionalised using the recirculating method should be higher. From these results, the recirculating functionalisation method should be implemented in TPMS columns functionalised in the future, in order to yield higher ligand immobilisation densities within the channels.

The depth of cytochrome c penetration on the columns' outer diameters was also measured as a function of column length for columns functionalised using both methods. Cytochrome c penetration was expected to be large and uniform on the batch functionalised column, because the column was completely submerged and continuously agitated for the reaction duration, meaning the was good mass transfer to the wall surface. On the column functionalised using the recirculating method, penetration was expected to be like that of the batch method, with an even distribution along the outer walls and constant with column length. In reality, the average wall penetration depths were $0.263 \pm 0.006$ mm and $0.244 \pm 0.009$ respectively for the batch functionalised and recirculating functionalised columns respectively. Figure 5-16 below shows the differences between the outer wall protein penetration along the length of the columns for the columns produced using the batch method and recirculating method. The batch method had a higher average penetration depth than the recirculating method because the recirculating method yielded a non-uniform ligand immobilisation distribution along the length of the column. During the recirculating method, the column was placed in a glass casing, and it was assumed that there was even flow distribution around the column. However, the area of the column with no protein adsorbed meant no ligand was immobilised, indicating that the column was pressed up against the wall of the column casing and the surface could not be accessed by the ligand immobilisation reaction solution while it was recycled around the column.

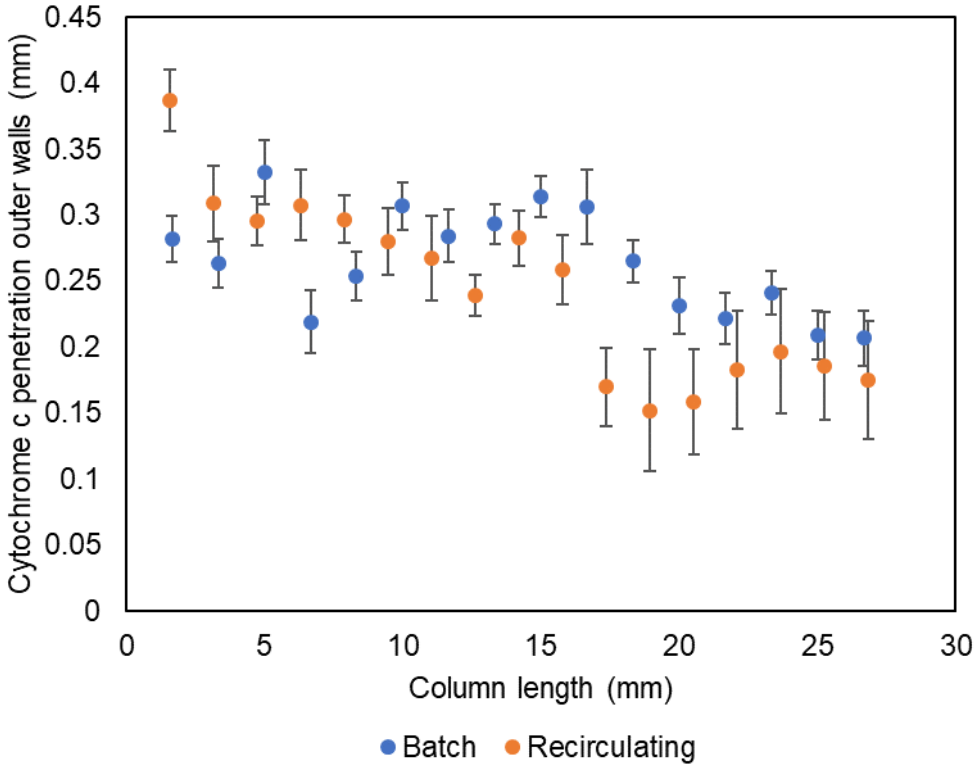


*Figure 5-16: Average cytochrome c penetration of outer wall of 30 mm agarose column functionalised using batch and recirculating methods*

The penetration depth around columns functionalised using the batch method had a variance on 0.005 $mm^2$, showing uniform distribution was achieved. The variance in penetration depth around the recirculating functionalised column was 0.02 $mm^2$, showing significantly less uniform distribution as a result of the method. If the columns were TPMS rather than monolith plugs, it would be expected that the ligand immobilisation distribution would not be affected by this, because the horizontal flow channels would carry the functionalisation reactant mixture to the outer walls much more effectively than in the monolith plug. Furthermore, the non-uniform ligand density seen here was likely a result of defects in the 3D-printed template given the printer used to create to monoliths has a low resolution meaning the size of the defects was large.

Considering the average cytochrome c penetration depth inside the channels explains the reason that TPMS channels with smaller diameter channels and walls had higher ion exchange capacities than those without. Assuming the penetration depth inside the TPMS walls was constant regardless of the channel diameter, this meant that hydrogel wall features with a smaller diameter would have a higher percentage functionalised than those with larger diameters. This is shown schematically Figure 5-17 below, where the radius of penetration

(red) is constant for channel sizes of three different diameters, resulting in varying diameter unfunctionalised cores (grey).

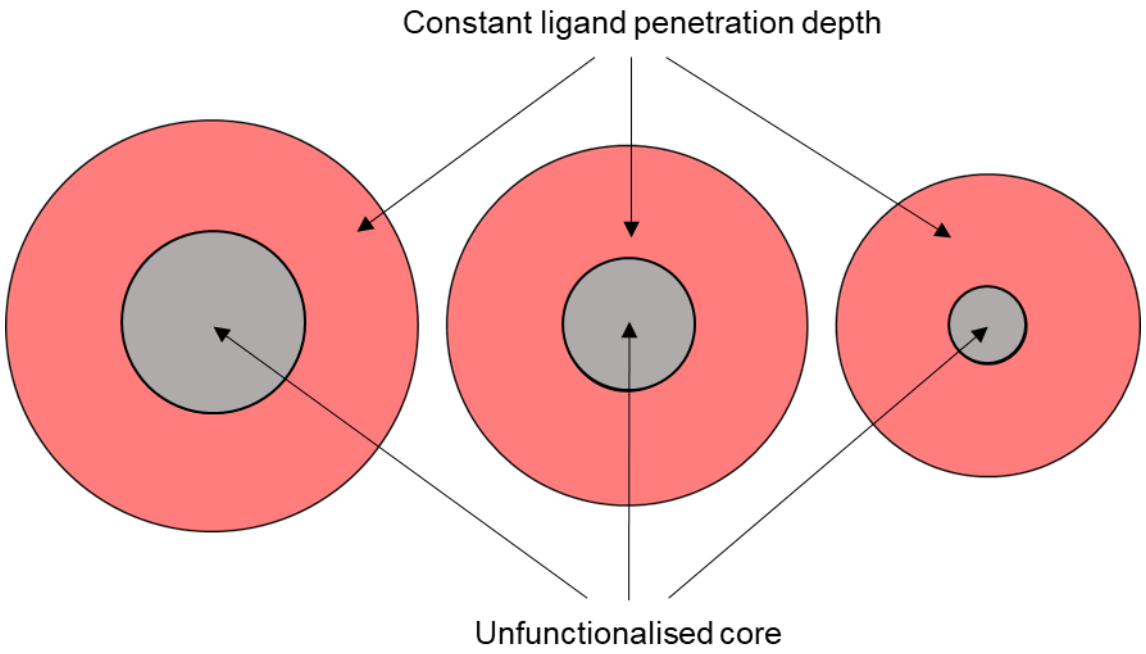


*Figure 5-17: Schematic demonstrating unfunctionalised hydrogel core of different diameter walls with ligand penetration radius*

When TPMS column hydrogel walls were approximated to a cylinder, the percentage of a cross-section of the channel walls functionalised varied depending on the wall diameter (Table 5-10). Using the three hydrogel wall diameters of the TPMS columns made in this research (300 µm, 400 µm and 500 µm), and the cytochrome c penetration depth experimentally determined for the walls of the batch-functionalised and recirculating-functionalised monolith channels, the percentage functionalised on an area basis was calculated. Calculations showed that the percentage of hydrogel functionalised increased with decreasing wall diameter, mirroring the ion exchange capacity results in Chapter 4. 300 µm features had a functionalisation percentage of 96.0% of the cross-section when functionalised using the batch method, which was calculated to increase to 100% with the recirculating method because the penetration depth of cytochrome c was larger than the radius of the wall. Changing the functionalisation method from batch to recirculating would theoretically result in the whole TPMS structure being functionalised when the TPMS features are 300 µm, and would increase the ligand immobilisation density and hence ion exchange capacity of TPMS structures with 400 µm and 500 µm features significantly, showing the benefit of the

implementation of the recirculating functionalisation method on columns produced in the future.

*Table 5-10: Theoretical functionalisation percentages for TPMS columns functionalised using batch and recirculating method*

| Wall diameter<br>μm | Percentage of wall cross-section functionalised, batch<br>% ($mm^2/mm^2$) | Percentage of wall cross-section functionalised, recirculating<br>% ($mm^2/mm^2$) |
|---|---|---|
| 300 | 96.0% | 100.0% |
| 400 | 84.0% | 97.8% |
| 500 | 73.0% | 89.8% |

Cytochrome c binding capacity was also measured on the monolith columns, which was found to be 59.5 mg/ml and 59.1 mg/ml for the columns functionalised using the batch and recirculating method respectively. This was a negligible difference, however when considering the columns produced using the recirculating method had surface with no ligand immobilisation, the binding capacity could be higher if column defects resulting in non-uniform distribution of functionalisation reactants around the column were avoided.

### 5.4.1 Functionalisation Effects on Porosity

SEM images of freeze-dried hydrogel samples were analysed to determine the mean pore diameter for cellulose and agarose samples before and after functionalisation. It was previously assumed that functionalisation would not affect the pore diameter, however it was shown that the functionalisation process increased the pore diameter on both cellulose and agarose (Figure 5-18), because of the reduction on hydrogen bonds in the hydrogels during functionalisation, with the substitution of the hydroxyl groups with the immobilised ligand-carbamate linkage. The cellulose mean pore diameter was 0.72 ± 0.1 μm when unfunctionalised, which increased to 4.8 ± 0.7 μm after functionalisation with the CM ligand. Agarose mean pore diameter was nearly double this, increasing from 3.9 ± 1.1 μm to 8.4 ± 2.0 μm after functionalisation. These pore diameters were lower than those determined for cellulose and agarose beads by Johnson et al., where the mean pore diameters were 10 μm and 20 μm respectively. The gelling method, temperature, crosslinker type and concentration all effect the pore diameter [20], hence it is difficult to predict the final pore diameters of the hydrogels.

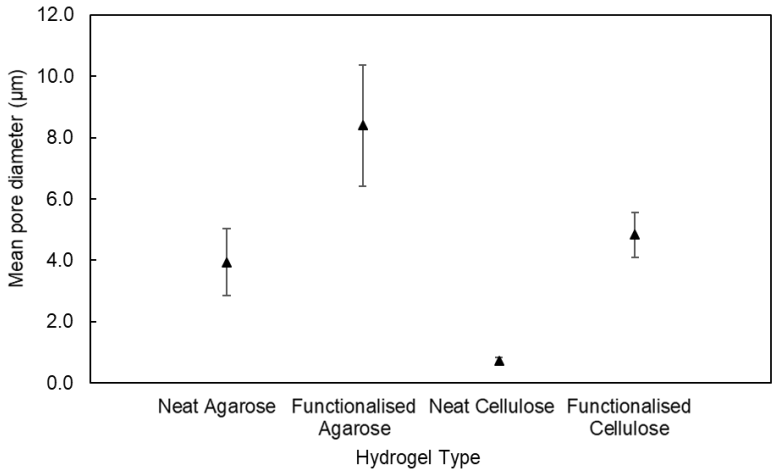


*Figure 5-18: Mean pore diameter of hydrogels before and after functionalisation*

RTD curves (Figure 5-19) on the monoliths show there was a difference in the channel void volume (indicated by the blue dextran curves) and the porous void volume (indicated by the acetone curves), and a change in these occurred with CDI activation and CM ligand immobilisation. With blue dextran, mean elution volume increased from 0.67 ml to 0.74 ml when the column was functionalised, and the acetone mean elution volume increased from 0.79 ml to 1.03 ml. This corresponded to a pore fraction increase from 0.05 to 0.12 with functionalisation, more than doubling the void volume in the monoliths attributed to pores. An increase in both volumes demonstrated that the functionalisation method caused changes to the column voidage by creating larger pores (supported by the pore diameters calculated above) through the chemical modification, as well as increasing features on the macro scale that blue dextran, a large molecule, could interact with.

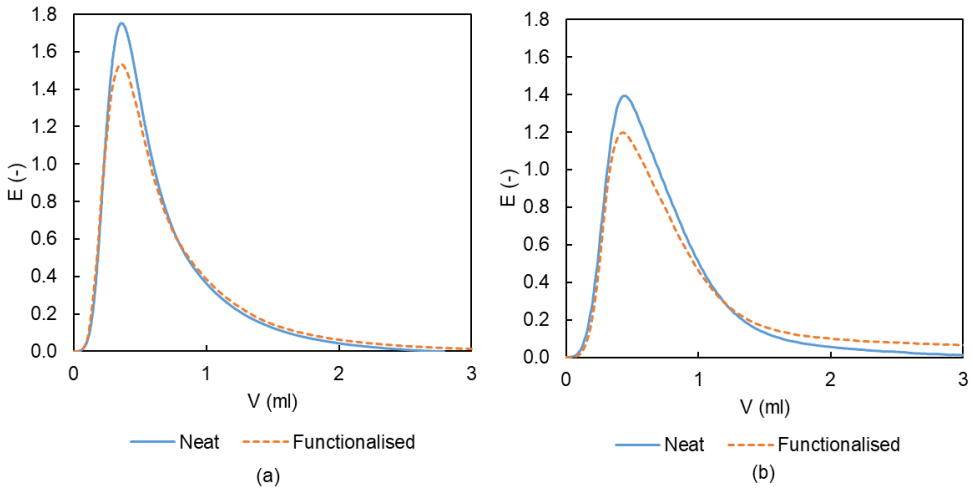


*Figure 5-19: RTD Curves for (a) blue dextran and (b) acetone on agarose gyroid monoliths before and after functionalisation*

With the increase in mean pore diameter in hydrogel, and the overall increase in macro and micro void volumes after functionalisation, it is clear that the changes occurring to the hydrogel structure are difficult to predict and understand. This implications on the functionality of the columns is that differences in pore structure effect the overall surface area available for functionalisation, the pores accessible to proteins via advection or diffusion, and make adsorption performance difficult to predict. It is important that these effects on functionalisation are understood in order to be able to produce TPMS columns optimised for solid-tolerant chromatography.

## 5.5 Conclusions

In this chapter, protein adsorption to TPMS hydrogel columns was investigated under dynamic conditions. CM, DEAE, and HIC columns all successfully demonstrated adsorption and subsequent elution for model proteins. In bind-and-elute experiments, protein adsorption was higher at lower flowrates because there was less protein lost in the mobile phase via advection, and protein adsorption efficiency increased with decreasing channel diameter because of the greater ligand density from the higher surface area. Reduced plate height analysis showed pore diffusion reduced the chromatographic efficiency and was the main dispersive parameter, resulting in reduced plate height values much higher than those predicted computationally [85] because of the higher porosity of the TPMS hydrogel structures compared with the 50% void structures analysed by Dolamore. The TPMS hydrogel columns' geometries were limited by CAD software and 3D-printing technologies, which meant optimal geometries, such as large diameter columns, could not be tested. It is expected that with improved software and technology, TPMS columns with larger diameters could be printed, resulting in lower reduced plate heights and better chromatographic efficiency.

Overall, the results in this chapter demonstrated a clear mass transfer limitation on the TPMS hydrogel columns. Because of the large diameter channels and small pore diameters, protein was lost from the columns via advection through the channels, because protein diffusion in the bulk flow to the channel walls and through the pores was much slower compared with advection. Because of this, protein adsorption was much higher at lower linear velocities, and better breakthrough performance was observed at these lower velocities, where more protein could be loaded on to the column before the mass transfer zone was reached.

Protein adsorption was higher on cellulose hydrogel columns compared with agarose columns of the same channel size, as was shown by the saturation binding capacities calculated from protein breakthrough experiments. Cellulose had a higher percentage of polysaccharide in the hydrogel matrix and a greater surface area from smaller pore diameter, meaning a higher ligand density (as was determined in Chapter 4). Based on the protein breakthrough curves, G400C-CM had the best breakthrough performance because of its high ligand density.

Dynamic binding capacities for TPMS hydrogels were much lower than those of commercial resins because of mass transfer limitations. Analysis of $DBC_{10\%}$ showed that the $DBC_{10\%}$ decreased with increasing linear velocity, up until a point where advection was completely limiting and there was no change in $DBC_{10\%}$. High $DBC_{10\%}$ at low linear velocities required long operating times, which is not feasible for commercial chromatography practices, which require fast linear velocities for high through-put and acceptable yield. It was proposed that these columns be operated at a high velocity, reaching $DBC_{10\%}$ quickly, with the flow-through recycled. This would require further optimisation for protein adsorption efficiency, pumping costs, and consumables costs.

Analysis of the batch functionalisation procedure used to immobilise ligands to the hydrogels showed CDI activation was not likely to have limited the overall ligand immobilisation density. However, once the hydrogels were activated with CDI, the fast hydrolysis reaction of the CDI intermediate and slow ligand diffusion into the porous structure meant that not all the available active intermediates reacted with the ligands. Comparison of the batch and recirculating functionalisation methods showed the changing the functionalisation method to recirculating increased the ligand immobilisation inside monolith channels, because the active delivery of ligand into the monolith channels meant the ligand reached the CDI active intermediates before they were completely hydrolysed.

Changes to the porous microstructure of the hydrogels occurred with functionalisation, whereby the pore diameter and void volumes of the agarose monoliths increased. This was due to the reduction in hydrogen bonding in the hydrogel, as hydroxyl groups were substituted for cation exchange ligands. There is little literature on the effects of chemical modification on hydrogel pore diameter, and it is recommended that further work be conducted to understand this phenomenon. Accurate understanding of pore structure would enable more accurate prediction of TPMS column surface area, size exclusion effects, and controlling dispersive effects.

# Chapter 6. Cell Recovery on TPMS Hydrogels

## 6.1 Introduction

This thesis looks at the development of TPMS hydrogel structures to be used in solid-tolerant chromatography. In the previous chapters, TPMS hydrogel structures were prototyped using a 3D-printed TPMS template and functionalised for common modes of chromatography. Protein adsorption to the column under static and dynamic conditions proved the adsorptive functionalities and limitations of these columns, where smaller TPMS features and lower flowrates yielded the highest protein adsorption. This chapter demonstrates the second part of the purpose of the TPMS hydrogel columns: the ability of solids to be removed from a feedstock by a TPMS hydrogel column without significant loss in protein adsorption efficiency. Solutions of 0.5% w./w. bakers' yeast (*Saccharomyces cerevisiae)* rehydrated in buffer solutions mixed with proteins were used to simulate a fermentation broth. Yeast passage was analysed for the TPMS hydrogels of different channel diameter, geometry, hydrogel type and chromatographic mode. The effect of the mobile phase velocity was analysed for the gyroid columns, and SEM images showed some cell retention in the columns. For the TPMS hydrogels to work successfully as a solid-tolerant chromatography column, solid particle recovery through the column must be 100%; this means in a sample loaded onto the column, all of the solid material flows through the column without becoming stuck in the columns.

Protein concentration from yeast cells was neglected, because in a 2.0 ml sample of 0.5% w/w yeast, these proteins are 40% of the yeast cell [115], making up 0.2% w/w of the sample, or approximately $2 \times 10^{-4}$ mg/ml which is negligible compared with protein concentrations added to these samples loaded onto the column (2.0 mg/ml). Cation uptake of yeast cells has been reported, whereby the negative charge of the cell wall will absorb cations in solution [116], however the relative concentrations of cell and protein make this negligible, too.

## 6.2 Preliminary Cell Passage

The ability of the TPMS hydrogel columns to process a simulated fermentation broth was demonstrated by comparing protein adsorption and cell passage in bind-and-elute experiments where the chromatograms for a protein only solution, cell only solution, and protein and yeast mixture were loaded onto the columns. Proteins on each column were the

same as in Section 5.2 (described in Seciton 3.10.2), and bakers' yeast (*Saccharomyces cerevisiae)* was used as the cell. Cell recovery was the amount of yeast detected in the flow-through peak compared with the amount of yeast in the on-sample. Each injected sample had a volume of 2.0 ml and was loaded onto the column at 1.0 ml/min (76.0 cm/h).

### 6.2.1 TPMS CM Columns

The chromatograms below show protein adsorption on G300A-CM was unimpeded between the protein only and protein and yeast mixtures loaded onto the column (Figure 6-1). The cytochrome c and yeast mixture curve was the approximate sum of the cytochrome c and yeast only curves, indicating the protein binding and cell passage were independent of each other in the mixture. Protein-yeast interactions in solution could be neglected because the relative concentration of yeast cells was low compared with the protein concentration. Absorbance at 280 nm and 600 nm were both recorded, because cytochrome c absorbs at 280 nm, and yeast at 600 nm, however both compounds demonstrated absorbance at both wavelengths, because of the protein was in the reduced form and absorbs light at 552 nm [117].

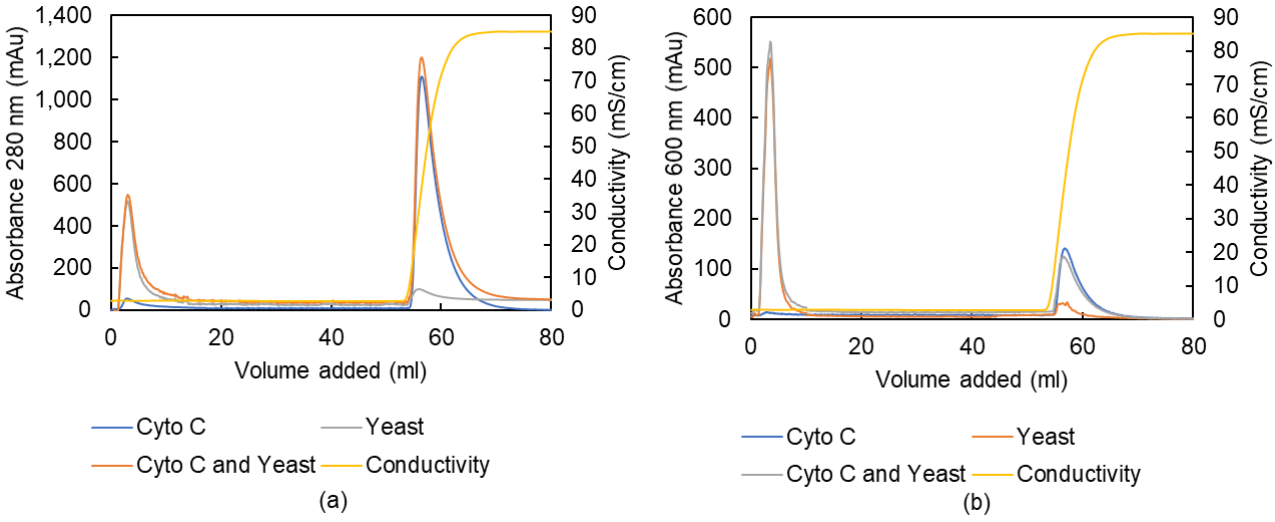


*Figure 6-1: Chromatogram of UV absorbance at (a) 280 nm and (b) 600 nm for cytochrome c, yeast, and cytochrome c plus yeast on G300A-CM*

Optical density analysis of the yeast fractions at 600 nm gave a yeast recovery of 33.0% in the flow-through peak and 3.4% in the elution peak, showing that 100% cell passage was not achieved in the flow-through, nor was 100% of the yeast accounted for over the whole experiment, indicating some cell hold-up in the column. Small channel diameters mean that cell retention because of straining and interception was likely [61]. A small peak in the yeast

only run after elution buffer was applied demonstrated eluted material, likely to be extracellular proteins secreted by the yeast cells or some cells binding due to the slight affinity of yeast to cation exchange resins. Tari et al. reported an interaction coefficient of 0.095 at this conductivity, meaning some cellular material could adsorb to the column [49]. TPMS columns with features of this diameter are not appropriate for cell processing given the low recovery, although this could be improved with a higher flowrate on-sample because of the increased advective mass transport.

Gel electrophoresis was conducted on fractions taken from the cytochrome c and yeast mixture that was loaded onto G300A-CM, shown in Figure 6-2. Yeast (Y) and cytochrome c (C) were measured separately to demonstrate their presence in the on-sample (ON) that was loaded onto the column. Fractions collected from the flow-through peaks (F) were combined and freeze dried to concentrate the species in case it was too dilute to be detected. The freeze-dried product was rehydrated in 0.5 ml phosphate buffer before being prepared for gel electrophoresis. Buffer washing (W) and elution fractions (E1, E2 and E3) were also collected. Cytochrome c was present in C, ON, and the elution ladders, demonstrating protein capture and elution upon the addition of the salt buffer, shown by the band just below the 15 kDa reference ladder because the molecular weight of cytochrome c is approximately 12.3 kDa. Yeast was indicated by the cloudy mixture seen in Y, because of the combination of extracellular solubles and cellular material in the sample. Yeast was also present in the ON and F, showing yeast flowing through the column. Yeast did not show up in the elution lanes despite a small amount being detected in the chromatogram, likely because it was too dilute.

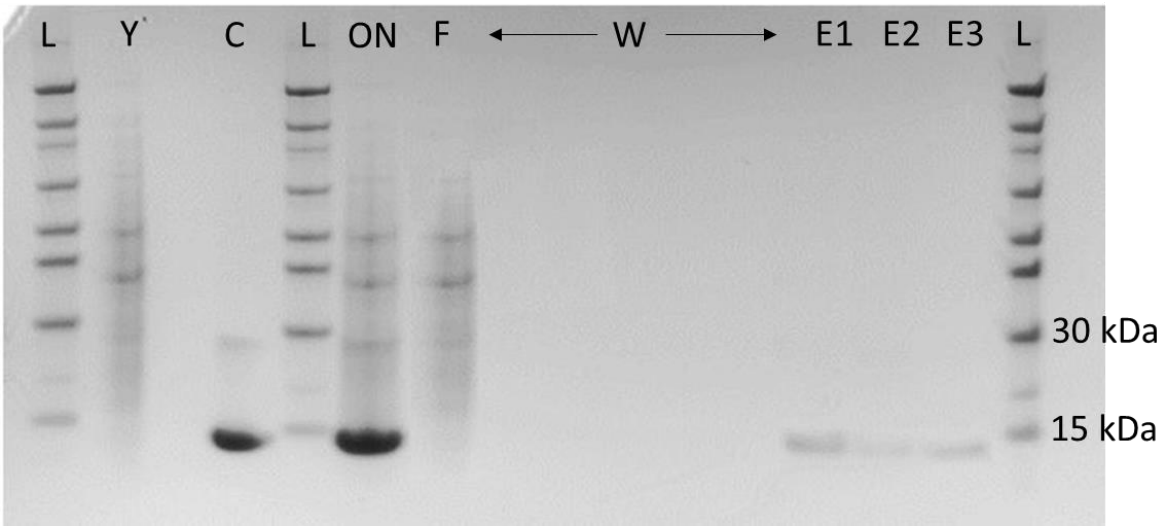


*Figure 6-2: Gel electrophoresis of fractions from cytochrome c and yeast mixture loaded onto G300A-CM at 1.0 ml/min. L: ladder, Y: yeast, C: cytochrome c, ON: on-sample, F: flow-through, W: wash, E1: elution 1, E2: elution 2: E3: elution 3.*

Cell recovery on G400A-CM (Figure 6-3) and G500A-CM (Figure 6-4) was improved in comparison with G300A-CM, because yeast recovery was 77% and 87% respectively, again with negligible interference in protein binding in the presence of yeast cells because there was little difference between the area under the elution fractions when measured with the UV-vis at 280 nm. Small amounts of yeast were detected in the elution peaks as with G300A-CM, but this accounted for less than 1% of the initial on-sample. The deficit in the mass balance between the on-sample, flow-through and elution meant that approximately 32% and 13% of the cells remained in the column after the run on G400A-CM and G500A-CM respectively. Application of 1 M NaOH to the column did not result in further elution of the yeast cells, indicating the cells were not irreversibly adsorbed, rather they were stuck in the geometric features of the columns.

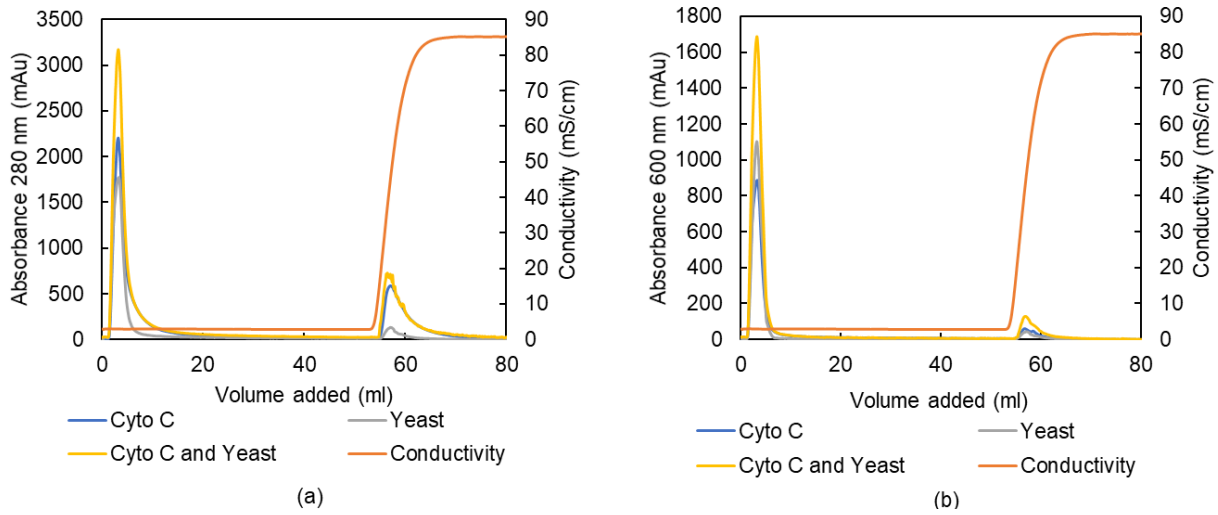


*Figure 6-3: Chromatogram of UV absorbance at (a) 280 nm and (b) 600 nm for cytochrome c, yeast, and cytochrome c plus yeast on G400A-CM*

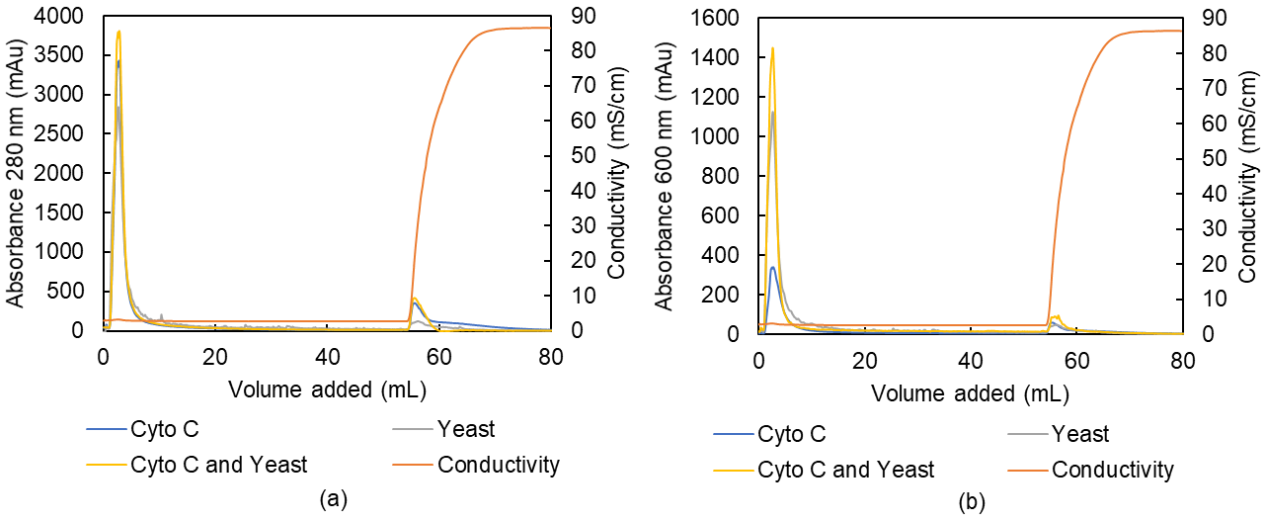


*Figure 6-4: Chromatogram of UV absorbance at (a) 280 nm and (b) 600 nm for cytochrome c, yeast, and cytochrome c plus yeast on G500A-CM*

On SD500A-CM, the chromatogram analysed at an absorbance of 600 nm showed yeast passage in the flow-through peak with a small fraction of yeast elution upon the addition of the salt buffer (Figure 6-5). Optical density measurements of the fractions yielded cell recovery in the flow-through of 94.2%, with 1.4% presented in the elution fractions. This meant approximately 4.4% of the yeast remained in the column after the run. Schwarz diamond has a lower tortuosity than the gyroid, meaning inertial impaction of solids is reduced, hence the higher cell recovery obtained on SD500A-CM compared with G500A-CM. As with the other cation exchange columns, a small fraction of the yeast on-sample was eluted with application of salt buffer because of the slight interaction between cell and adsorbent. Cytochrome c adsorption was unchanged between the protein only investigation and the protein-yeast mixture investigation, demonstrated in the comparison between the absorbance at 280 nm for cytochrome c only and cytochrome c-yeast mixture, where the absorbance in the latter was the sum of the peaks in the cytochrome c only and yeast only trials.

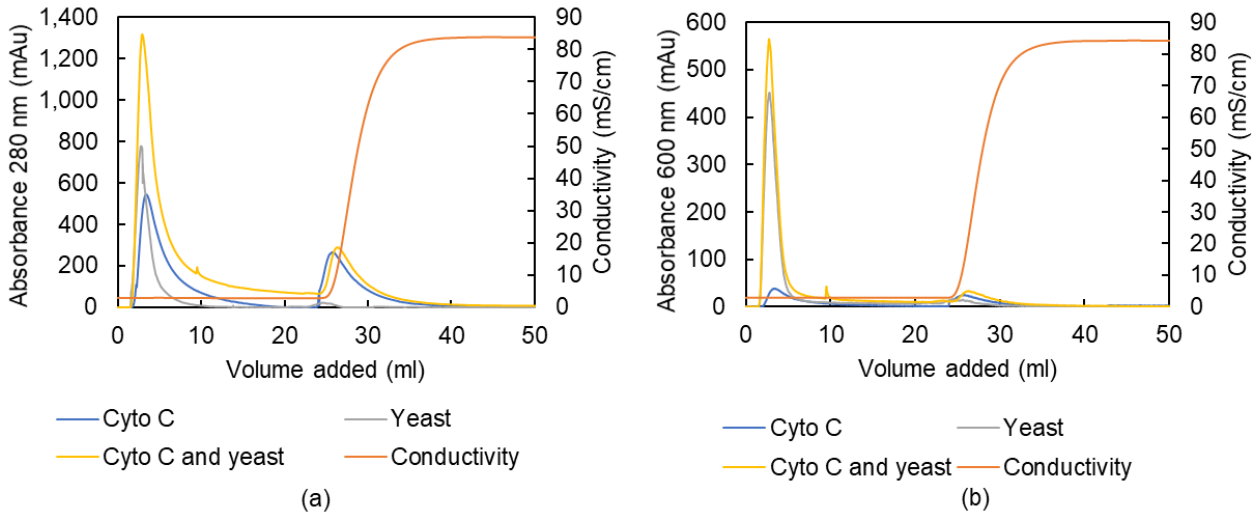


*Figure 6-5: Chromatogram of UV absorbance at (a) 280 nm and (b) 600 nm for cytochrome c, yeast, and cytochrome c plus yeast on SD500A-CM*

The combined UV absorbance at 280 nm show there is little change in behaviour between the capture of cytochrome c on G500C-CM in buffer only and when it is in a yeast mixture, meaning the presence of solids does not perturb protein binding capacity. Yeast passage was calculated the optical density of the fractions collected over the run, yielding a cell recovery of 87.0% in the flow-through peak, 2.4% in the elution peak, and 10.6% remaining in the column. The geometric properties of G500C-CM were the same as G500A-CM on the macroscale, hence similar cell recovery on should have been measured on each column, which was the case. The differences in microstructure between agarose and cellulose should not influence cell recovery, because cells do not interact with microporous structures, as their large size excludes them from interacting with pores the same diameter or smaller. A summary of the protein adsorbed and yeast cells recovered is provided in Table 6-1.

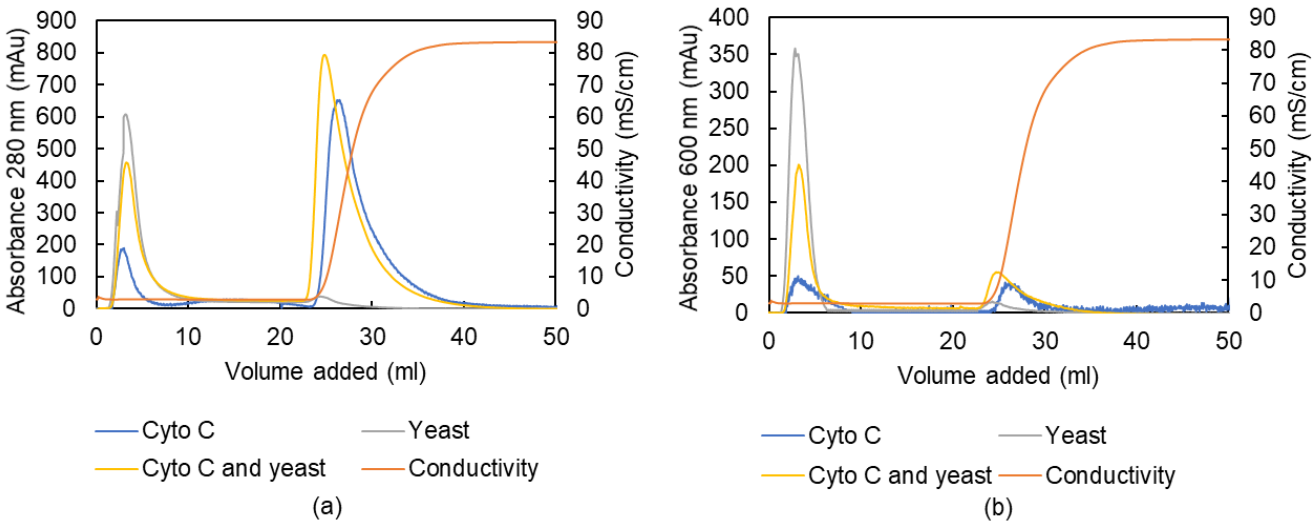


*Figure 6-6: Chromatogram of UV absorbance at (a) 280 nm and (b) 600 nm for cytochrome c, yeast, and cytochrome c plus yeast on G500C-CM*

*Table 6-1: Protein adsorption and cell recoveries for CM columns*

| | **Protein adsorbed** | **Cell recovery in flow-through** |
|---|---|---|
| | % on-sample w/w | % on-sample w/w |
| G300A-CM | 95% | 33% |
| G400A-CM | 31% | 77% |
| G500A-CM | 22% | 87% |
| SD500A-CM | 38% | 94% |
| G500C-CM | 85% | 87% |

Overall, the results from the bind-and-elute experiments did not demonstrate 100% cell recovery in the flow-through peak for any of the TPMS hydrogel columns at the linear velocity tested. Cell recovery was related to channel diameter, where cell recovery increased with increasing channel diameter. Increased channel diameter reduced the effects of interception and inertial impaction, demonstrated by the decreasing aspect ratio and Stokes number with increased channel diameter, calculated in Table 6-2. These parameters were calculated assuming a cell diameter of 40 µm, and cell density of 1,112.6 kg $m^{-3}$ [118]. Because larger channel diameters increased the distance that an entrained cell had to be carried by inertia before impacting with the channel walls, inertial impaction was reduced. Typical values for the Stokes number are between $1x10^{-9}$ – $2x10^{-3}$, with higher numbers indicating cells travelling with higher inertia. Values calculated for these experiments ranged between 0.000126 – 0.000075, indicating that although inertial impaction reduced in columns

with larger channel diameters, it was still comparable with typical deep bed filtration values where solid retention is desired. Effects of inertial impaction would be reduced with further increases to channel diameter.

*Table 6-2: Calculated sedimentation mechanism parameters from bind-and-elute experiments*

| Column ID | G300A-CM | G400A-CM | G500A-CM | SD500A-CM | G500C-CM |
|---|---|---|---|---|---|
| $N_R$ | 0.13 | 0.10 | 0.08 | 0.08 | 0.08 |
| $St$ | 0.000126 | 0.000094 | 0.000075 | 0.000075 | 0.000075 |
| $N_G$ | 0.236 | 0.236 | 0.236 | 0.236 | 0.236 |
| $Re_l$ | 0.082 | 0.110 | 0.137 | 0.108 | 0.137 |

The effects of hydrodynamic interactions lessened with increasing channel diameter, demonstrated by the modified Reynolds number, which increased with increasing channel diameter and decreasing specific surface area. However, the modified Reynolds number was still below the condition for streamline flow for all columns, meaning some cell wander across streamlines was likely. On top of further increasing channel diameter, hydrodynamic interactions would decrease further with a faster flowrate, because cells would be carried out of the column via advection fast than they would wander across streamlines and become entrapped on the column.

Effects of sedimentation were dependent on interstitial velocity rather than channel diameter, hence was constant at for all channel diameters, because the interstitial velocity was constant with channel diameter, meaning the gravity number was also constant. This was calculated based on Equations 2-43 to 2-47 from Section 2.4.1.2, and the justification for this is shown in Table 6-3, where the velocity in a single channel was calculated on the basis of the channels having a circular cross-section with 50% voidage, with even distribution of flow-through the channels. The mechanisms of sedimentation become reduced with increasing interstitial velocity, therefore at higher flowrates, it is expected that cell deposition would reduce accordingly, increasing cell recovery.

*Table 6-3: Theoretical interstitial velocities for 10 mm diameter TPMS columns with 50% voidage with flowrate 1.0 ml/min*

| Channel Diameter | μm | 500 | 400 | 300 |
|---|---|---|---|---|
| Number of channels | (-) | 200 | 312.5 | 555.6 |
| Area one channel | $m^2$ | $1.96 \times 10^{-7}$ | $1.26 \times 10^{-7}$ | $7.07 \times 10^{-8}$ |
| Flowrate one channel | $m^3 s^{-1}$ | $8.33 \times 10^{-11}$ | $5.33 \times 10^{-11}$ | $3.00 \times 10^{-11}$ |
| Velocity one channel | $m s^{-1}$ | 0.000424 | 0.000424 | 0.000424 |

On top of typical sedimentation mechanisms, cell-adsorbent interactions were also prominent between the yeast cells and cation exchange columns, although there was no noticeable reduction in protein binding capacity of the columns. Small amounts of cellular and extracellular material adsorbed to the column; yeast was reported to have an interaction coefficient of 0.095 at the conductivity measured of the binding buffer [49]. This can be reduced by optimising the binding buffer salt concentration, increasing the ionic strength of the solution to reduce the relative charge between the cellular material and decrease the amount that binds to the column [46]. However, increasing salt concentration would also reduce the amount of protein that could adsorb to the column; it was concluded in Chapters 4 and 5 that the was a weak interaction between cytochrome c and the cation exchange ligand, evidenced by low equilibrium constants in the Langmuir analysis and immediate protein elution when elution buffer was applied to the columns in bind-and-elute experiments. The optimum point would require careful optimisation to prevent cell binding but maintain protein adsorption.

### *6.2.2 Other Chromatography Modes*

As well as cation exchangers, anion exchange and hydrophobic interaction columns were synthesised in this work.

#### 6.2.2.1 G400A-DEAE

G400A-DEAE demonstrated yeast cell passage, however there was a significant amount of yeast bound to the column, which was eluted off with the salt buffer, shown in the chromatograms below (Figure 6-7). The 600 nm absorbance chromatogram showed yeast cells clearly, however BSA did not show absorbance at 600 nm. With yeast and yeast and BSA mixture, there was a clear flow-through peak and elution peak signifying yeast binding to column and then eluted under salt conditions. Approximately 73.4% of the yeast was recovered in the flow-through, with the 16.6% eluting off with elution buffer and the remainder trapped in the column. This was expected, as at pH 7.0 in 20 mM phosphate buffer,

yeast cells will have a slight negative charge, meaning they will bind to the positively charged DEAE ligand [46]. Compared with the cation exchange resin, the interaction coefficient between yeast and the anion exchange resin was much higher, approximately 0.86 [49]. The magnitude of the interaction coefficient can be reduced with the increase of salt concentration and hence conductivity in the binding buffer, increasing the ionic strength of the solution and preventing yeast from binding to the column. As with the cation exchange column, this may also have an adverse effect on the binding capacity of BSA to the column; providing an optimisation problem that can be further investigated.

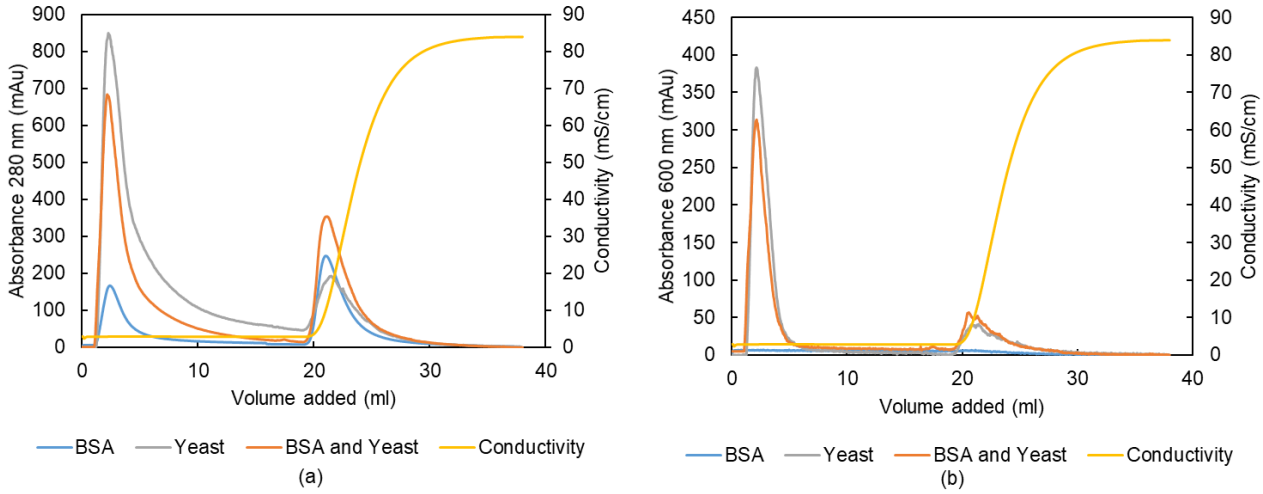


*Figure 6-7: Chromatogram of UV absorbance at (a) 280 nm and (b) 600 nm for BSA, yeast, and BSA plus yeast on G400A-DEAE*

#### 6.2.2.2 G400A-HIC

In the presence of yeast, α-lactalbumin was bound to G400A-HIC and subsequently eluted in the presence of elution buffer. This was concluded based on the combined absorbance chromatograms at 280 nm for the three trials: α-lactalbumin, yeast, and α-lactalbumin and yeast mixture (Figure 6-8). The α-lactalbumin curve showed approximately equal amounts of protein flow-through and eluted. For yeast only, a large flow though peak at 280 nm and small elution peak was observed, therefore a small amount of yeast was bound to the column due to some extracellular proteins associated with yeast having an interaction with the column. For α-lactalbumin with yeast a large flow-through peak (approximately the size of the combined α-lactalbumin flow-through and yeast flow-through) was recorded, with an elution peak similar to the size of the elution peak in the α-lactalbumin run. This indicated similar protein adsorption performance of the column with and without solids present in the

feed solution, showing yeast did not inhibit the performance of the benzylamine agarose column.

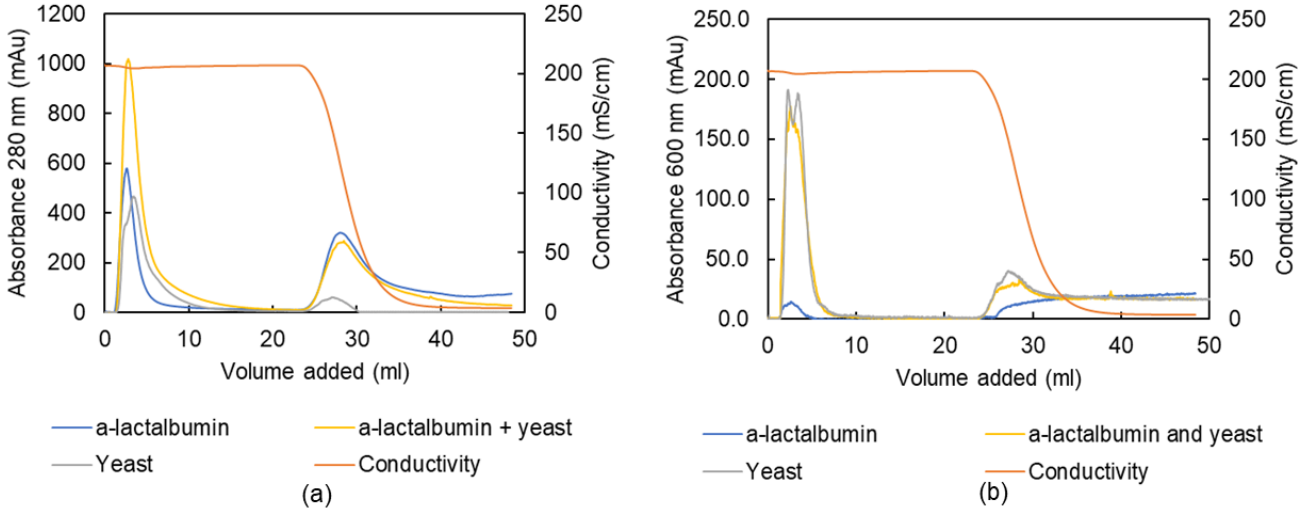


*Figure 6-8: Chromatogram of UV absorbance at (a) 280 nm and (b) 600 nm for α-lactalbumin, yeast, and for α-lactalbumin plus yeast on G400A-HIC*

Yeast passage through G400A-HIC was observed by monitoring the UV absorbance at 600 nm in Figure 6-8. The α-lactalbumin run shows α-lactalbumin has a very small absorbance at 600 nm. The yeast only run has a large flow-through peak and small elution peak; again, evidence of some adsorbent-adsorbate interaction. The yeast and α-lactalbumin with yeast track essentially the same over both sets of data on the 600 nm curve, showing the yeast passage was the same in both trials. Comparison of the peak intensities show that 73% of yeast flowed through the column, similar to G400A-CM, showing the same effect of gyroid channel on cell recovery. However, in this case, the was less cell hold up in the column and more yeast adsorbed to the column. Benzylamine has reported affinity to glycogen phosphorylase [68] which is present in yeast cells and therefore likely to be present in solution via secretion and cell breakage. Optimisation would be required to reduce the interaction between the yeast cells and proteins and the column; this would be done through changing salt concentration and pH.

It should be noted in Figure 6-8 that following the change in buffer from high salt to low salt resulted in a new baseline on the 600 nm UV absorbance curves, evidenced by each curve tailing to an absorbance of approximately 25 mAu.

## 6.3 Effect of Linear Velocity on Cell Recovery

From the preliminary bind-and-elute experiments, 100% cell recovery was not achieved on the TPMS hydrogel column. This was most likely because the flowrate of the on-sample was too low, meaning effects of hydrodynamic interaction and inertial impaction lead to cells being entrapped on the column. The effect of increasing the flowrate on cell recovery was determined by loading 2.0 ml of 0.5% w/w yeast samples onto each column at linear velocities of 76 cm/h, 153 cm/h, 382 cm/h, 573 cm/h and 764 cm/h (corresponding to flowrates of 1.0 ml/min, 2.0 ml/min, 5.0 ml/min, 7.5 ml/min, and 10.0 ml/min). After the initial flow-through peak was observed, the mobile phase velocity was increased to 764 cm/h to remove any further entrapped cellular material. Optical density at 600 nm of the fractions was measured to determine the cell recovery in the flow-thorough and high velocity wash. The cell recoveries are shown in Figure 6-9 and Figure 6-10 for the agarose and cellulose gyroids respectively.

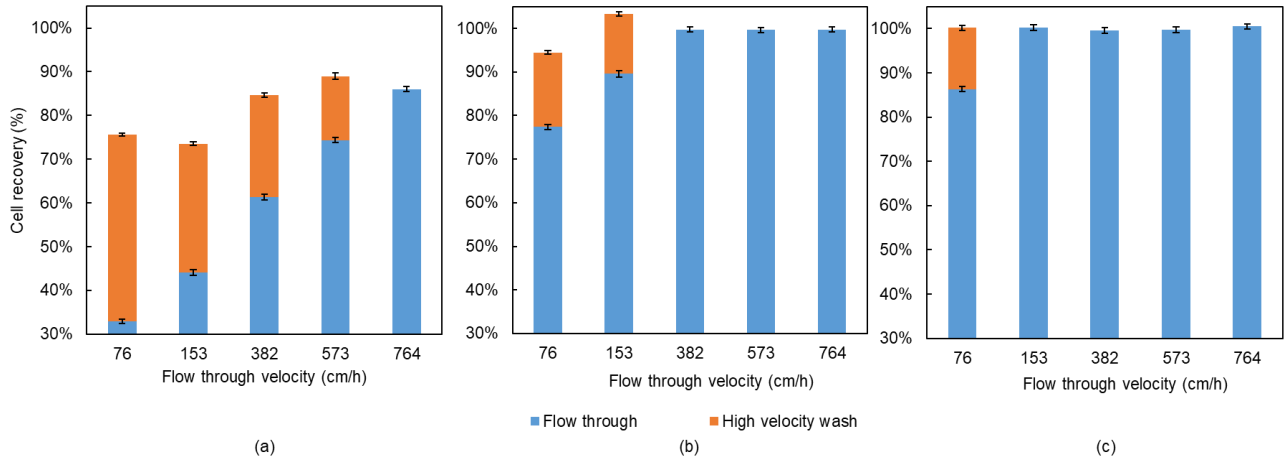


*Figure 6-9: Yeast cell recovery on (a) G300A-CM, (b) G400A-CM and (c) G500A-CM at varying linear velocity flow-through sample application. High velocity wash at 764 cm/h*

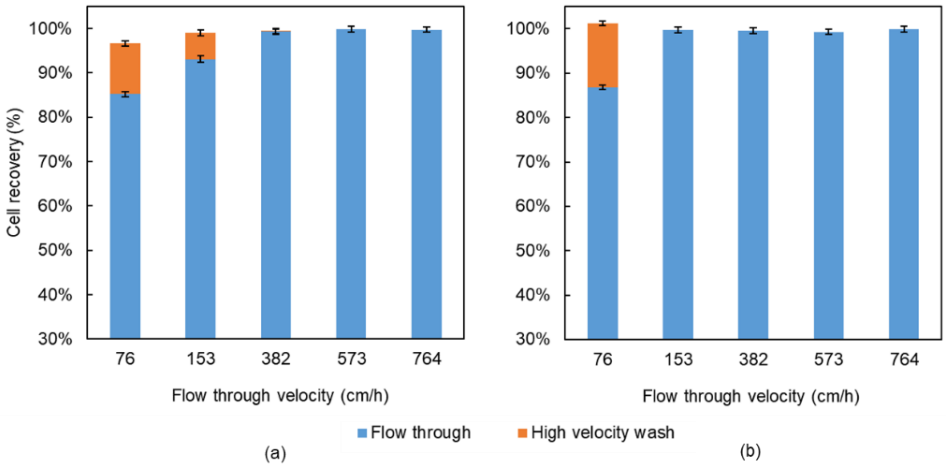


*Figure 6-10: Yeast cell recovery on (a) G400C-CM and (b) G500C-CM at varying linear velocity flow-through sample application. High velocity wash at 764 cm/h.*

Cell recovery in the flow-through fractions increased with increasing velocity for all columns and was lower for smaller channel sizes. Increasing the velocity reduced the cell capture effects of hydrodynamic interaction and sedimentation, meaning cells were did not become entrapped in the column. 100% cell recovery was achieved in the flow-through at four of the velocities tested on the 500 µm columns, and three of the velocities tested for the 400 µm agarose column.

The wash step was applied at a high velocity in order to remove cells already trapped in the columns, however the amount that could be recovered in this step was determined by the on-sample linear velocity. In other words, the high velocity wash did not mean that the same total cell recovery was measured on a column for different on-sample velocities. At lower on-sample velocities, advection was less prominent, meaning inertial impaction and sedimentation had a greater effect. Furthermore, at lower velocities, cell adsorption to CM ligands was more prominent because cells had more time to diffuse and adsorb to ligands immobilised to the channel walls. These effects were especially apparent on G300A-CM, where there was a higher surface area for sedimentation, hydrodynamic interaction, and adsorption, which was reflected in the total cell recovery never exceeding 86% despite the high velocity wash being applied.

On both agarose and cellulose columns with channel diameters 400 µm and 500 µm, addition of the high velocity was step was successful in increasing the cell recovery to 100%, with only the 76.4 cm/h trials not yielding 100% cell recovery on the 400 µm channel columns when the high velocity wash was applied. The high velocity wash increased the gravity number and modified Reynolds number to a point where increases in the Stokes number did not mean

inertial impaction had an effect. The combination of a low velocity on-sample application and high velocity wash is a promising operating parameter to consider for the use of TPMS hydrogels as solid-tolerant chromatographic media.

When considering the suitability of these columns to be used in solid-tolerant chromatography, protein adsorption and cell recovery were taken into account. From protein breakthrough studies, G400C-CM had the highest protein adsorption and dynamic binding capacity. When operated at 152.8 cm/h, the dynamic binding capacity was 5.0 mg/ml, and cell recovery was 100%. This column could be operated at a higher linear velocity, and the dynamic binding capacity would decrease to approximately 3.0 mg/ml, but 100% cell recovery would be maintained, and processing times reduced. As discussed in the previous chapter, the linear velocity selection would also be dependent on other operating costs.

Cell recovery in the flow-through for gyroids was compared with the experimental recovery values for G300A-CM, G400A-CM and G500A-CM, shown in Figure 6-11. Theoretical cell recovery was calculated using the analytical correlations from Tufenkji and Elimelech [63]. The theoretical recoveries calculated take into account capture mechanisms from diffusion, interception, sedimentation, and van der Waals attraction. Effects of hydrodynamic interaction and inertial impaction were not included. At high velocities, cell the experimental cell recovery was close to theoretical values, however this was not the case for low velocities, especially for the columns with smaller channels, as inertial impaction is more apparent at low velocities, and hydrodynamic interaction increases with larger surface area. This partially accounted for the deviation of the predicted cell recovery from the experimental.

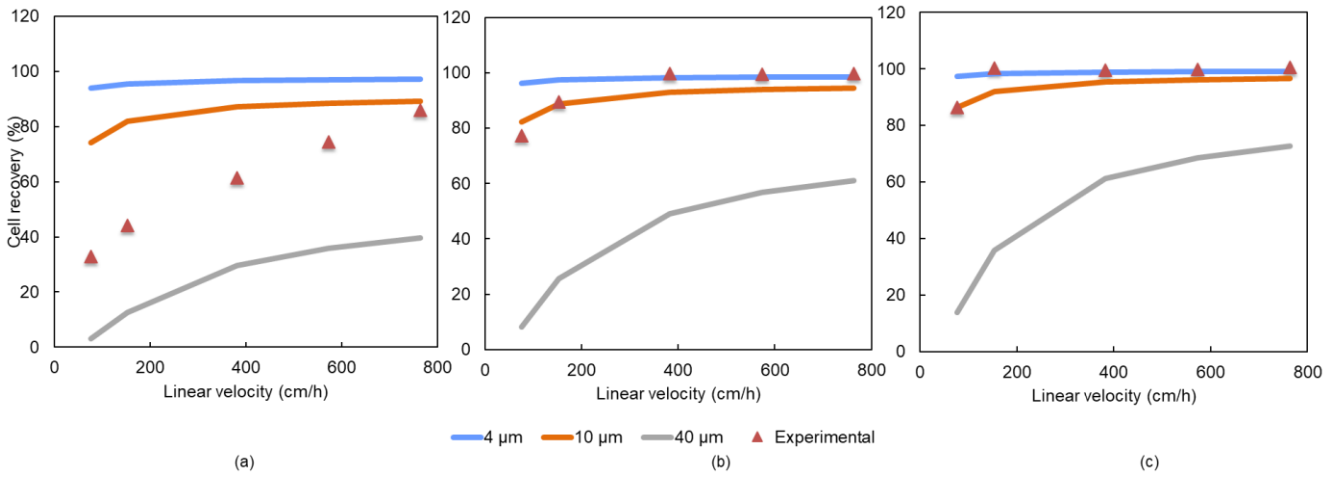


*Figure 6-11: Theoretical cell recovery for varying yeast cell diameters compared with experimental results on (a) G300A-CM, (b) G400A-CM and (c) G500A-CM*

At high velocities on G400A-CM and G500A-CM, the predicted cell recoveries for a 4 μm cell were the same as experimentally determined recovery values, although the cells likely had a size distribution between 4 – 40 μm. At higher velocities, it was thought that advection reliant terms such as hydrodynamic interaction and sedimentation were most dominant in determining overall cell recovery, hence they can easily be used to predict high cell recovery. However, at lower velocities on smaller diameter channel columns, the theoretical values erred significantly from predicted values because of non-uniformities and defects on the column walls and surfaces, as well as the fact that the model did not account for inertial impaction or hydrodynamic interaction. As seen in SEM images in Chapter 4, the hydrogel surfaces had an inherent roughness caused by the layer-by-layer creation of the TPMS template which propagated through to the hydrogel. While these defects would have been present on all the columns, the ratio of the size of these defects to the column diameter was larger on smaller columns. These defects and difference in aspect ratio were not considered in the theoretical cell recovery calculations. These defects would have increased the surface area, reducing the modified Reynolds number, provided a greater surface area for sedimentation, and a larger aspect ratio for interception.

The correlations from Tufenkji and Elimelech [63] are based on the filtration efficiency. The figure below shows the relative capture efficiencies for the three gyroid columns, for an assumed yeast cell diameter of 10 μm (Figure 6-12). At low linear velocities, the effect of sedimentation was the largest contributing mechanism to cell capture in the columns, leading to lower cell recovery in the flow-through. The mechanisms of sedimentation decreased with increasing cell velocity, while interception decreased slightly with increasing velocity because interception was dependent on channel diameter rather than velocity. Interception had the largest effect on G300A-CM, because the aspect ratio was the largest, meaning cells were more likely to come into contact with the TPMS column walls and become entrapped. There were small differences between the sedimentation effects with respect to channel diameter, where sedimentation effects were the largest on G300A-CM because while sedimentation efficiency was primarily dependent on the gravity number (which was independent of channel diameter), it was also affected by the aspect ratio, which decreased as channel diameter increased.

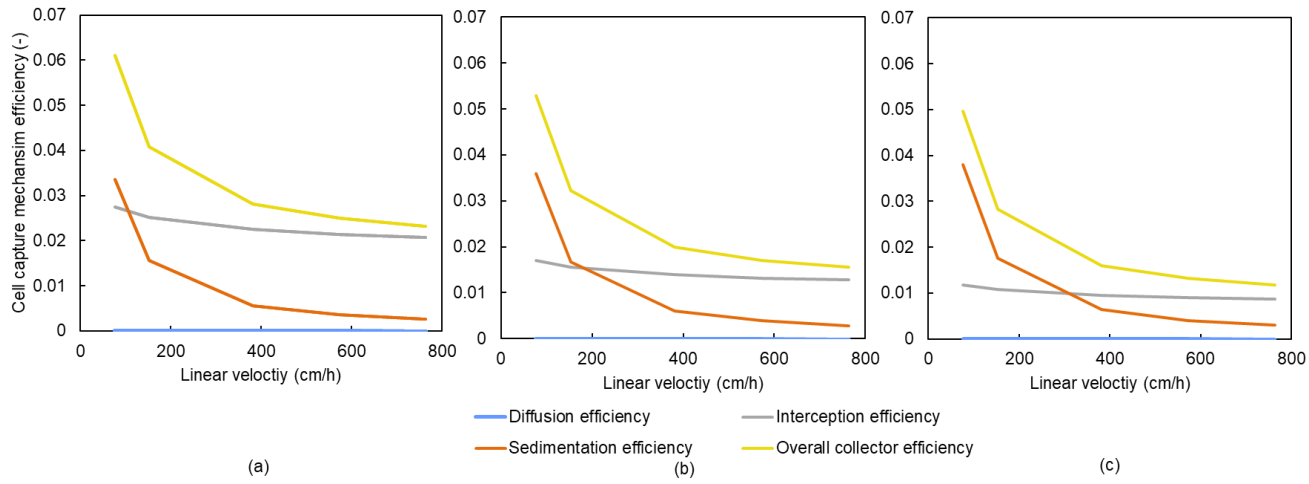


*Figure 6-12: Cell capture efficiency by mechanism on a) G300A-CM, b) G400A-CM, and c) G500A-CM*

The theoretical analysis of cell recovery in the TPMS gyroids assumed the broth was made of cells of a single diameter when in reality, this would not have been the case. Analysis of sedimentation and interception capture efficiencies demonstrated that the cell diameter had a large effect on determining the overall capture efficiency by sedimentation. The 40 µm cell had a significantly higher capture efficiency at the lowest cell velocity compared with the 4 µm and 10 µm cells, because the Stokes settling velocity of the cell increased exponentially with cell diameter. Sedimentation was particularly apparent at low velocities because there was a greater difference between the particle settling velocity. This shows the importance of understanding the size distribution of the cell culture, because changes in cell diameter greatly affect the ability of the column to process solids.

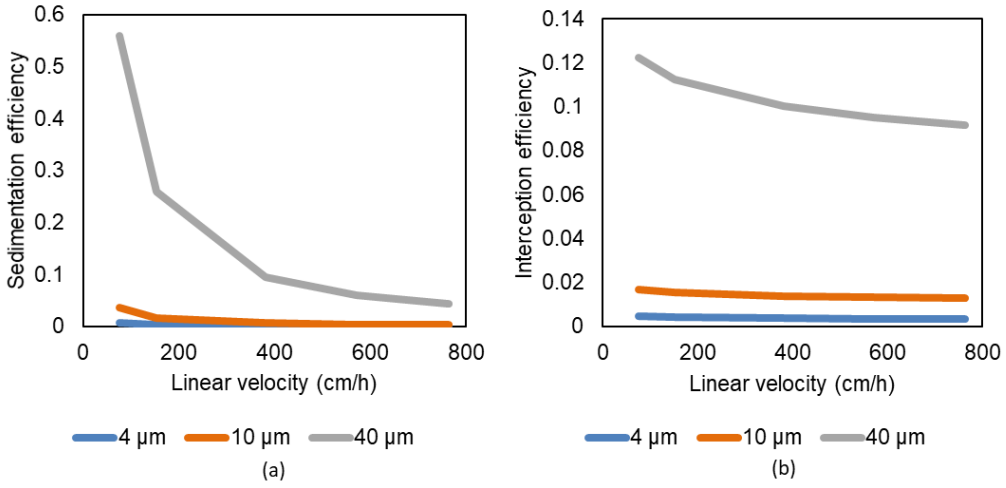


*Figure 6-13: Effect of cell diameter on a) sedimentation capture efficiency and b) interception capture efficiency on G400A-CM*

SEM images were taken of a segment of freeze-dried G400A-CM following the repeated experiments in this section, shown below (Figure 6-14). The last treatment on the column before freeze-drying was washing the column into deionised water following application of a high salt elution buffer. Examples of the TPMS channels were highlighted in yellow circles, clearly apparent in image (a), and examples of the layering effect were shown in the orange circles in (a) and (b). The layers were zoomed in on in (c) and (d), where cell deposits are shown in the purple circles. Lastly, the sections highlighted in green circles showed the formation of cell clusters present in the columns. These were likely due to the sample preparation method, where rehydrated bakers' yeast was mixed with a stirrer, however, stirring was not adequate to break up the yeast granules. These clusters were approximately 100 µm in diameter, meaning they were significantly more likely to be retained in the column, because capture mechanisms such as interception, straining, sedimentation, inertial impaction and hydrodynamic interaction all become more effective with larger diameter solid particles [119]. Therefore, on top of the layering effect, non-uniform cell size distribution and cell cluster formation were responsible for differences in the theoretical cell recovery, and the low cell recovery at low velocities and in columns with smaller channel diameters.

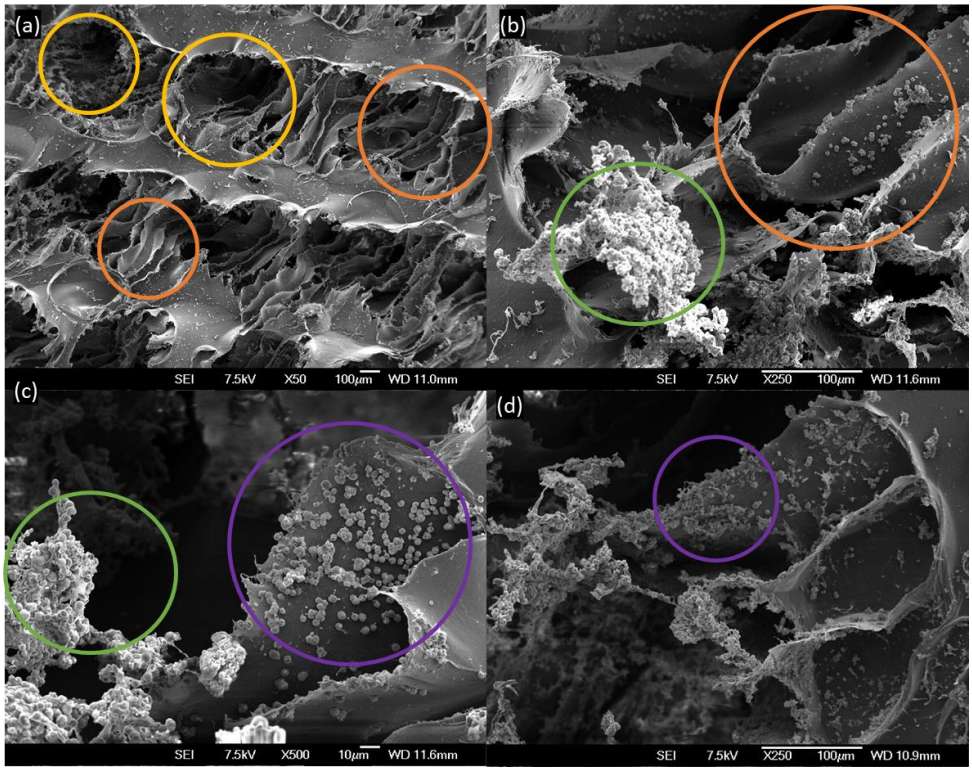


*Figure 6-14: SEM images demonstrating S. cerevisiae entrapment in G400C-CM after multiple sample applications. Highlighted sections are channels (yellow), layering effect (orange), cell entrapment on layers (purple), and cell clusters (green)*

## 6.4 Conclusions

In this chapter, yeast recovery through TPMS hydrogels was examined in the presence of protein to determine the effects of yeast on protein adsorption, and the overall yeast cell recovery in the columns was determined at different linear velocities on the different columns.

The presence of yeast cells in the protein solutions did not affect the protein adsorption efficiency, although yeast and associated extracellular material did adsorb to the columns because of the interactions between these compounds and the ligands. In particular, yeast cells adsorbed to the DEAE column because of opposing charges between cell wall and ligand, and proteins such as glycogen phosphorylase had affinity to the HIC column. These interactions highlighted the necessity of understanding the components of the on-sample when working with solid-tolerant chromatography columns, especially with the application being protein adsorption from cell cultures and fermentation broths which are complex mixtures.

At 76.4 cm/h, cell recovery was low on all columns, however with the increase in linear velocity of the on-sample in the flow-through, cell recovery increased because cell capture mechanisms such as sedimentation and interception decreased. On G300A-CM, the effects of interception were too high, and 100% cell recovery was never achieved, even with the application of a high velocity wash step to remove entrapped cells. The high velocity wash step resulted in 100% cell recovery overall for all on-sample velocities tested on G500A-CM and G500C-CM because of their large channels. It was also effective in increasing the cell recovery to 100% on G400A-CM when the on-sample was loaded on to the column at 152.8 cm/h. Overall, this step proved useful in achieving 100% cell recovery of the columns, which is required for solid-tolerant chromatography. Based on these results, and the results from the breakthrough experiments in the previous chapter, G400C-CM operated at or above 152.8 cm/h would yield the highest protein adsorption while maintaining 100% cell recovery.

Main controlling mechanisms for cell recovery were interception, which was most prevalent at high aspect ratios, and sedimentation, which was most prevalent at low linear velocities. The analysis in this chapter showed that cell recovery increased with increasing channel diameter and linear velocity to reduce the aspect ratio and decrease the difference between settling velocity and fluid velocity.

TPMS hydrogels were shown to have layers present on the column walls because of the 3D-printing template method used to prototype the columns. These layers were sources of

cell deposition and entrapment in the columns, reducing the cell recovery. SEM images also showed yeast cells depositing in clusters much greater than the predicted size range of yeast particles. This was a source of the actual experimental cell recovery being lower than those predicted at lower velocities. These cell clusters formed as a result of the preparation method, which was to rehydrate yeast granules under constant mixing; the mixing was not sufficient to break up the granules in some instances.

# Chapter 7. Conclusions and Recommendations for Future Work

## 7.1 Conclusions

This work presented the development of the first chromatography columns for solid-tolerant chromatography to be produced using 3D-printing methods. Columns were made of commonly used chromatographic stationary phase material (agarose and cellulose), functionalised for three common types of chromatography, demonstrated competitive static adsorption performance, and were able to capture protein from a cell/protein mixture, demonstrating solid-tolerant capabilities. The key achievements and conclusions of this work are presented below.

In Chapter 4, TPMS columns were made using a 3D-printing process from agarose and cellulose. The structure of these was confirmed to have good fidelity to the CAD design, with gyroids and Schwarz diamond columns being produced. TPMS channels and wall features were 300 μm, 400 μm, and 500 μm, as these were the limit on what could be produced in Solidworks, as file size was a limitation here. These columns were successfully functionalised for cation exchange, anion exchange, and hydrophobic interaction chromatography. These columns had lower ion exchange capacities compared with commercial resins, and the effects of TPMS feature size was apparent in determining the ion exchange capacity, whereby smaller channel columns had a higher ligand density because of the high surface area. Cellulose was shown to yield a higher ligand immobilisation density because of the higher percentage of polysaccharide in the hydrogel, and the smaller pore diameter resulting in a higher surface area available for ligand immobilisation. Static adsorption experiments using model proteins confirmed these columns' abilities to be used for protein adsorption, however some steric hindrance was noted as the protein binding capacity was lower than that of the small-ion capacity. SMA models did not account for this difference, which meant that the porous structure of the hydrogels also had an effect.

TPMS hydrogel columns performance under dynamic conditions were analysed in Chapter 5. Protein bind-and-elute experiments imitated process chromatography, and successful protein capture and subsequent elution was achieved, although protein adsorption was low at high flowrates. Reduced plate height calculations showed pore diffusion was the main dispersive

parameter, and reduced plate height values were larger than predicted, meaning chromatographic efficiency was low. Protein breakthrough experiments showed large mass transfer limitations on protein adsorption, as slow diffusion and fast advection resulted in protein being entrained out of the columns via advection at high linear velocities before it could be bound to the ligands. Cellulose columns were shown to have higher dynamic binding capacities because of their higher ligand densities. Based on the adsorption performance, G400C-CM was the best column for protein adsorption under dynamic conditions.

Protein adsorption in the presence of yeast cells was shown to be unaffected by the yeast cells, demonstrated in Chapter 6. Higher cell recovery was demonstrated at higher flowrates because of the reduced effects of cell sedimentation, and on columns with larger channel diameter because of the decreased aspect ratio reducing the effects of interception. G400C-CM operated at a minimum of 152.8 cm/h resulted in 100% cell recovery. Based on this result, and the protein adsorption results, with was concluded that operating G400C-CM at 152.8 cm/h would yield the best protein adsorption with simultaneous cell recovery. SEM images of the columns revealed the layering effect from the 3D-printed template which provided surfaces onto which cells became entrapped, and revealed cell clusters were present in the on-sample which accounted for deviations in experimental cell recoveries from predicted values at low linear velocities.

Overall, this work proved the concept of using 3D-printing techniques to produce a controlled geometry hydrogel column suitable for solid-tolerant chromatography. Despite the low adsorption capacity under dynamic conditions and poor chromatographic efficiency, the columns demonstrated the ability to function as solid-tolerant chromatography columns. Many of the problems with these columns arose from the limitations of the 3D-printing technology and associated software. The templating method yielded slight deviations to the macrostructure from the design and produced layers on the column walls which were a source for cell entrapment. The CAD and 3D-printing software limited the file sizes that could be designed and printed, meaning these were not optimised for chromatography. With advances in both of these technologies in recent years, the adsorption and chromatographic efficiency of these columns is likely to improve significantly.

## 7.2 Recommendations

For future developments regarding TPMS hydrogel columns for solid tolerant chromatography, there are several recommendations for the direction of future work, as given below.

With the development of better 3D printing processes, it is recommended that TPMS hydrogels be directly printed, rather than using a templating method. Furthermore, columns with larger overall diameters should be printed in order to improve chromatographic efficiency which would decrease the reduced plate height.

For better protein affinity to the columns, ligand selection should be reviewed. In this work, ligands were selected to demonstrate the ability of this type of column to be produced, now ligands may be selected with specific applications in mind.

Future TPMS columns made using these methods should be functionalised using a recirculating method, as this increases mass transfer of the reactants inside the TPMS channels, yielding a higher ligand immobilisation. However, it is also recommended that pre-functionalisation of agarose and cellulose powder be conducted, as this could result in higher ligand immobilisation, because the mass transfer limitations on reactant delivery would be greatly reduced.

Changes in porosity that occurred as a result of chemical functionalisation made prediction of surface area and binding capacities difficult. It is recommended that studies be conducted into the effects of the hydrogels' gelling temperature, functionalisation procedure and ligand density in order to quantify these effects.

With the conclusion of G400C-CM being recommended as the best column for solid-tolerant chromatography, further investigation into the operating parameters should be conducted. 152.8 cm/h was recommended as the best operating linear velocity, however based on the protein binding per minute, it may be more cost-efficient to run these columns at a higher velocity. Investigation into the optimisation of protein recovery, running time, pumping costs, and other associated costs should be conducted to determine the best linear velocity.

Lastly, it is recommended that specific applications for solid-tolerant TPMS columns be investigated, with the components of the biological feedstocks and their interactions with the columns fully understood. This work presented the effects of basic operating parameters, such as linear velocity and channel diameter on the efficiency of these columns, however

complete understanding of the interactions between feedstock and adsorbent would enable much more efficient design and application of these columns.

# Chapter 8. References


1. Gottschalk, U., *Process Scale Purification of Antibodies*. 2009, Hoboken, UNITED STATES: Wiley.
2. GE Healthcare. *CM Sepharose Fast Flow*. 2019 [cited 2019 30/01/2019]; Available from: https://www.gelifesciences.com/en/us/shop/cm-sepharose-fast-flow-p-02529.
3. Datar, R.V., T. Cartwright, and C.-G. Rosen, *Process Economics of Animal Cell and Bacterial Fermentations: A Case Study Analysis of Tissue Plasminogen Activator*. Nat Biotech, 1993. **11**(3): p. 349-357.
4. Thömmes, J., *Fluidized bed adsorption as a primary recovery step in protein purification*. Advances in biochemical engineering/biotechnology, 1997. **58**: p. 185-230.
5. Langer, E.S., *8th Annual Report and Survey of Biopharmaceutical Manufacturing Capacity and Production: A Survey of Biotherapeutic Developers and Contract Manufacturing Organisations*. 2011, BioPlan Associates: Rockville, Maryland.
6. Bartels, C.R., et al., *Novel ion-exchange method for isolation of streptomycin*. Chemical Engineering Progress, 1958. **54**(8): p. 49-51.
7. Belter, P.A., F.L. Cunningham, and J.W. Chen, *Development of a recovery process for novobiocin*. Biotechnology and Bioengineering, 1973. **15**(3): p. 533-549.
8. Erickson, J., J. Finch, and D. Greene, *Direct capture of recombinant proteins from animal cell culture media using a fluidized bed adsorber*. Animal Cell Technology: Products for today, 1994.
9. Fee, C.J., S. Nawada, and S. Dimartino, *3D printed porous media columns with fine control of column packing morphology*. Journal of Chromatography A, 2014. **1333**(0): p. 18-24.
10. Doble, M., *Principles of Downstream Techniques in Biological and Chemical Processes*. 2016, Oakville, CANADA: Apple Academic Press.
11. McGlaughlin, M.S. *An Emerging Answer to the Downstream Bottleneck*. BioProcess Insider, 2012.
12. Curbelo, D.R., et al., *Cost Comparison of Protein Capture from Cultivation Broths by Expanded and Packed Bed Adsorption*. Engineering in Life Sciences, 2003. **3**(10): p. 406-415.
13. Prieto, E.M. and S.A. Guelcher, *5 - Tailoring properties of polymeric biomedical foams*, in *Biomedical Foams for Tissue Engineering Applications*, P.A. Netti, Editor. 2014, Woodhead Publishing. p. 129-162.
14. Mohamed, M.H. and L.D. Wilson, *Porous Copolymer Resins: Tuning Pore Structure and Surface Area with Non Reactive Porogens*. Nanomaterials (Basel, Switzerland), 2012. **2**(2): p. 163-186.
15. Fanali, S., et al., *Liquid Chromatography : Fundamentals and Instrumentation*. 2013, Saint Louis, UNITED STATES: Elsevier.
16. GE Healthcare. *Resins*. 2019 [cited 2019 19/09/2019]; Available from: https://www.gelifesciences.com/en/us/shop/chromatography/resins.

17. Heinze, T., *New ionic polymers by cellulose functionalisation*. Macromolecular Chemistry and Physics, 1998. **199**(11): p. 2341 - 2364.

18. Hermanson, G.T., A.K. Mallia, and P.K. Smith, *Immobilized affinity ligand techniques*. 1992: Academic Press.

19. JNC Corporation. *Cellufine*. 2011 [cited 2019 19/09/2019]; Available from: https://www.jnc-corp.co.jp/fine/en/cellufine/.

20. Huber, T., et al., *Analysis of the Effect of Processing Conditions on Physical Properties of Thermally Set Cellulose Hydrogels*. Materials, 2019. **12**(7): p. 1066.

21. Huber, T., et al., *3D Printing Cellulose Hydrogels Using LASER Induced Thermal Gelation*. Journal of Manufacturing and Materials Proessing, 2018. **2**(3): p. 42.

22. Spalding, B.J., *Downstream Processing: Key To Slashing Production Costs 100 Fold*. Nat Biotech, 1991. **9**(3): p. 229-234.

23. Hileman, F.D., et al., *In Situ Preparation and Evaluation of Open Pore Polyurethane Chromatographic Columns*. Analytical Chemistry, 1973. **45**(7): p. 1126-1130.

24. Hansen, L.C. and R.E. Sievers, *Highly permeable open-pore polyurethane columns for liquid chromatography*. Journal of Chromatography A, 1974. **99**(C): p. 123-133.

25. Svec, F. and C.G. Huber, *Monolithic materials: promises, challenges, achievements*. 2006, ACS Publications.

26. Oberacher, H. and C. Huber, *Capillary monoliths for the analysis of nucleic acids by high-performance liquid chromatography–electrospray ionization mass spectrometry*. TrAC Trends in Analytical Chemistry, 2002. **21**(3): p. 166-174.

27. Svec, F. and J.M.J. Fréchet, *Molded rigid monolithic porous polymers: An inexpensive, efficient, and versatile alternative to beads for the design of materials for numerous applications*. Industrial and Engineering Chemistry Research, 1999. **38**(1): p. 34-48.

28. Tennikova, T.B., F. Svec, and B.G. Belenkii, *High-Performance Membrane Chromatography. A Novel Method of Protein Separation*. Journal of Liquid Chromatography, 1990. **13**(1): p. 63-70.

29. Belenkii, B.G., et al., *Peculiarities of zone migration and band broadening in gradient reversed-phase high-performance liquid chromatography of proteins with respect to membrane chromatography*. Journal of Chromatography A, 1993. **645**(1): p. 1-15.

30. Hara, T., et al., *Performance of Monolithic Silica Capillary Columns with Increased Phase Ratios and Small-Sized Domains*. Analytical Chemistry, 2006. **78**(22): p. 7632-7642.

31. Wells, C.M., K. Patel, and A. Lyddiatt, *Liquid fluidised bed adsorption in biochemical recovery and biological suspensions*. Separation for Biotechnology, 1987: p. 217-224.

32. Sirkar, K., *Separation of Molecules, Macromolecules and Particles: Principles, Phenomena and Processes*. 2014, Cambridge, UK: Cambridge University Press.

33. Hansson, M., et al., *Single-Step Recovery of a Secreted Recombinant Protein by Expanded Bed Adsorption*. Nat Biotech, 1994. **12**(3): p. 285-288.

34. Barnfield Frej, A., R. Hjorth, and Å. Hammarström, *Pilot scale recovery of recombinant annexin V from unclarified escherichia coli homogenate using expanded bed adsorption*. Biotechnology and Bioengineering, 1994. **44**(8): p. 922-929.

35. Spence, C., et al., *Fluidized-bed receptor-affinity chromatography*. Biomedical Chromatography, 1994. **8**(5): p. 236-241.

36. Chase, H.A. and N.M. Draeger, *Expanded-Bed Adsorption of Proteins Using Ion-Exchangers.* Separation Science and Technology, 1992. **27**(14): p. 2021-2039.

37. Morton, P. and A. Lyddiatt, *Direct Recovery of Protein Products from Whole Fermentation Broths: A role for ion exchange adsorption in fluidised beds*, in *Ion Exchange Advances: Proceedings of IEX '92*, M.J. Slater, Editor. 1992, Springer Netherlands: Dordrecht. p. 237-244.

38. Chang, Y., G. McCreath, and H.A. Chase, *Development of an expanded bed technique for an affinity purification of G6PDH from unclarified yeast cell homogenates.* Biotechnology and Bioengineering, 1995. **48**(4): p. 355-366.

39. Zurek, C., et al., *Production of two aprotinin variants in Hansenula polymorpha.* Process Biochemistry, 1996. **31**(7): p. 679-689.

40. Vouté, N., *Fluidized beds with beaded supports for protein separation*, in *Conference on separation of biopharmeuticals.* 1992: France.

41. Bascoul, A., B. Biscans, and H. Delmas, *Recuperation des proteins du lactoserum–perspectives industrielles*, in *Recents progres engenies des procedes.* 1991: France.

42. Richardson, J.F. and W.N. Zaki, *The sedimentation of a suspension of uniform spheres under conditions of viscous flow.* Chemical Engineering Science, 1954. **3**(2): p. 65-73.

43. Draeger, N.M. and H.A. Chase, *Liquid fluidized bed adsorption of protein in the presence of cells.* Bioseparation, 1991. **2**(2): p. 67-80.

44. Mustafa, M.A., et al., *Retrofit decisions within the biopharmaceutical industry: An EBA case study.* Food and Bioproducts Processing, 2006. **84**(1 C): p. 84-89.

45. Chase, H.A., *Purification of proteins by adsorption chromatography in expanded beds.* Trends in Biotechnology, 1994. **12**(8): p. 296-303.

46. Feuser, J., et al., *Cell/adsorbent interactions in expanded bed adsorption of proteins.* Bioseparation, 1999. **8**(1): p. 99-109.

47. Chase, H.A. and N.M. Draeger, *Affinity purification of proteins using expanded beds.* Journal of Chromatography A, 1992. **597**(1): p. 129-145.

48. Draeger, N.M. and H.A. Chase, *Protein adsorption in liquid fluidized beds.* Institution of Chemical Engineers Symposium Series, 1990(118): p. 161-172.

49. Tari, C., et al., *Colloid deposition experiments as a diagnostic tool for biomass attachment onto bioproduct adsorbent surfaces.* Journal of Chemical Technology and Biotechnology, 2008. **83**(2): p. 183-191.

50. Fee, C.J., S. Dimartino, and T. Huber, *Separation medium.* 2017, Google Patents.

51. Fee, C.J., *3D-printed porous bed structures.* Current Opinion in Chemical Engineering, 2017. **18**: p. 10-15.

52. Carta, G. and A. Jungbauer, *Protein Chromatography: Process Development and Scale-Up.* 2010, Weinheim: WILEY-VCH Verlag GmbH & Co. KGaA.

53. Levenspiel, O., *Chemical Reaction Engineering.* Third Edition ed. 1999, New York: Jon Wiley & Sons.

54. Halász, I. and K. Martin, *Pore sizes of solids.* Angewandte Chemie International Edition in English, 1978. **17**(12): p. 901-908.

55. Yao, Y. and A.M. Lenhoff, *Determination of pore size distributions of porous chromatographic adsorbents by inverse size-exclusion chromatography.* Journal of Chromatography A, 2004. **1037**(1): p. 273-282.

56. Staahlberg, J., B. Joensson, and C. Horvath, *Theory for electrostatic interaction chromatography of proteins.* Analytical Chemistry, 1991. **63**(17): p. 1867-1874.

57. Haller, W., *Critical Permeation Size of Dextran Molecules.* Macromolecules, 1977. **10**(1): p. 83-86.

58. van Deemter, J.J., F.J. Zuiderweg, and A. Klinkenberg, *Longitudinal diffusion and resistance to mass transfer as causes of nonideality in chromatography.* Chemical Engineering Science, 1956. **5**(6): p. 271-289.

59. Hayduk, W. and H. Laudie, *Prediction of diffusion coefficients for nonelectrolytes in dilute aqueous solutions.* AIChE Journal, 1974. **20**(3): p. 611-615.

60. Civan, F., *Porous Media Transport Phenomena.* 2011, Hoboken, UNITED STATES: John Wiley & Sons, Incorporated.

61. Rushton, A., A.S. Ward, and R.G. Holdich, *Solid-Liquid Filtration and Separation Technology : An Introduction.* 1996, Hoboken, GERMANY: John Wiley & Sons, Incorporated.

62. Cooper, G.M., *The cell: A molecular approach.* 1997, Sunderland, Mass; Washington, D. C.: ASM Press.

63. Tufenkji, N. and M. Elimelech, *Correlation Equation for Predicting Single-Collector Efficiency in Physicochemical Filtration in Saturated Porous Media.* Environmental Science and Technology, 2004. **38**(2): p. 529-536.

64. Axén, R. and S. Ernback, *Chemical fixation of enzymes to cyanogen halide activated polysaccharide carriers.* European Journal of Biochemistry, 1971. **18**(3): p. 351-360.

65. Axén, R., J. Porath, and S. Ernback, *Chemical coupling of peptides and proteins to polysaccharides by means of cyanogen halides.* Nature, 1967. **214**(5095): p. 1302-1304.

66. Axén, R. and P. Vretblad, *Binding of proteins to polysaccharides by means of cyanogen halides. Studies on cyanogen bromide treated Sephadex.* Acta chemica Scandinavica, 1971. **25**(7): p. 2711-2716.

67. Bethell, G.S., et al., *A novel method of activation of cross-linked agaroses with 1,1'-carbonyldiimidazole which gives a matrix for affinity chromatography devoid of additional charged groups.* Journal of Biological Chemistry, 1979. **254**(8): p. 2572-2574.

68. Hearn, M.T.W., *1,1'-Carbonyldiimidazole-Mediated Immobilization of Enzymes and Affinity Ligands.* Methods in Enzymology, 1987. **135**: p. 102-17.

69. Bethell, G.S., et al., *Investigation of the activation of various insoluble polysaccharides with 1,1'-carbonyldiimidazole and of the properties of the activated matrices.* Journal of Chromatography A, 1981. **219**(3): p. 361-371.

70. Shi, Q.-H., X. Zhou, and Y. Sun, *A novel superporous agarose medium for high-speed protein chromatography.* Biotechnology and Bioengineering, 2005. **92**(5): p. 643-651.

71. Toufik, J. and D. Labarre, *Relationship between reduction of complement activation by polysaccharide surfaces bearing diethylaminoethyl groups and their degree of substitution.* Biomaterials, 1995. **16**(14): p. 1081-1088.

72. Merck KGaA. *Glycidyltrimethylammonium chloride*. 2019 05/11/2019]; Available from: https://www.sigmaaldrich.com/catalog/product/aldrich/50053?lang=en&region=NZ.

73. Hull, C.W., *Apparatus for production of three-dimensional objects by stereolithography*. 1986.

74. Billiet, T., et al., *The 3D printing of gelatin methacrylamide cell-laden tissue-engineered constructs with high cell viability*. Biomaterials, 2014. **35**(1): p. 49-62.

75. Hockaday, L.A., et al., *Rapid 3D printing of anatomically accurate and mechanically heterogeneous aortic valve hydrogel scaffolds*. Biofabrication, 2012. **4**(3).

76. Melchels, F.P.W., J. Feijen, and D.W. Grijpma, *A review on stereolithography and its applications in biomedical engineering*. Biomaterials, 2010. **31**(24): p. 6121-6130.

77. Nakamura, M., et al. *Computer-assisted designing and biofabrication of 3-D hydrogel structures towards thick 3-D tissue engineering*. in *2011 MRS Fall Meeting, November 28, 2011 - December 2, 2012*. 2012. Boston, MA, United states: Materials Research Society.

78. Pataky, K., et al. *High-fidelity printing strategies for printing 3D vascular hydrogel structures*. in *NIP25: 25th International Conference on Digital Printing Technologies and Digital Fabrication 2009, September 20, 2009 - September 24, 2009*. 2009. Louisville, KY, United states: Society for Imaging Science and Technology.

79. Zhou, F., et al., *3D printing technology and the latest application in the aviation area*, in *Advanced Materials Research*. 2014. p. 1057-1060.

80. Zhao, C., et al., *Three dimensional (3D) printed electrodes for interdigitated supercapacitors*. Electrochemistry Communications, 2014. **41**: p. 20-23.

81. Ngo, T., et al., *Additive manufacturing (3D printing): A review of materials, methods, applications and challenges*. Composites Part B: Engineering, 2018. **143**: p. 172-196.

82. Bahnini, I., et al., *Additive manufacturing technology: the status, applications, and prospects*. The International Journal of Advanced Manufacturing Technology, 2018. **97**(1): p. 147-161.

83. Dolamore, F., C. Fee, and S. Dimartino, *Modelling ordered packed beds of spheres: The importance of bed orientation and the influence of tortuosity on dispersion*. Journal of Chromatography A, 2018. **1532**: p. 150-160.

84. Nawada, S., S. Dimartino, and C. Fee, *Dispersion behavior of 3D-printed columns with homogeneous microstructures comprising differing element shapes*. Chemical Engineering Science, 2017. **164**: p. 90-98.

85. Dolamore, F., *In Silico analysis of flow and dispersion in ordered porous media*. 2017.

86. Salmean, C. and S. Dimartino, *3D-Printed Stationary Phases with Ordered Morphology: State of the Art and Future Development in Liquid Chromatography*. Chromatographia, 2019. **82**(1): p. 443-463.

87. Kučera, F. and J. Jančář, *Homogeneous and heterogeneous sulfonation of polymers: A review*. Polymer Engineering & Science, 1998. **38**(5): p. 783-792.

88. Simon, U. and S. Dimartino, *Direct 3D printing of monolithic ion exchange adsorbers*. Journal of Chromatography A, 2019. **1587**: p. 119-128.

89. Dhariwala, B., E. Hunt, and T. Boland, *Rapid prototyping of tissue-engineering constructs, using photopolymerizable hydrogels and stereolithography*. Tissue Engineering, 2004. **10**(9-10): p. 1316-1322.

90. Killion, J.A., et al., *Hydrogel/bioactive glass composites for bone regeneration applications: synthesis and characterisation.* Mater Sci Eng C Mater Biol Appl, 2013. **33**(7): p. 4203-12.

91. Nishiyama, Y., et al., *Development of a three-dimensional bioprinter: Construction of cell supporting structures using hydrogel and state-of-the-art inkjet technology.* Journal of Biomechanical Engineering, 2009. **131**(3).

92. Seck, T.M., et al., *Designed biodegradable hydrogel structures prepared by stereolithography using poly(ethylene glycol)/poly(d,l-lactide)-based resins.* Journal of Controlled Release, 2010. **148**(1): p. 34-41.

93. CELLINK AB, *BIO X 3D Bioprinter*, in *www.cellink.com/bioprinter*, CELLINK, Editor. 2019, CELLINK AB: Boston, USA.

94. Lord, E.A. and A.L. Mackay, *Periodic minimal surfaces of cubic symmetry.* Current Science, 2003. **85**(3): p. 346-362.

95. Jung, Y., K.T. Chu, and S. Torquato, *A variational level set approach for surface area minimization of triply-periodic surfaces.* Journal of Computational Physics, 2007. **223**(2): p. 711-730.

96. Sreedhar, N., et al., *Mass transfer analysis of ultrafiltration using spacers based on triply periodic minimal surfaces: Effects of spacer design, directionality and voidage.* Journal of Membrane Science, 2018. **561**: p. 89-98.

97. Al-Ketan, O., R. Rowshan, and R.K. Abu Al-Rub, *Topology-mechanical property relationship of 3D printed strut, skeletal, and sheet based periodic metallic cellular materials.* Additive Manufacturing, 2018. **19**: p. 167-183.

98. Solidscape Inc. *Midas Castable Material.* 2020 [cited 2020 18/04/2020]; Available from: https://www.solidscape.com/products/3d-printing-materials/wax/midas-castable-material/.

99. Solidscape Inc. *Melt Dissolvable Support.* 2020 [cited 2020 18/04/2020]; Available from: https://www.solidscape.com/products/3d-printing-materials/wax/melt-dissolvable-support/.

100. Stone, M.C. and G. Carta, *Protein adsorption and transport in agarose and dextran-grafted agarose media for ion exchange chromatography.* Journal of Chromatography A, 2007. **1146**(2): p. 202-215.

101. GE Healthcare. *SP Sepharose Big Beads.* 2019 30/01/2019]; Available from: https://www.gelifesciences.com/en/us/shop/chromatography/resins/ion-exchange/sp-sepharose-big-beads-p-00972.

102. Yun, J., et al., *An improved capillary model for describing the microstructure characteristics, fluid hydrodynamics and breakthrough performance of proteins in cryogel beds.* Journal of Chromatography A, 2011. **1218**(32): p. 5487-5497.

103. DePhillips, P. and A.M. Lenhoff, *Pore size distributions of cation-exchange adsorbents determined by inverse size-exclusion chromatography.* Journal of Chromatography A, 2000. **883**(1): p. 39-54.

104. Hua, J., et al., *Highly Porous Cellulose Microbeads and their Adsorption for Methylene Blue.* Fibers and Polymers, 2019. **20**(4): p. 794-803.

105. JNC Corporation, *Cellufine MAX S, Q, CM, DEAE*, J. Corporation, Editor. 2012: Tokyo.

106. Merck. *DEAE–Sepharose® Fast Flow*. 2018 [cited 20/11/2018]; Available from: https://www.sigmaaldrich.com/catalog/product/sigma/dff100?lang=en&region=NZ&gclid=EAIaIQobChMImsO796y-3gIVQQ4rCh0yFQedEAAYASAAEgLn4vD_BwE.

107. Merck. *DEAE–Sepharose® CL-6B*. 2018 [cited 20/11/2018]; Available from: https://www.sigmaaldrich.com/catalog/product/sigma/dcl6b100?lang=en&region=NZ.

108. Johnson, T.F., et al., *Three dimensional characterisation of chromatography bead internal structure using X-ray computed tomography and focused ion beam microscopy*. Journal of Chromatography A, 2018. **1566**: p. 79-88.

109. Levison, P.R., et al., *Performance comparison of low-pressure ion-exchange chromatography media for protein separation*. Journal of Chromatography A, 1997. **760**(1): p. 151-158.

110. General Electric Company, *Phenyl Sepharose High Performance Butyl Sepharose High Performance*, G.E. Company, Editor. 2012, GE Healthcare UK Limited: Little Chalfont, UK.

111. Geno Technology Inc, *G-Trap HIC Columns*, G. Biosciences, Editor. 2019, G Biosiences: USA.

112. Yun, J., et al., *Modeling of protein breakthrough performance in cryogel columns by taking into account the overall axial dispersion*. Journal of Separation Science, 2009. **32**(15-16): p. 2601-2607.

113. Colin, H., *Simple Considerations on Column Design in Preparative-Scale Liquid Chromatography*. Separation Science and Technology, 1987. **22**(8-10): p. 1851-1868.

114. Hearn, M.T.W., et al., *Application of 1,1'-Carbonyldiimidazole-activated agarose for the purification of proteins: II. The use of an activated matrix devoid of additional charged groups for the purification of thyroid proteins*. Journal of Chromatography, 1979. **185**: p. 463-470.

115. US Department of Agriculture. *Yeast*. 2019 [cited 2019 13/11/2019]; Available from: https://fdc.nal.usda.gov/fdc-app.html#/food-details/343391/nutrients.

116. Leggett, J.E., W.R. Heald, and S.B. Hendricks, *Cation binding by baker's yeast and resins*. Plant physiology, 1965. **40**(4): p. 665-671.

117. Tervoort, M.J., L.T.M. Schilder, and B.F. Van Gelder, *The absorbance coefficient of beef heart cytochrome c1*. BBA - Bioenergetics, 1981. **637**(2): p. 245-251.

118. Baldwin, W.W. and H.E. Kubitschek, *Buoyant density variation during the cell cycle of Saccharomyces cerevisiae*. Journal of Bacteriology, 1984. **158**(2): p. 701-704.

119. Payatakes, A.C., *Trajectory calculation of particle deposition in deep bed filtration - 1. Model Formulation*. AIChE journal, 1974. **20**(5): p. 889-900.

# Appendix 1. Supplementary Isotherm Analysis

Steric mass action (SMA) law (Equation 2-6) and Freundlich isotherms (Equation 2-7) were fitted to protein adsorption data from Chapter 4 (Figures A1 – A4). SMA parameters ($q_0$, $z$, $\sigma$) were determined using the method outlined in section 4.4.2, with $K_m$ fit using the least squares method. Freundlich constants were determined using a linearization method. Neither equations showed a good fit to the experimental data, hence were not included in this thesis.

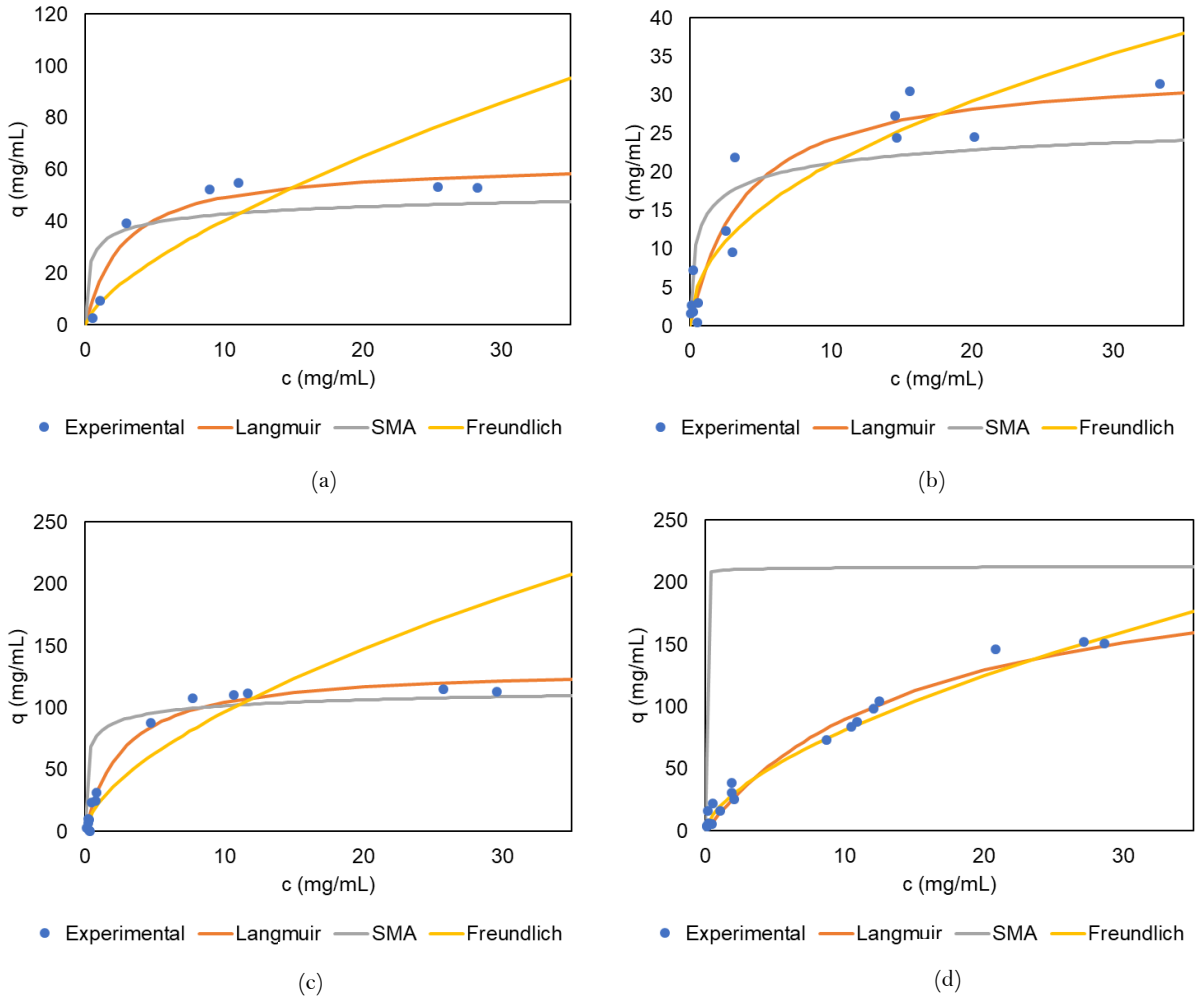


*Figure A1: All adsorption data and isotherm curves for: (a) G400A-CM, (b) G500A-CM, (c) G400C-CM, (d) G400A-DEAE*

# Appendix 2. Example Calculations

## Reduced Plate Height

Example calculation for Gaussian parameters and HETP for G300A-CM at 1.0 mL/min

$L$ = 3.9 cm, $d_p$ = 300 x $10^{-6}$ m

Using the elution peak, trapezium rule was used to determine the following integrals:

$$\mu_0 = \int_0^\infty C dt = \sum C_i \Delta t \qquad (2-11)$$

$$\mu_0 = 5383.96$$

$$\mu_1 = \frac{1}{\mu_0}\int_0^\infty C t dt = \frac{1}{\mu_0}\sum C_i t_i \Delta t \qquad (2-12)$$

$$\mu_1 = 6.45 \text{ min} = mean\ elution\ time$$

$$\sigma^2 = \frac{1}{\mu_0}\int_0^\infty C(t-\mu_1)^2 dt = \frac{\sum t_i^2 C_i}{\sum C_i} - \mu_1^2 \qquad (2-13)$$

$$\sigma^2 = 11.49 \text{ min}^2$$

$$HETP = \frac{\sigma^2 L}{\mu_1^2} \qquad (2-22)$$

$$HETP = \frac{11.49^2 \times 3.9}{6.45} = 1.08\ cm$$

$$h' = \frac{HETP}{d_p} \qquad (2-24)$$

$$h' = \frac{\frac{1.08}{100}}{\frac{300}{10^6}} = 35.9$$

## Dimensionless Numbers

Dispersion number, $N_D$

Using parameters from above in G300A-CM, 1.0 mL/min

$$\sigma_\theta = \frac{\sigma^2}{\mu_1^2} \qquad (2-14)$$

$$\sigma_\theta = \frac{11.49^2}{6.45^2} = 0.27$$

$$\sigma_\theta = \frac{2\mathbf{D_{ax}}}{uL} - 2\left(\frac{\mathbf{D_{ax}}}{uL}\right)^2\left(1 - e^{-\frac{uL}{\mathbf{D_{ax}}}}\right) \qquad (2-15)$$

Using Solver, values for $N_D = \frac{\mathbf{D_{ax}}}{uL}$ iterated through equation 2-15 until $\sigma_\theta = 0.27$.

$$N_D = \frac{\mathbf{D_{ax}}}{uL} = 0.165$$

Peclet number, Pe

$$u = \frac{F_0}{A} \qquad (2-25)$$

$$u = \frac{\left(\frac{\frac{1.0}{1000}}{60}\right)}{\frac{\pi}{4} \times 0.01^2} = 2.1 \times 10^{-4}\ m\ s^{-1}$$

$$v = \frac{u}{\varepsilon} \qquad (2-26)$$

$$v = \frac{2.1 \times 10^{-4}}{0.82} = 2.6 \times 10^{-4}\ m\ s^{-1}$$

Where $\varepsilon$ was determined using ISEC.

Cytochrome c diffusivity calculated using H-L correlation

$$\mathbf{D_{m,AB}} = \frac{13.16 \times 10^{-5}}{\mu_B^{1.14} V_A^{0.589}} \qquad (2-27)$$

$$\mathbf{D_{m,AB}} = \frac{13.16 \times 10^{-5}}{0.001^{1.14} 144.1^{0.589}} = 2.05 \times 10^{-13}\ m^2\ s^{-1}$$

$$\mathrm{Pe} = \frac{\mathrm{vL}}{\mathbf{D_m}} \qquad (2-9)$$

$$Pe = \frac{2.6 \times 10^{-4} \times 0.0039}{2.05 \times 10^{-13}} = 3.9 \times 10^{7}$$

Reynolds number, Re, assuming liquid properties close to water

$$Re = \frac{Dv\rho}{\mu} \qquad (2-35)$$

$$Re = \frac{300 \times 10^{-6} \times 2.6 \times 10^{-4} \times 998}{0.001} = 0.064$$

## Solid Removal Mechanisms

For G300A-CM

| **Parameters** | | |
|---|---|---|
| Cell diameter, $d_s$ | 40 | µm |
| | 0.00004 | m |
| Cell density, $\rho_s$ | 1112.6 | kg/m$^3$ |
| Fluid density, $\rho_f$ | 998 | kg/m$^3$ |
| Fluid viscosity $\mu_f$ | 0.001 | Pa.s |
| $\varepsilon$ | 0.81 | |
| F | 1 | mL/min |
| u | 0.00021 | m/s |
| $u_0$ | 0.000424 | m/s |
| $d_p$ | 300 | µm |
| | 0.0003 | m |
| $S_v$ | 5150 | m$^{-1}$ |

$$\mathrm{N_G} = \frac{\mathrm{d_s^2}(\rho_s - \rho_f)\mathrm{g}}{18\mu_f \mathrm{u}} \qquad (2-31)$$

$$N_G = \frac{0.0004^2 \times (1112.6 - 998) \times 9.81}{18 \times 0.001 \times 0.000424} = 0.236$$

$$N_R = \frac{d_s}{d_p} \qquad (2-32)$$

$$N_R = \frac{0.00004}{0.0003} = 0.1333$$

$$\mathrm{St} = \frac{\rho_s d_s^2 u}{18 \mu_f d_p} \qquad (2-34)$$

$$St = \frac{1112.6 \times 0.00004^2 \times 0.000424}{18 \times 0.001 \times 0.0003} = 0.000126$$

$$Re_l = \frac{v \rho_f}{(1-\varepsilon) S_v \mu_f} \qquad (2-36)$$

$$Re_l = \frac{0.00021 \times 998}{(1-0.81) \times 5150 \times 0.001} = 0.082$$